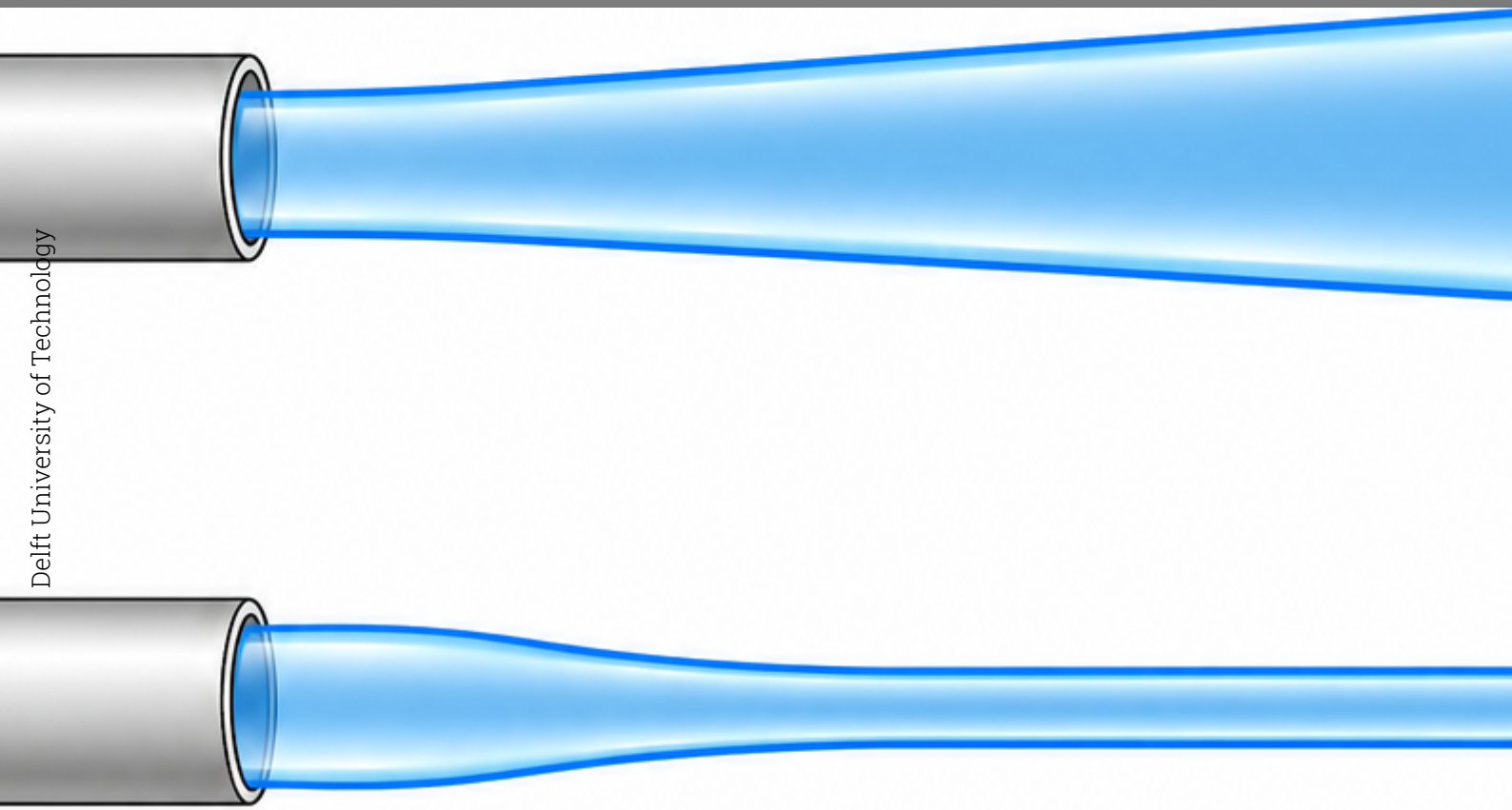
Undeveloped laminar liquid jets

Effect of the nozzle length on the expansion or contraction behaviour

Master of Science Thesis

Loek Thon



Delft University of Technology

TU Delft

Undeveloped laminar liquid jets

Effect of the nozzle length on the expansion or contraction behaviour

by

Loek Thon

Supervisors:	W.P. Breugem, M.J.B.M. Pourquie & G. Ooms
Project Duration:	February, 2026 - December, 2026
Course:	ME55035
Faculty:	Faculty of Mechanical Engineering, Delft University of Technology Department of Process & Energy

Cover image: AI-generated, see Appendix E

TU Delft

Abstract

The expansion or contraction of a laminar Newtonian liquid jet emerging from a circular nozzle is governed by the interaction of viscous, inertial and capillary forces. For a fully developed nozzle flow, the jet expands at low Reynolds numbers due to viscous effects, whereas increasing inertial effects result in jet contraction at higher Reynolds numbers. However, for shorter nozzles, the flow may not be fully developed before exiting the nozzle. This thesis investigates the influence of nozzle length on jet expansion and contraction, with particular emphasis on distinguishing the contributions of hydrodynamic flow development and viscous nozzle-exit perturbations.

An integral momentum balance for fully developed nozzle flow was extended to incorporate hydrodynamically undeveloped velocity profiles. The resulting decomposition distinguishes between the contribution of flow development to the axial momentum flux, excess pressure and wall-shear contributions, and capillary effects. Numerical simulations were performed using the finite-volume solver OpenFOAM version 13, employing a geometric Volume-of-Fluid method to capture the liquid–gas interface. A total of 56 combinations of Reynolds number and nozzle length were investigated, covering a nozzle bulk Reynolds number in the range of $4.2 \leq Re \leq 400$ and $L/R = 1.94,\ 2.00,\ 5.16,\ 21.4$. For each configuration, a jet simulation was compared with an undisturbed pipe-flow simulation to quantify the nozzle-exit perturbations and to isolate the undeveloped flow at the nozzle outlet position.

The results demonstrate that nozzle length has little influence on jet expansion or contraction at low Reynolds numbers, where viscous exit-induced perturbations dominate and the nozzle flow is approximately fully developed. At higher Reynolds numbers, the increasing hydrodynamic development length causes shorter nozzles to produce increasingly underdeveloped exit velocity profiles. Consequently, jets emerging from shorter nozzles experience weaker contraction than jets emerging from longer nozzles. At $Re = 400$, the difference in contraction ratio between the shortest and longest nozzles reaches approximately 6%. Reconstruction of the contraction ratio using the extended integral momentum balance generally agrees with the numerical results, although quantitative differences remain between the simulations and experimental measurements.

To investigate this, an additional Weber number sensitivity analysis was performed using both the integral momentum balance reconstruction and OpenFOAM simulations. The analysis demonstrates that surface tension influences the reconstructed contraction ratio both directly through the capillary contribution and through the capillary pressure contribution included in the excess pressure and shear terms. Additional simulations at increased Weber numbers confirm that reducing the relative influence of surface tension produces greater jet contraction, reducing the differences with experimental observations. However, the reductions are smaller than predicted by the reconstruction when the velocity and pressure fields and interface geometry are held fixed. Furthermore, the high-Reynolds-number simulations may not have reached their final constant jet radii at the evaluated downstream locations.

Overall, the results demonstrate that the influence of nozzle length on jet expansion and contraction is closely related to the hydrodynamic development of the flow inside the nozzle. At low Reynolds numbers, viscous exit-induced perturbations dominate the jet behaviour, increasing expansion and resulting in an increased jet radius. At higher Reynolds numbers, hydrodynamic flow development becomes increasingly important, with more developed velocity profiles producing stronger jet contraction. Conversely, underdeveloped nozzle flows exhibit weaker contraction. Additionally, capillary effects contribute to the quantitative differences between numerical results reported in this work and experimental contraction ratios, particularly in the high-Reynolds-number regime.

Contents

Abstract i

Nomenclature iv

1 Introduction 1

2 Literature 4
2.1 Fully developed long nozzle flow . . . 4
2.1.1 Experimental research . . . 4
2.1.2 Theoretical contraction ratio limit . . . 5
2.1.3 Numerical research . . . 5
2.2 Short nozzle flow . . . 7
2.2.1 Experimental research on the effect of tube length . . . 7
2.2.2 Flow development . . . 8

3 Computational method and setup 10
3.1 The Volume Of Fluid method . . . 10
3.2 Surface reconstruction . . . 11
3.3 Surface tension model . . . 11
3.4 Computational grid . . . 11
3.5 Initialization and boundary conditions . . . 13
3.6 Numerical stability and time step . . . 13

4 Integral momentum balance 15
4.1 Derivation . . . 16
4.2 Analytical approximation . . . 18
4.2.1 Entry flow equations . . . 18
4.2.2 Analytical jet ratio . . . 19
4.3 Flow regimes . . . 20
4.3.1 Degree of development . . . 20
4.3.2 Viscous effects . . . 21
4.3.3 Distinction between viscous outflow effects and flow development . . . 22
4.3.4 Capillary effects . . . 23

5 Two-dimensional flow fields 24
5.1 Flow field decompositions . . . 24
5.1.1 Viscous regime: $Re = 4.2$ . . . 24
5.1.2 Inertial regime: $Re = 400$ . . . 25
5.1.3 Perturbation fields . . . 26
5.2 Effect of the nozzle length on the perturbation flow fields . . . 28

6 Centerline velocity 31

7 Jet profile 34
7.1 Numerical surface results . . . 34
7.2 Final jet ratio . . . 36
7.2.1 Direct numerical results . . . 36
7.2.2 Reconstruction . . . 37
7.2.3 Sensitivity to the Weber number . . . 38
7.3 Jet angle and curvature at the nozzle outlet . . . 41

8 Conclusion 42

9 Recommendations for future work 44

References **45**

A Mesh sensitivity study **47**

B Additional numerical surface results **48**

C Numerical solver settings **51**
C.1 `controlDict` 51
C.2 `fvSolution` 52
C.3 `fvSchemes` 53
C.4 `blockMeshDict` 54

D Numerical mesh settings **58**

E AI Statements **59**

Nomenclature

Symbols

Symbol	Definition	Unit
D	Diameter	m
g	Gravitational acceleration	$m\,s^{-2}$
L	Nozzle length	m
L_{dev}	Hydrodynamic development length	m
L_f	Axial distance downstream of the nozzle exit to the final jet radius	m
L/R	Nozzle length-radius ratio	$-$
$\dot{M}$	Momentum flux	N
$\tilde{K}$	Dimensionless excess viscous contribution	$-$
r	Radial coordinate	m
R	Nozzle radius	m
$R_i(x)$	Local jet radius	m
R_f	Final jet radius	m
p	Pressure	Pa
$\tilde{P}_{exc}$	Excess pressure contribution	$-$
$\tilde{T}_{exc}$	Excess integral wall shear stress contribution	$-$
u	axial velocity	$m\,s^{-1}$
U_b	uniform axial inflow velocity	$m\,s^{-1}$
U_f	Final mean axial jet velocity	$m\,s^{-1}$
U_x	Axial velocity	$m\,s^{-1}$
U_r	Radial velocity	$m\,s^{-1}$
x	Axial coordinate	m
x/R	Normalized axial coordinate	$-$
α	VOF Coefficient, liquid volume fraction on cell basis	$-$
β_{outlet}	Outlet development parameter	$-$
$\chi = R_i(L_f)/R$	Jet (radius or diameter) ratio	$-$
σ	Surface tension	$N\,m^{-1}$
κ	Local interface curvature	m^{-1}
μ	Dynamic viscosity	$kg\,m^{-1}\,s^{-1}$
ν	Kinematic viscosity	$m^2\,s^{-1}$
φ	Jet angle at nozzle exit	$-$
ρ	Density	$kg\,m^{-3}$
τ_{xr}	Wall shear stress	Pa

Dimensionless numbers

Reynolds number	$Re = \frac{2U_bR}{\nu}$	$\frac{\text{Inertia}}{\text{Viscous forces}}$
Weber number	$We = \frac{\rho U_b^2 R}{\sigma}$	$\frac{\text{Inertia}}{\text{Capillary forces}}$
Froude number	$Fr = \frac{U_b}{\sqrt{gR}}$	$\frac{\text{Inertia}}{\text{Gravitational forces}}$
Capillary number	$Ca = 2We/Re = \frac{\mu U_b}{\sigma}$	$\frac{\text{Viscous forces}}{\text{Capillary forces}}$

1. Introduction

Forcing a visco-elastic or non-Newtonian liquid through a long nozzle into a gaseous environment can lead to expansion of the liquid. This expansion effect is known as the die-swell phenomenon or Barus effect, named after its discoverer in the 19th century [1]. In the 1960s of the previous century, Middleman and Gavis [21] experimented with this phenomenon and found that a jet of viscoelastic expands for low ejection velocities, whereas it contracts for higher velocities. They attributed the changing diameter behaviour to an elastic 'stress memory effect'.

The swelling of jets is not limited to viscoelastic liquids, however. Newtonian liquid jets may also undergo an expansion after exiting a nozzle, when the Reynolds number is sufficiently low. This was first observed by Middleman and Gavis [20]. Of course, for a Newtonian liquid, the expansion cannot be attributed to an elastic relaxation effect; rather, it is a viscous relaxation effect. Richardson [27] investigated the theory behind the swelling behaviour for Newtonian fluids. He attributed this to a transition from a no-slip velocity condition at the nozzle wall, to a free-slip condition at the liquid-gas interface, when the liquid is ejected. More recently, the effect of the Reynolds number on a fully developed jet flow was investigated numerically by Breugem and Kamis [3], who concluded that expansion occurs as a consequence of a radially outward flow and the accompanying normal viscous stress acting on the jet interface directly downstream of the nozzle exit. A Newtonian liquid jet will eventually contract when the Reynolds number is increased sufficiently, as a consequence of inertial effects taking over [3].



Figure 1.1: Conceptual relationship between jet geometry, interfacial instabilities and droplet formation.

The expansion or contraction behaviour of liquid jets is important in the process of prilling, for example for fertilizer grain production. In the prilling process, droplets are generated under inertio-capillary breakup of (spiralling) jets. The droplet forming process relates to Rayleigh-Plateau instabilities forming in the jet, which are influenced by the change in diameter of the liquid jet. [16]. Since the characteristics of Rayleigh-Plateau instabilities depend on the local jet radius, understanding the expansion or contraction of the liquid jet is relevant to predict the breakup behaviour and consequently the droplet characteristics. Its conceptual relationship is visualised in Figure 1.1.

In this thesis, the expansion and contraction behaviour of Newtonian liquid jets, ejected from a cylindrical nozzle, is investigated, with an emphasis on the effect of underdeveloped nozzle flow and nozzle exit effects.

For laminar flow, the velocity profile approaches the fully developed Poiseuille profile over a characteristic hydrodynamic development length: L_{dev}, given by Equation 1.1 [6] below, where R is the nozzle radius and Re is the Reynolds number:

$$\frac{L_{dev}}{R} = 2\left[(0.619)^{1.6} + (0.0567\,Re)^{1.6}\right]^{\frac{1}{1.6}} \tag{1.1}$$

The jet expansion and contraction behaviour for a fully developed outflow has been studied experimentally by Goren and Wronski [10], showing expanding behaviour for low Reynolds number viscous-dominated flows and contracting behaviour, as the inertial effects start to come into play at higher Reynolds numbers.

The influence of the nozzle length has been experimentally investigated by Gavis and Modan [8] for Reynolds numbers up to 1000. At high Reynolds numbers, their experimental results show a relation between nozzle length and jet contraction ratio. The authors attribute this to incomplete flow development.

The influence of nozzle length on the downstream jet behaviour can be related to the hydrodynamic development of the flow inside the nozzle. For a sufficiently long nozzle, the velocity profile approaches a fully developed Poiseuille profile, whereas for shorter nozzles, the flow may be underdeveloped at the nozzle exit. The resulting differences in the exit velocity profile affect the axial momentum flux and, consequently, the expansion or contraction of the jet. As the Reynolds number increases, the hydrodynamic development length increases, potentially causing the flow in a nozzle of fixed length to become increasingly underdeveloped.

In addition to hydrodynamic development, the flow is affected by the transition from a no-slip boundary condition at the nozzle wall to a free-slip condition at the liquid–gas interface. This transition induces flow perturbations upstream of the nozzle exit, affecting the velocity and stress distributions just upstream of the nozzle outlet. Consequently, the downstream jet behaviour is influenced by both the degree of hydrodynamic development and the perturbations induced by the nozzle exit. Distinguishing and quantifying these contributions is the central objective of this research:

How does the nozzle length influence the expansion or contraction behaviour of a laminar liquid jet, through hydrodynamic flow development and nozzle outflow perturbations?

To quantify this, the integral momentum balance as derived by Breugem and Kamis [3] for a long nozzle with a fully developed Poiseuille flow, far upstream of the nozzle exit, will be extended to include the effects of potentially undeveloped nozzle flow. In order to relate upstream exit effects and the downstream jet behaviour, the integral momentum balance will be decomposed into a jet flow and an undisturbed pipe flow. This is discussed in Chapter 4.

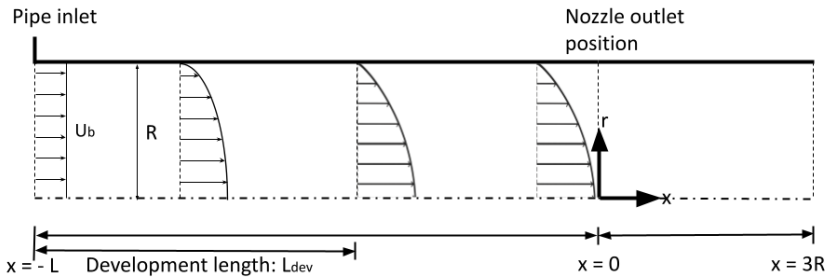
Numerically, the relation between upstream flow development and downstream formation of a jet will be investigated using the Computational Fluid Dynamics (CFD) finite-volume (FV) solver OpenFOAM version 13. Experimental data to validate the simulations and compare results are given by references [8] and [10]; recent numerical data is obtained from ref. [3].

The undisturbed long pipe flow serves as a reference simulation for the hydrodynamic development of the velocity profile, whereas the jet simulations incorporate the effects of the nozzle outlet perturbations next to this. Comparing both the flow fields allows to isolate the influence of these outlet-induced perturbations.

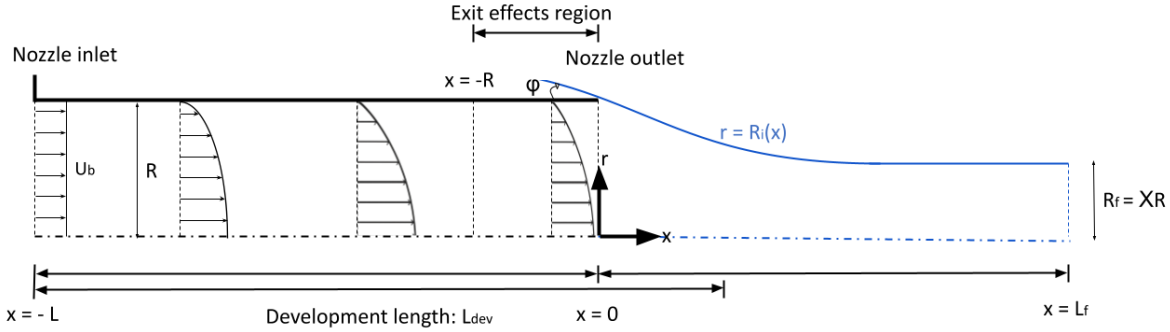
A total of 56 combinations of Reynolds number and nozzle length were investigated, covering the range $4.2 \leq Re \leq 400$, each consisting of two numerical simulations: an undisturbed, long pipe flow without exit effects (Fig. 1.2a) and a nozzle flow of length L, under the influence of exit effects, containing a downstream jet formation (Fig. 1.2b). Four nozzle lengths are investigated, normalized by the nozzle radius R: $L/R = 1.94$, $L/R = 2.00$, $L/R = 5.16$ and $L/R = 21.4$. Three of the lengths considered were experimentally investigated by Gavis and Modan [8]; the nozzle of length $L/R = 2.00$ is added, because this corresponds to a nozzle length-to-diameter ratio of exactly one.

In addition to this, the influence of surface tension on the final jet contraction ratio is examined through a Weber number sensitivity study, performed using both the integral momentum balance reconstruction and additional OpenFOAM simulations at increased Weber numbers, for a selection of Reynolds numbers. This investigation assesses whether capillary effects contribute to the quantitative difference between numerical contraction ratios and the experimental results by Gavis and Modan [8], in particular at higher Reynolds numbers.

First, existing experiments and past numerical research will be discussed in Chapter 2. Then, the numerical approach (Chapter 3) is discussed, after which an analytical decomposition of the integral momentum balance for a jet flow is derived in Chapter 4. Finally, additional numerical results are given and discussed (Chapters 5 to 9).



(a) Flow domain for an undisturbed pipe flow in an extended nozzle of length $L + 3R$.



(b) Flow domain for the jet flow, ejected from a nozzle of length L.

Figure 1.2: Flow domains.

2. Literature

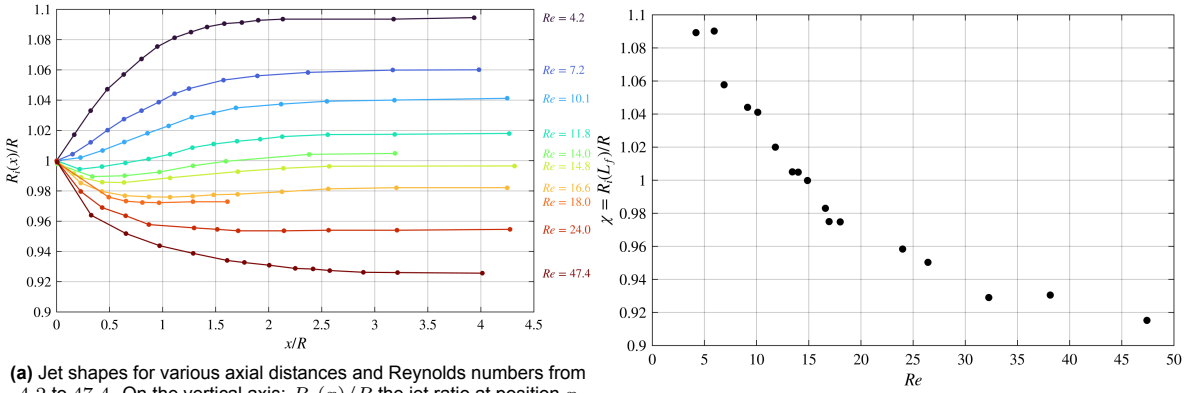
This chapter will give an overview of past research that has been done on the topic of laminar liquid jets. First, experiments and previous numerical research for fully developed jet flow will be discussed. Then, experimental results for undeveloped jet flow is discussed.

2.1. Fully developed long nozzle flow

2.1.1. Experimental research

Several experimental studies on the topic of Newtonian fully developed die-swell has been performed over the last 60 years. The experimental results by Middleman and Gavis [20] indicate that the final jet contraction ratio χ is a function of velocity and viscosity, in other words, a function of the Reynolds number. The experimental results showed expanding behaviour for $Re < 16$, whereas the jets contract for $16 < Re < 150$. As $Re \to \infty$, the ratio approached Harmon's [12] theoretical limit of $\frac{R_f}{R} = \frac{\sqrt{3}}{2}$. According to Middleman and Gavis, the expanding and/or contracting behaviour is due to velocity profile relaxation: the dimensionless axial velocity gradient $\partial\tilde{u}/\partial\tilde{x}$ is zero in the nozzle, but becomes finite as soon as the fluid leaves the nozzle. To satisfy the integral momentum balance in the jet, a change in velocity profile must be accompanied by a change in diameter or radius. Later, we will see that this is not the case; $\partial\tilde{u}/\partial\tilde{x}$ is nonzero close to the nozzle outlet. This transition upon exiting the nozzle was found to be related to the no-slip to free-slip condition change, discussed in detail by Richardson [27]. Essentially, a discontinuity arises in the stress distributions as the liquid separates from the nozzle wall.

In similar fashion, Goren and Wronski [10] experimentally investigated the shape of low-speed Newtonian capillary jets, ejected from a long nozzle, in 1966. For $4.2 < Re < 47.4$, they measured jet profiles as a function of axial distance away from the nozzle exit. Their results are shown in Figure 2.1a, for a glycerol-water mixture, ejected from an 18.1 mm diameter nozzle. Later in this thesis, we will see that the diameter on its own does not matter; only the ratio of the nozzle length with respect to diameter or radius matters. Monotonic contraction occurs for $Re \gtrapprox 17$. Below $Re \lessapprox 12$, the jet experiences expansion. The interesting thing happens for $12 < Re < 17$, where the jet first contracts and then expands. In the numerical analysis by Breugem and Kamis [3], this was attributed to competing viscous and inertial effects, dominant in respectively the low and high Reynolds number regimes and which tend to respectively expand and contract a jet.



(a) Jet shapes for various axial distances and Reynolds numbers from 4.2 to 47.4. On the vertical axis: $R_i(x)/R$ the jet ratio at position x and on the horizontal axis: x/R the dimensionless axial distance away from the nozzle exit.

(b) Final jet contraction ratio χ vs Reynolds number showing the exponential decay, as reported in ref. [10].

Figure 2.1: Experimental results for a fully developed Newtonian jet, adapted from Goren and Wronski [10].

As the Reynolds number increases, the jet radius decreases exponentially as a function of distance towards the final equilibrium radius. This is shown in Figure 2.1a for Re up to 47.4. The proof of exponential decay was found by performing a linear perturbation analysis of the Navier-Stokes equations with respect to the final plug flow state, i.e. just before it breaks up. In the linear perturbation analysis, the authors found a discontinuity for $16 < Re < 20$, which they attribute to a complex damping coefficient. However, apart from the possible neglect of higher order terms, no detailed explanation of this was given in their article.

2.1.2. Theoretical contraction ratio limit

Harmon [12] developed a theoretical limit for the final radius ratio of a low-speed capillary jet. A number of assumptions were made: a fully developed cylindrical nozzle flow, no drag from the environmental fluid and no gravitational effects. By conserving mass and momentum along the jet, his result indicated a theoretical limit to the final contraction ratio and average velocity:

$$\chi = \frac{R_f}{R} = \frac{\sqrt{3}}{2} \tag{2.1}$$

$$\frac{U_f}{U_b} = \frac{4}{3} \tag{2.2}$$

The subscript 'f' indicates the final condition, far downstream of the nozzle exit. Equations 2.1 and 2.2 show that, as the jet contracts, the average velocity increases. This momentum balance only takes changes in velocity in the inertial regime into account and thus always predicts a contracting jet. The experiments by Middleman and Gavis [20] and Goren and Wronski [10] show experimental proof of this limit for $Re \to \infty$; however, they have shown that, a jet expands at lower Reynolds numbers.

2.1.3. Numerical research

Over the past 50 years, various numerical research has been done on the topic of laminar liquid jets. One of the first simulations performed were the Finite Element Method (FEM) models by Nickell et al. [23], who modelled creeping, low Reynolds number jets ($Re < 10^{-8}$) without surface tension. Particular focus in their numerical approximation was on the stick-slip singularity at the nozzle edge. They dealt with the problem by refining the grid around the nozzle edge.

Reddy and Tanner [26] modelled the effect of surface tension for Reynolds numbers up to 50; their results for the final jet radius are shown in Fig. 2.2, showing a decreasing jet ratio as the Reynolds number increases; a similar shape to Fig. 2.1b by Goren and Wronski. Moreover, the gradient of the curve changes between $Re = 10$ and $Re = 20$, indicating a transition from an expanding to a contracting jet, as seen in the experiments by Goren and Wronski. As in the research by Nickell et al., the mesh was refined accordingly to work around the stress singularity at the nozzle tip.

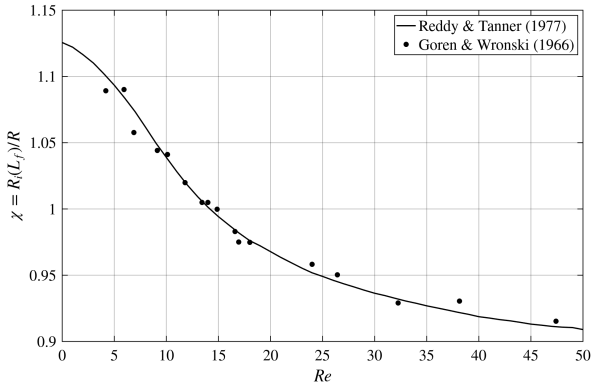


Figure 2.2: Results of FEM simulations by Reddy and Tanner. Jet radius as a function of Reynolds number, adapted from [26].

Omodei [24] also performed FEM simulations for $10^{-3} < Re < 1000$, with particular focus on the effect of surface tension. In their results for the jet profiles, similar behaviour as in the experiments by Goren and Wronski [10] and Middleman and Gavis [20] is noticeable, where the jets expand at low Reynolds numbers and contract for higher Reynolds numbers.

More recently, Breugem and Kamis [3] performed Finite Volume (FV) simulations, with the aim to find the physical mechanisms for the expansion and contraction behaviour of laminar liquid jets at $4.2 < Re < 47.4$. The simulated cases are presented in Table 2.1, with the results for the jet interface profiles shown in Fig. 2.3.

Re	We	Ca	Fr
4.2	16.1	7.7	10.1
7.2	45.8	12.7	17.0
10.1	88.5	17.5	23.6
11.8	118.2	20.0	27.3
14.0	164.2	23.5	32.1
14.8	182.0	24.6	33.8
16.6	225.6	27.2	37.7
18.0	262.9	29.2	40.7
24.0	458.6	38.2	53.7
47.4	1733.8	73.2	104.4

Table 2.1: Governing dimensionless numbers of the simulated cases [3]. $We \gg 1$, $Ca \gg 1$ and $Fr \gg 1$ for most cases indicating negligible effects of surface tension and gravity, respectively.

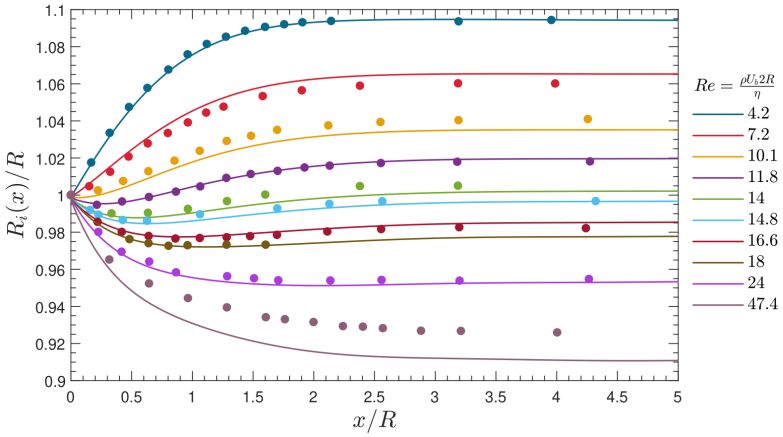


Figure 2.3: Numerical results for the normalized jet radius as function of normalized axial distance from the nozzle exit for the cases in Table 2.1 [3]. The dots represent experimental results by Goren and Wronski [10], the lines correspond to numerical results by Breugem and Kamis [3].

The jet profiles are in agreement with the experimental results of Goren and Wronski [10] and the numerical results of Omodei [24], showing the same transition Reynolds number of $Re \approx 14$, where the jet switches from expansion to contraction. The numerical results and derivation of an integral momentum balance indicate that expanding jets at low Re are due to a radial outward velocity, a compressive normal stress at the interface just downstream of the nozzle and an additional integral wall shear stress within the nozzle, due to the stick-slip transition.

The two-dimensional velocity contour plots around the nozzle exit are shown in Figure 2.4, for an expanding jet ($Re = 4.2$), an expanding and contracting jet ($Re = 14$) and a contracting jet ($Re = 24$). Just downstream of the nozzle exit, a positive radial velocity exists. This is the consequence of an increased axial velocity at the nozzle exit due to the stick-slip transition as a result of mass conservation across the radial interface. As the Reynolds number increases to $Re = 24$, the axial velocity magnitude increases and the radial momentum gets advected downstream, causing the higher amount of smearing in the contours.

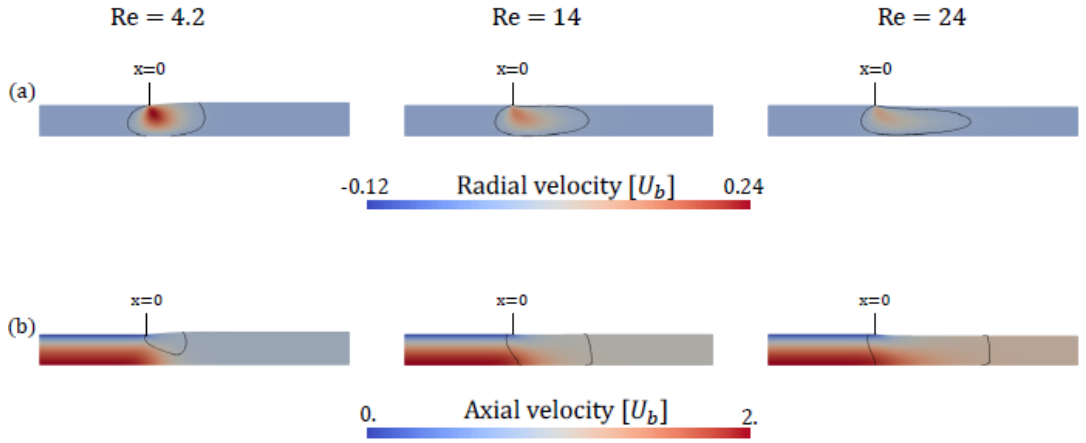


Figure 2.4: 2D flow field plots of the magnitude of the radial (a) and axial (b) velocity in units of U_b (bulk velocity) in the nozzle and the jet for $Re = 4.2$, 14 and 24, from left to right, respectively. [3]

At low Reynolds numbers, the changes in radial velocity, normal and wall shear stresses cause a reduced integral axial momentum flux at the nozzle. To maintain the integral momentum balance, the jet must expand.

2.2. Short nozzle flow

The following section discusses experimental research by Gavis and Modan [8] on flow from short nozzles, as well as pipe flow development and exit effects.

2.2.1. Experimental research on the effect of tube length

In the previous section, the nozzles were assumed to be sufficiently long for the flow to fully develop inside the nozzle. Gavis and Modan [8] performed experiments in the 1960s to find the influence of nozzle length on the jet contraction ratio. For six different nozzle length to radius ratios, L/R, and Reynolds numbers up to 1000, the final jet radius ratio was measured. Their observed values of χ, as a function of Re and L/R are shown in Figure 2.5 for a selection of cases.

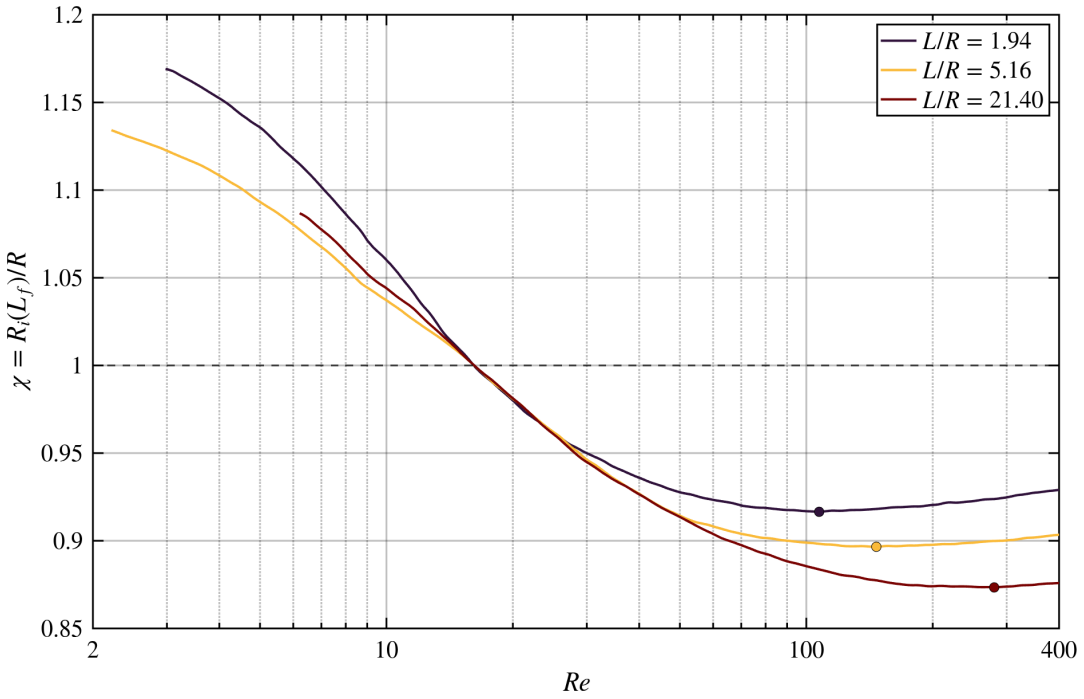


Figure 2.5: Final jet ratio at different Reynolds numbers and L/R-ratios, adapted from Gavis and Modan [8]. The dots represent the minimum value of the curves.

For all Reynolds numbers, the experimental curves for χ show a nozzle-length dependence. The curves shown represent constant viscosity cases. In their original results (Fig. 1 in ref. [8]), the data for χ shows a lot of scatter for low Reynolds numbers; particularly for $L/R = 1.94$. Gavis and Modan attributed this to possible lack of flow development in the nozzle and exit effects upstream of the nozzle exit for short nozzles. Another possible explanation for the scatter is the temperature dependence of the viscosity. The authors mention the experiments were run as close to $25°C$ as possible, but no attempt was made to actively control the temperature. For the viscous dominated regimes, this might suggest interaction between exit effects, upstream of the nozzle outlet, and the development of the jet, downstream of the nozzle outlet.

Figure 2.5 shows that, all L/R-curves collapse onto a single curve in the intermediate Reynolds number regime. The critical Reynolds number, where the jet transitions from expansion to contraction, appears to lie in between $Re \approx 12 - 16$, as seen in the results of other numerical and experimental research for a constant nozzle length ([3], [9]). This suggests that the transition Reynolds number is independent of L/R.

As the Reynolds number is increased beyond $Re \approx 20$, the χ-curves start to decrease until they reach a minimum after $Re \approx 100$, visible in Fig. 2.5 by the dots, after which the jet ratio for all geometries starts to increase again. Gavis and Modan attribute this phenomenon to a lack of flow development, which is supported by the integral momentum balance by Breugem and Kamis [3] in their numerical research into the effect of the Reynolds number on laminar liquid jets.

2.2.2. Flow development

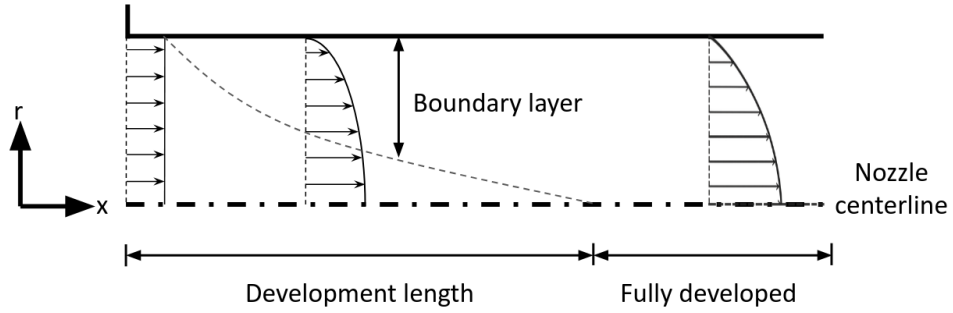


Figure 2.6: Schematic visualisation of flow development in a pipe.

Nozzle flow development occurs in the hydrodynamic development region. In this region, viscous boundary layers are distinct and the velocity profile is dependent on both the radial and the axial coordinate. When the nozzle flow is fully developed, the velocity profile only depends on the radial coordinate and becomes of the parabolic Poiseuille shape. [18] Assuming a uniform inflow velocity U_b, the centerline velocity will become $2U_b$ at the end of the development length L_{dev}.

Various correlations exist for the development length L_{dev} of laminar pipe flow, with $\frac{L_{dev}}{D} = 0.06Re$ [28] being probably the most widely used. Equation 2.3 [6], for example, also takes axial diffusion into account and should result in more accurate results for $Re < 100$.

$$\frac{L_{dev}}{R} = 2\left[(0.619)^{1.6} + (0.0567\,Re)^{1.6}\right]^{\frac{1}{1.6}} \tag{2.3}$$

In Figure 2.7, the dimensionless hydrodynamic development length L_{dev}/R is shown as a function of Reynolds number.

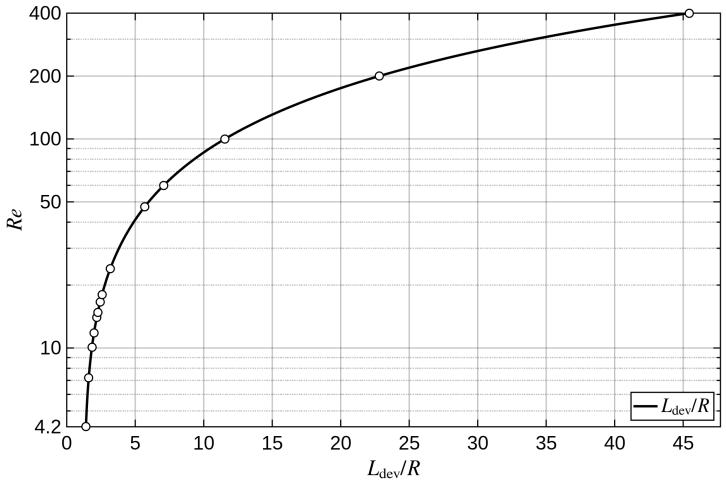
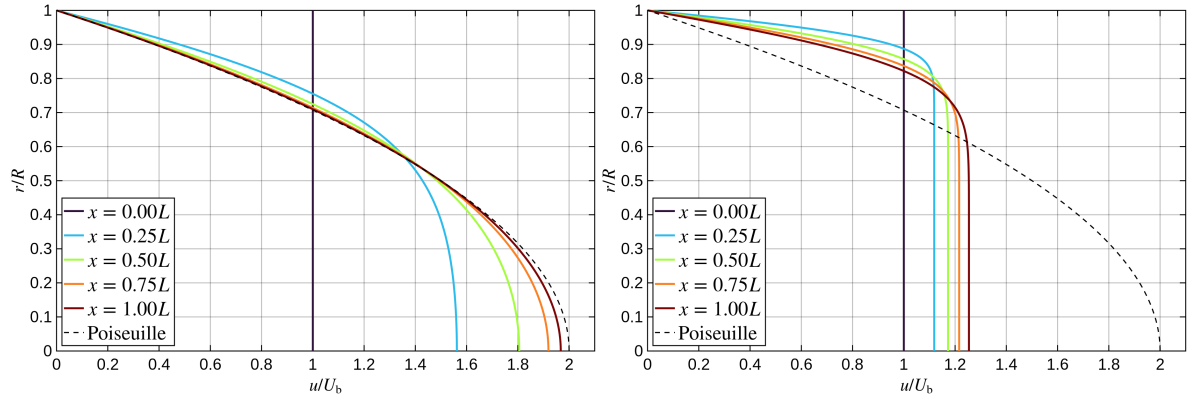


Figure 2.7: Hydrodynamic development length vs Reynolds number (Eq. 2.3). The dots represent the Reynolds numbers investigated.



(a) $Re = 24$. **(b)** $Re = 400$.

Figure 2.8: Axial velocity profiles at sample locations each increased by 25%, for $Re = 24$ (a) and $Re = 400$ (b), ejected from a nozzle of length $L = 1.94R$, illustrating the development of the velocity profiles for two different Reynolds numbers in the same geometry.

The development of the axial velocity profile along the nozzle length is illustrated in Figure 2.8, for $Re = 24$ and $Re = 400$, both for a nozzle of length $L = 1.94R$. Five sample locations, each in increments of 25% of L are presented. The velocity profiles shown are obtained using the entry-flow approximation proposed by Lew [19], discussed in more detail in Chapter 4.2 and assuming a uniform velocity profile at the nozzle inlet (U_b). The initially uniform velocity distribution develops towards a Poiseuille profile due to viscous momentum diffusion. The rate at which this happens depends on the Reynolds number, with a faster development occurring at lower Reynolds numbers.

At $Re = 24$, the velocity profile approaches a fully developed Poiseuille profile within the nozzle length, though it does not reach the centerline velocity of $2U_b$, indicating that it has not fully developed yet. At $Re = 400$, the profile is considerably more undeveloped, showing plug-like profiles at all sample locations.

The hydrodynamic development influences the axial momentum flux across the nozzle cross-section. The difference in axial momentum flux at the nozzle outlet is relevant to the integral momentum balance, governing the downstream expansion or contraction behaviour of the jet. Upon exiting the nozzle, the no-slip stress boundary condition at the wall is replaced by an interfacial free-slip stress boundary condition, which results in a redistribution of the axial velocity profile. The initial momentum flux getting redistributed across the cross-section, just downstream of the nozzle outlet, depends on the hydrodynamic flow development within the nozzle. A more developed profile is characterized by a larger axial momentum flux, resulting in more contraction.

3. Computational method and setup

The following chapter will go over the numerical methodology and setup used in the research on laminar liquid jets using the open-source Computational Fluid Dynamics (CFD) package OpenFOAM.org, version 13, including the interface reconstruction method, stability criteria, computational mesh and the initial and boundary conditions. For numerical settings and discretization methods in more detail, see Appendix C.

3.1. The Volume Of Fluid method

The Volume Of Fluid (VOF) method is a free-surface modelling technique, to track a free surface between two fluids. It was first introduced by Nichols and Hirt [22] in 1975, but described in more detail in their publication from 1981 [14].

In this thesis, the two fluids considered are water (fluid A) and air (fluid B). A discontinuous function $\alpha(x, r, t)$ is introduced to discretize the interface between A and B, for which:

- $\alpha = 1$ in fluid A (water);
- $\alpha = 0$ in fluid B (air);
- $0 < \alpha < 1$ in the surface cells, where both air and water exist.

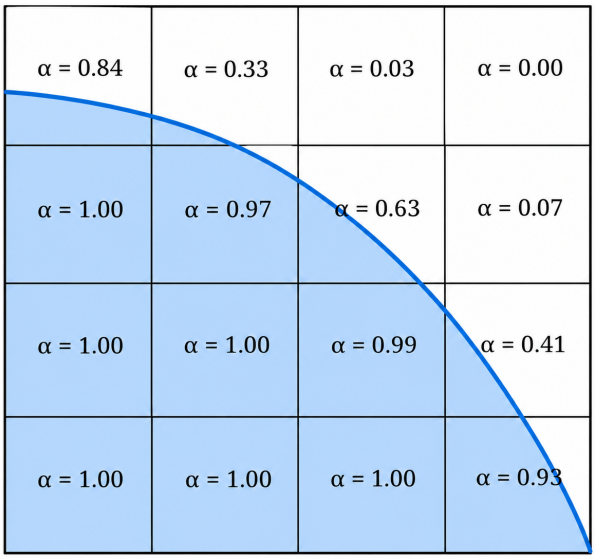


Figure 3.1: Volume-of-Fluid methodology: Sketch of the average analytical volume fractions for a curved interface on a fixed grid, adapted from [4] and generated with help of AI. The blue curve indicates the liquid-gas interface.

Using the function $\alpha(x, r, t)$, the local kinematic viscosity in the surface cells can be expressed as $\nu = \alpha\nu_{water} + (1 - \alpha)\nu_{air}$. Density and other fluid parameters can be expressed in way analogous to this.

The advection of the surface is governed by:

$$\frac{\partial \alpha}{\partial t} + u_x \frac{\partial \alpha}{\partial x} + u_r \frac{\partial \alpha}{\partial r} = 0 \tag{3.1}$$

3.2. Surface reconstruction

Surface reconstruction can be done in various ways, such as the Compressive Flux Model (*interfaceCompression* in OpenFOAM) or Piecewise Linear Interface Calculation (PLIC). In this thesis, the PLIC method was used. This is a geometric interface reconstruction method, where the interface is discretized in small line segments. A single line segment is represented by $\boldsymbol{x} \cdot \hat{\boldsymbol{n}} = \zeta$, where $\boldsymbol{x}$ represents the position vector of a line point, $\hat{\boldsymbol{n}}$ the unit normal w.r.t. the line and ζ a line constant. The line constant ζ is generally calculated iteratively [7].
The geometric PLIC method was introduced in OpenFOAM-v8 [11], [17]. Figure 3.2 shows a sketch where the interface (in blue in Fig. 3.1) is split up in linear line segments, each segment being in a computational cell.
Numerically, the interface is defined as the positions in the computational domain where the VOF function α is equal to 0.5.

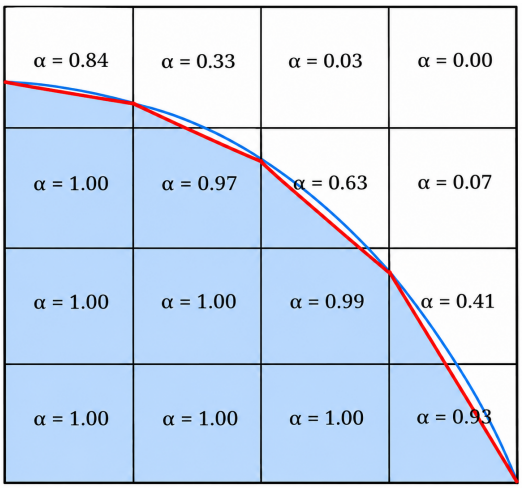


Figure 3.2: Volume-of-Fluid methodology: Piecewise Linear Interface Calculation from volume fractions, adapted from [4] and generated with help of AI. The red lines represent the liquid-gas interface split into multiple linear line segments.

3.3. Surface tension model

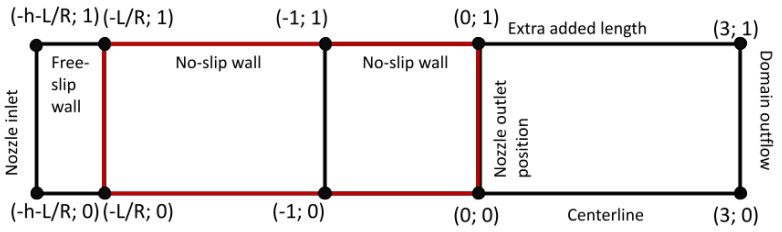
In the solver module *incompressibleVoF*, surface tension in the Laplace equation is modelled by the Continuum Surface Force (CSF) model by Brackbill et al. [2]. In the CSF model, surface tension is modelled as a 3D, continuous variable across an interface, where the Laplace equation becomes a vector equation. The details to the CSF model are given in Deshpande et al. [5] and Brackbill et al. [2].

3.4. Computational grid

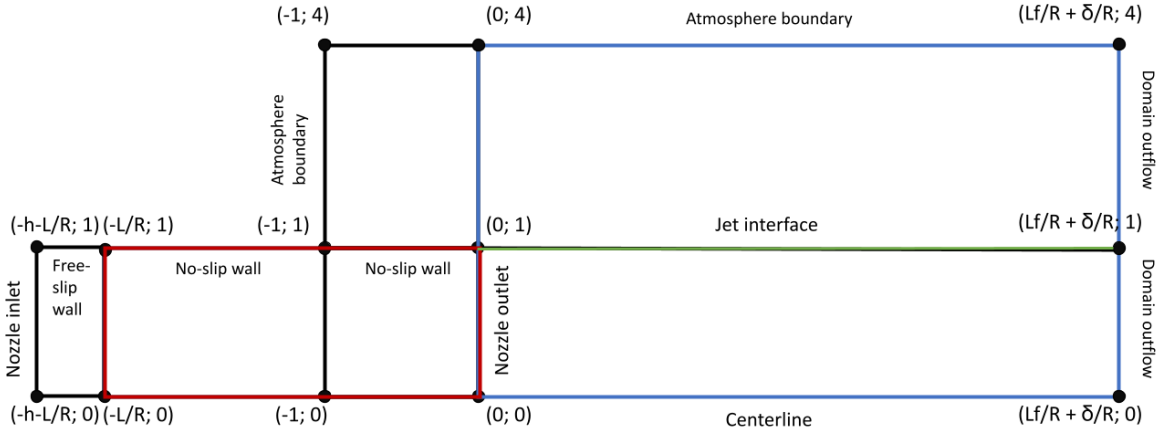
The computational grid is created using the *blockMesh* utility, shipped with OpenFOAM. The *blockMeshDict*, the dictionary governing the mesh is given in Appendix C. The grid is made up of four, resp. six blocks for the pipe and jet cases and is made dimensionless using the nozzle radius R as the characteristic length scale. As a consequence, the length of the nozzle is equal to L/R.

Sketches of the two grids are shown in Figures 3.3a and 3.3b. The highlighted red area represents the (actual) nozzle. The block from $-h$ upstream of the red-highlighted actual nozzle represents the inflow region, where a free-slip boundary condition is applied. This makes the nozzle in which the flow is computed slightly longer than the actual, experimental nozzle length.

In both the jet and the pipe cases, the domain is an axisymmetric wedge, since the situation in question is axisymmetric. The cell size imposed is $\Delta x/R = \Delta r/R = 1/40$. In OpenFOAM, the cell size was inserted as a function of the nozzle length (Cell count in block n $=$ Length of block n$/$cellSize) and is independent on the Reynolds number. As a consequence of this, the cell count varied from 104720 cells for the shortest nozzle to 135840 for the longest nozzle. At the nozzle wall and the jet interface, mesh refinement leads to a radial cell size of $\Delta r/R = 1/400$ and at the outlet cross-sectional plane an axial cell size of $\Delta x/R = 1/200$. To test the sensitivity of the grid resolution on the problem, several simulations were run with a mesh resolution of $\Delta r/R = 1/80$ for the Reynolds numbers $Re = 11.8$, $Re = 14.0$, $Re = 14.8$ and $Re = 47.4$. The interface profiles are presented in Figure A.1 in Appendix A and show negligible effect of increasing the mesh resolution in radial direction.



(a) Sketch of the long pipe flow simulations mesh, illustrating the extra added length for $x > 0$, after the actual nozzle outlet.



(b) Sketch of the jet simulations mesh. The blue highlighted zone represents the atmospheric gas region. The green highlighted line illustrates the jet interface. The six different blocks represent the mesh blocks, where different boundary conditions can be applied in OpenFOAM.

Figure 3.3: Sketch of the two computational grids. All coordinates are normalized by the nozzle radius R, with the origin at the center of the outlet plane. The red highlighted region represents the actual nozzle.

Two types of grids are used; one for long pipe simulations, one for jet simulations. In the long pipe grid, Figure 3.3a, the pipe is of dimensionless length $L/R+3$, to avoid any upstream exit effects. For the jet grid, Figure 3.3b, the domain downstream of the nozzle exit has a length of $L_f/R + \delta/R$, where δ/R is a chosen length scale added to the final jet length L_f. It depends on the Reynolds number, and is used to give the jet space to develop and to reduce the numerical end-of-domain effects. The grids for higher Reynolds numbers used a larger δ.

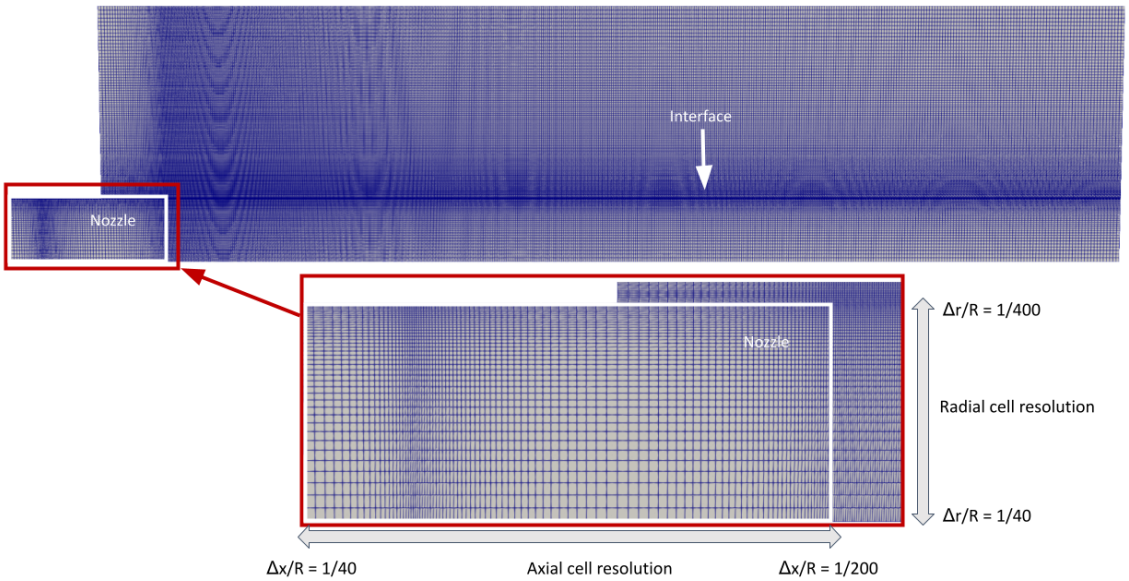


Figure 3.4: Computational grid used for the numerical simulations for a nozzle of length $L = 1.94R$. The other geometries are built using an equal grid resolution. The red highlighted zone represents the region around the nozzle, with grid refinements near the wall and the nozzle outlet plane.

3.5. Initialization and boundary conditions

At the nozzle inlet plane, a uniform velocity in axial direction and a VOF coefficient of one were imposed. The pressure boundary condition was set to a zero normal gradient condition, allowing the pressure to vary over the plane.
At the far-field atmosphere boundaries, the velocity and VOF coefficient were set to a zero gradient boundary condition and the pressure was set to $p = 0$, which is effectively the atmospheric pressure.
At the domain outflow, a zero gradient condition for velocity, pressure and VOF coefficient was imposed, allowing the variables to vary over the jet interface here.

In the nozzle and the extra added length, a no-slip velocity boundary condition is applied at the walls, except for the inlet region, for $x/R < -L/R$, see Figure 3.3. Here, a free-slip boundary condition is imposed, to avoid adverse effects of the discontinuity created by immediately imposing a no-slip stress condition while simultaneously imposing a constant velocity at the nozzle inlet. Also, this simulates a real inflow more accurately, for example from a reservoir into the nozzle. For the pressure and VOF coefficient, a zero gradient was imposed.

Initialization was done by imposing a VOF coefficient of $\alpha = 1$ for $r < R$ and $-L < x < L_f$. Velocity inside the jet and nozzle was initialized with a uniform velocity profile $(1, 0, 0)$ and the internal jet pressure was set equal to the pressure due to surface tension: $p = 2\sigma/R = 2 \cdot 0.07/1 = 0.14$. However, this expression corresponds to a spherical interface, whereas the pressure difference across a cylindrical liquid jet is half this. This was identified after the numerical simulations have been completed. Consequently, all results presented in the following chapters were obtained using the original pressure initialization. Although this might have influenced the initialization, its effect on the actual converged numerical simulations has not been quantified.

The flow parameters all depend on the Reynolds number and were set accordingly in the numerical settings using $\nu = 2U_bR/Re = 2/Re$.

3.6. Numerical stability and time step

The computational time step Δt is determined by the constraint based on the Courant number and the capillary-inertia stability criteria, as discussed by Ooms et al. [25] in their publication on core-annular flow, albeit in a slightly different form, since the density of the surrounding fluid is negligible compared to the liquid inside the jet:

$$\Delta t^{Max} = min\left(\Delta t_{Co}^{Max}, \Delta t_{Cap}^{Max}\right) \tag{3.2}$$

$$\Delta t_{Co}^{Max} = \frac{Co_{max} \cdot \Delta x_i}{u_i} \tag{3.3}$$

$$\Delta t_{Cap}^{Max} = \tau_I \frac{\sqrt{2}}{2} \frac{\Delta x_i^2}{\pi R^3} \tag{3.4}$$

$$\tau_I = \sqrt{\frac{\rho_w R^3}{\sigma}} \tag{3.5}$$

In the stability criteria above, Co_{max} is the maximum advection-based Courant number. u_i is the relevant advection velocity, in this case the constant uniform inflow velocity U_b, which is also used to initialize the velocity field in the simulations. Δx_i is the grid size in the relevant advection direction, which, since the simulations use an equal grid size in both the axial and radial direction, is equal to Δx.

Equation 3.4 is the maximum time step allowed for capillary-inertia dominated instabilities, based on the stability analysis for the Continuum-Surface-Force (CSF) model [2]. τ_I is the capillary-inertial timescale, required to stably resolve capillary-inertial waves of wavelength $2\Delta x$ travelling along the surface. Moreover, this criterion also governs the growth of parasitic currents on the interface [5]. Using $Co_{max} = 0.02$, $u_i = 1$, $\Delta x_i = 1/40$, $\rho_w = 1$, $R = 1$ and $\sigma = 0.07$ leads to a $\Delta t^{Max} = 5e^{-4}$.

In OpenFOAM, these stability criteria are enforced by setting the parameters in the *controlDict*, *fvSolution* and *fvSchemes* dictionaries. Most settings were left standard, but the stability criteria were enforced using the *adjustableRunTime*, *adjustTimeStep*, *maxCo*, *maxAlphaCo* and *maxDeltaT* settings in the *controlDict* dictionary. *maxDeltaT* is the maximum allowable timestep to guarantee numerical

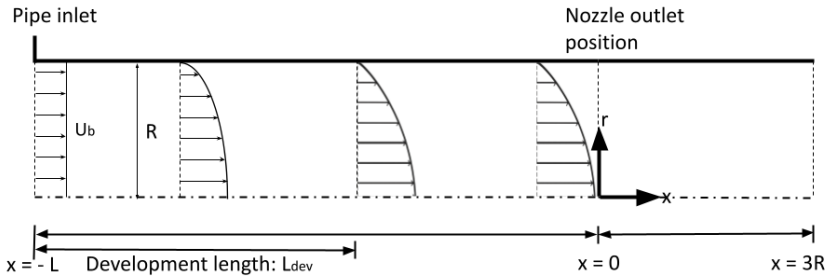
stability. OpenFOAM then reads the maximum user-imposed values and changes the local (in time) Δt accordingly. The maximum values set were: $\Delta t^{Max} = 5e^{-4}$, calculated based on Eq. 3.2, *maxCo* $= 0.02$ and *maxAlphaCo* $= 0.1$. The production simulations were run using a first-order implicit Euler scheme, until the jet radius has become constant, far enough downstream of the nozzle exit. For detailed numerical settings, see Appendix C.

4. Integral momentum balance

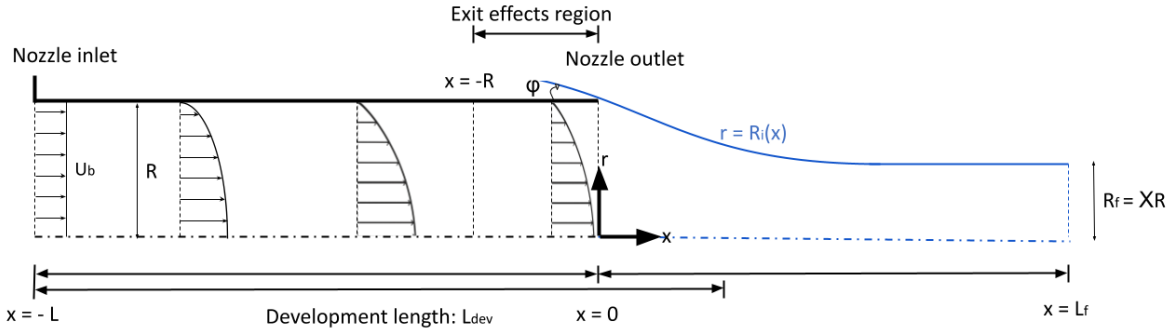
In the following chapter, the integral momentum balance for a jet emerging from a short nozzle will be derived, with the aim to provide a framework for, and make a clear distinction between, flow development effects and outflow effects and their relation to the jet expansion or contraction ratio χ.

To find the influence of nozzle exit effects and possible undeveloped effects, the balance is decomposed into two parts, assuming the exit perturbations are small. The decomposed integral momentum balance consists of a base flow and a perturbation flow. The base flow represents a flow in an extended nozzle or pipe, either developed or undeveloped, but without outflow effects. The perturbation flow exists due to nozzle outflow effects. These two flows added together form the jet flow, in other words subtracting the base flow from the jet flow results in the perturbation flow.

The two flows are sketched in Figures 4.1a and 4.1b. Figure 4.1a corresponds to an undisturbed flow for a long pipe of length $L + 3R$, without outflow effects. For $L \gg L_{dev}$, the flow is hydrodynamically developed and the velocity profile will be a Poiseuille flow at the end of the development region. For $L \ll L_{dev}$, the flow is undeveloped and the effects of flow development come into effect. Figure 4.1b corresponds to a jet, ejected from a nozzle of length L. The exit region is assumed to be $1R$ upstream of the nozzle exit. In this case, the flow upstream of the nozzle outlet will be affected by outflow effects as a consequence of the transition from a no-slip nozzle wall to a free-slip liquid-gas interface downstream of the nozzle exit. Furthermore, the upstream hydrodynamic development stage of the flow will be relevant in determining the momentum flux at the nozzle outlet.



(a) Flow domain for an undisturbed pipe flow. A length of $3R$ is added to the nozzle length L, to ensure no outflow effects.



(b) Flow domain for the jet flow, ejected from a nozzle of length L. The exit region is assumed to be $1R$ upstream of the nozzle exit.

Figure 4.1: Flow domains for the decomposed integral momentum balance.

As in the fully developed flow case, studied by Breugem and Kamis [3], the steady state incompressible conservation equations apply. Since the jet considered is purely horizontal, gravity is negligible [3].

$$\nabla \cdot \boldsymbol{u} = 0 \tag{4.1}$$

$$\rho \nabla \cdot (\boldsymbol{u}\boldsymbol{u}) = -\nabla p + \nabla \cdot \boldsymbol{\tau} \tag{4.2}$$

$\boldsymbol{u}$ is the velocity vector, $\boldsymbol{\tau} = \mu\left[\nabla\boldsymbol{u} + \nabla\boldsymbol{u}^T\right]$ the Newtonian viscous stress tensor. The nozzle is of length L and radius R.

At the inlet of the nozzle and pipe, $x = -L$, a uniform plug flow velocity profile with magnitude U_b is assumed. The momentum flux here is $\dot{M}_{inlet}$.

For a long nozzle or pipe, $L \geq L_{dev}$, this uniform velocity profile will develop into a parabolic Poiseuille profile within the development region, as given by Equation 2.3. For a short nozzle or pipe, $L \leq L_{dev}$, the flow has insufficient axial length to develop. As a result, the radial velocity profile inside the nozzle will be flatter and more plug-like.

In the nozzle flow, Figure 4.1b, the outlet axial momentum flux at $x = 0$ is $\dot{M}_{outlet}$. For the pipe flow, Figure 4.1a, the axial momentum flux at the position of the nozzle outlet is $\dot{M}^{EN}_{outlet}$. The distinction between the perturbed, nozzle outlet momentum flux $\dot{M}_{outlet}$ and the undisturbed, pipe flow outlet momentum flux $\dot{M}^{EN}_{outlet}$ allows us to quantify the degree of development at the position of the nozzle outlet with respect to a fully developed homogeneous Poiseuille flow.

At $x = L_f$, the jet attains its final radius $R_f = \chi R$, where χ is the jet expansion or contraction ratio. The momentum flux at the final downstream position of the jet will be $\dot{M}_f$.

σ is the surface tension coefficient and $\kappa_0 = cos\varphi/R - R_i"(0)cos^3\varphi$ is the interface curvature at the nozzle exit. τ_{xr} is the wall shear stress in the nozzle and $R_i"(0) = d^2R_i/dx^2_{|x=0}$ is the second derivative of the local jet radius with respect to x, just downstream of the nozzle outlet.

In the derivation, upstream is referred to as $x < 0$, downstream $x > 0$. The superscript EN refers to the extended nozzle in the undisturbed long pipe flow.

4.1. Derivation

For the undisturbed pipe flow, the integral momentum balance for $-L < x < 0$ is:

$$\dot{M}^{EN}_{outlet} - \dot{M}_{inlet} = \Delta p^{EN}\pi R^2 + \int_{-L}^{0} \tau^{EN}_{xr|r=R} 2\pi R dx \tag{4.3}$$

, where $\dot{M}_{inlet}$ and $\dot{M}^{EN}_{outlet}$ are the axial momentum fluxes at the pipe inlet and outlet, respectively. Δp^{EN} and $\tau^{EN}_{xr|r=R}$ are the pressure difference and wall shear stress, respectively, for a homogeneous, Poiseuille pipe flow.

The upstream integral momentum balance in the nozzle flow is:

$$\dot{M}_{outlet} - \dot{M}_{inlet} = -\left[p_{outlet} - p_{inlet}\right]\pi R^2 + \int_{-L}^{0} \tau_{xr|r=R} 2\pi R dx \tag{4.4}$$

, where $\dot{M}_{outlet}$ and $\dot{M}_{inlet}$ are the axial momentum fluxes at the nozzle inlet and outlet, respectively.

By subtracting Eq. 4.3 from Eq. 4.4, $\left(\dot{M}_{outlet} - \dot{M}_{inlet}\right) - \left(\dot{M}^{EN}_{outlet} - \dot{M}_{inlet}\right)$, the upstream integral perturbation momentum balance, with respect to a fully developed homogeneous Poiseuille flow, becomes:

$$\dot{M}_{outlet} - \dot{M}^{EN}_{outlet} = \pi R^2\left[p_{inlet} - p_{outlet} - \Delta p^{EN}\right] + \int_{-L}^{0}\left(\tau_{xr|r=R} - \tau^{EN}_{xr|r=R}\right) 2\pi R dx \tag{4.5}$$

The integral momentum balance for the jet, downstream of the nozzle outlet ($0 < x < L_f$) is:

$$\dot{M}_f - \dot{M}_{outlet} = \left[p_{outlet} - (p_{atm} + \sigma\kappa_0)\right]\pi R^2 + \pi R\sigma\left[\chi - cos\varphi - RR_i"(0)cos^3\varphi\right] \tag{4.6}$$

, where $\dot{M}_f$ is the momentum flux at the final downstream position of the jet.

Combining the upstream and downstream balances (Eq. 4.5 and 4.6) results in the total integral momentum balance:

$$\dot{M}_f - \dot{M}^{EN}_{outlet} = \pi R^2\left[p_{inlet} - (p_{atm} + \sigma\kappa_0) - \Delta p^{EN}\right] + \int_{-L}^{0}\left(\tau_{xr|r=R} - \tau^{EN}_{xr|r=R}\right) 2\pi R dx + \pi R\sigma\left[\chi - cos(\varphi) - RR_i"(0)cos^3(\varphi)\right] \tag{4.7}$$

Subtracting $\dot{M}_{Pois} = \frac{4}{3}\pi\rho R^2 U_b^2$, which is the momentum flux representing a fully developed Poiseuille flow, from Eq. 4.7, moving $\dot{M}_{outlet}^{EN}$ to the right-hand side and substituting the expression for $\dot{M}_f = \frac{1}{\chi^2}\pi\rho R^2 U_b^2$ results in:

$$\frac{1}{\chi^2}\pi\rho R^2 U_b^2 - \underbrace{\frac{4}{3}\pi\rho R^2 U_b^2}_{\dot{M}_{Pois}} = \dot{M}_{outlet}^{EN} - \underbrace{\frac{4}{3}\pi\rho R^2 U_b^2}_{\dot{M}_{Pois}} + \pi R^2\left[p_{inlet} - (p_{atm} + \sigma\kappa_0) - \Delta p^{EN}\right] + \int_{-L}^{0}\left(\tau_{xr|r=R} - \tau_{xr|r=R}^{EN}\right)2\pi R dx + \pi R\sigma\left[\chi - cos(\varphi) - RR_i"(0)cos^3(\varphi)\right] \tag{4.8}$$

Dividing by $\rho\pi R^2 U_b^2$:

$$\frac{1}{\chi^2} - \frac{4}{3} = \frac{\dot{M}_{outlet}^{EN}}{\rho\pi R^2 U_b^2} - \frac{4}{3} + \frac{1}{\rho U_b^2}\left[p_{inlet} - (p_{atm} + \sigma\kappa_0) - \Delta p^{EN}\right] + \frac{2}{\rho R U_b^2}\int_{-L}^{0}\left(\tau_{xr|r=R} - \tau_{xr|r=R}^{EN}\right)dx + \frac{\sigma}{\rho R U_b^2}\left[\chi - cos(\varphi) - RR_i"(0)cos^3(\varphi)\right] \tag{4.9}$$

After nondimensionalizing Eq. 4.9, by using U_b as the characteristic velocity scale, R as the characteristic length scale and $\frac{\mu U_b}{R}$ as the characteristic scale for the pressure terms and viscous stresses, the result becomes:

$$\frac{1}{\chi^2} - \frac{4}{3} = \underbrace{\frac{\dot{M}_{outlet}^{EN}}{\rho\pi R^2 U_b^2} - \frac{4}{3}}_{\beta_{outlet}} + \underbrace{\frac{2}{Re}\left[\tilde{p}_{inlet} - \left(\tilde{p}_{atm} + \frac{\tilde{\kappa}_0}{Ca}\right) - \Delta\tilde{p}^{EN}\right] + \frac{4}{Re}\int_{-\tilde{L}}^{0}\left(\tilde{\tau}_{xr|\tilde{r}=1} - \tilde{\tau}_{xr|\tilde{r}=1}^{EN}\right)d\tilde{x}}_{\frac{\tilde{K}}{Re}} + \frac{1}{We}\left[\chi - cos(\varphi) - \tilde{R}_i"(0)cos^3(\varphi)\right] \tag{4.10}$$

where $\tilde{R}_i"(0) = RR_i"(0)$ is the dimensionless second derivative of the local jet radius and $\tilde{\kappa}_0 = R\kappa_0$ the dimensionless nozzle outlet curvature of the jet interface.

This results in the final, dimensionless equation for χ:

$$\frac{1}{\chi^2} - \frac{4}{3} = \beta_{outlet} + \frac{\tilde{K}}{Re} + \frac{1}{We}\left[\chi - cos(\varphi) - \tilde{R}_i"(0)cos^3(\varphi)\right] \tag{4.11}$$

Equation 4.11 is a dimensionless, implicit relationship for χ, allowing us to express the jet expansion or contraction ratio χ as a function of the degree of development at the position of the nozzle outlet, perturbed viscous effects and the capillary forces, which represent the three terms on the RHS in this particular order.

β_{outlet} represents the outlet development parameter with respect to a fully developed, homogeneous Poiseuille pipe flow, $\tilde{K}$ represents the perturbed viscous effects and the third term on the right-hand side of Eq. 4.11 represents the capillary effects.

Equation 4.11 can be rewritten to a 3rd degree polynomial:

$$A\chi^3 + B\chi^2 + C\chi + D = 0 \tag{4.12}$$

with $A = 2/Ca$ $B = \frac{4}{3}Re + \beta_{outlet}Re + \tilde{K} - \frac{2}{Ca}\left(cos\varphi + \tilde{R}_i"(0)cos^3(\varphi)\right)$, $C = 0$ and $D = -Re$, or, alternatively, an implicit root equation:

$$\chi = \frac{\frac{1}{2}\sqrt{3}}{\sqrt{1 + \frac{3}{4}\beta_{outlet} + \frac{3}{4}\frac{\tilde{K}}{Re} + \frac{3}{4We}\left[\chi - cos(\varphi) - \tilde{R}_i"(0)cos^3(\varphi)\right]}} \tag{4.13}$$

4.2. Analytical approximation

To analytically predict the influence of an undeveloped velocity profile on the downstream jet behaviour, the momentum flux at the position of the nozzle outlet, $\dot{M}_{outlet}^{EN}$ in the undisturbed pipe flow, is approximated by a series expansion, assuming no upstream outflow effects and negligible surface tension effects.

4.2.1. Entry flow equations

Lew [19] derived a velocity profile series expansion for a developing pipe flow by linearizing the entry flow equations around the nozzle exit and assuming a uniform velocity profile with magnitude U_b at the nozzle inlet. For this, the Navier-Stokes equations were linearized by retaining all terms of order $1/Re^2$ and greater and writing the nonlinear velocity terms as $\boldsymbol{u}\nabla u \approx U_b \partial u/\partial x$, where U_b is the uniform inlet velocity, which, according to the author's publication, is valid for $20 < Re < 400$. The result is given by Eq. 4.17 [19].

$$\frac{\partial u}{\partial t} + U_b \frac{\partial u}{\partial x} = -\frac{1}{\rho}\frac{\partial p}{\partial x} + \nu \frac{1}{r}\frac{\partial}{\partial r} r \frac{\partial u}{\partial r} \tag{4.14}$$

$$-\frac{1}{\rho}\frac{\partial p}{\partial r} + \nu \frac{\partial}{\partial r}\frac{1}{r}\frac{\partial}{\partial r} rv = 0 \tag{4.15}$$

$$\frac{\partial u}{\partial x} + \frac{1}{r}\frac{\partial}{\partial r} rv = 0 \tag{4.16}$$

Substituting the boundary conditions for a no-slip nozzle results in Equation 4.17, a series expansion for the axial velocity profile $u(x, r)$ at the outlet of a nozzle of length L as a function of r and x.

$$\frac{u(r,x)}{U_b} = 2(1 - \frac{r^2}{R^2}) + \sum_{n=1}^{\infty} a_n e^{(-\lambda_n \frac{x}{R})} \left(\frac{J_0(k_n \frac{r}{R})}{J_0(k_n)} - 1 \right) \tag{4.17}$$

Here, $J_0(k_n \frac{r}{R})$ and $J_0(k_n)$ are Bessel functions of the first kind of order 0. λ_n represents the equation's eigenvalues, defined by:

$$\lambda_n = \frac{\sqrt{\left(\frac{1}{2}Re\right)^2 + 4k_n^2} - \frac{1}{2}Re}{2} \tag{4.18}$$

a_n are arbitrary constants determined from the inlet condition and k_n is the n-th root of the equation $J_2(k_n) = 0$, which are described in more detail in ref. [19].

Figure 4.2 shows the velocity profiles u/U_b at the nozzle outlet, for a number of nozzle lengths, at $Re = 100$. For most nozzles, the development length $L_{dev} > L$, causing incomplete flow development, which shows in the plug-like radial velocity profiles.

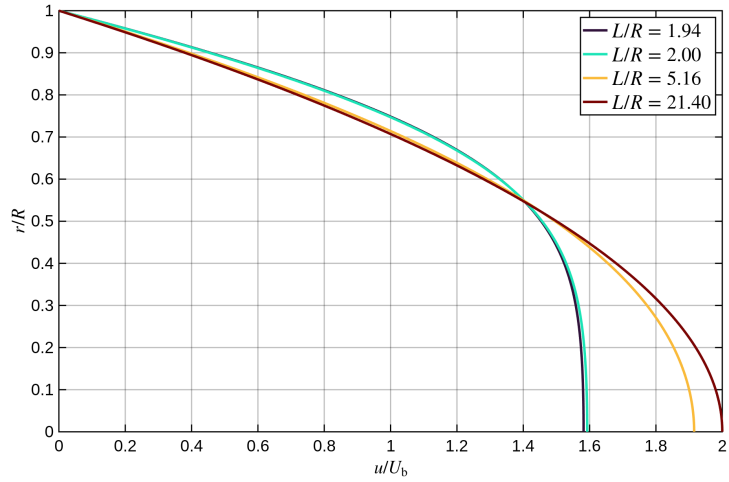


Figure 4.2: Normalized, developing radial velocity profiles at the nozzle outlet for $Re = 100$, showing the undeveloped plug-like profile for short nozzles.

4.2.2. Analytical jet ratio

For $We \gg 1$ and $Re \geq 10$ [3], the capillary term in the denominator of Equation 4.13 vanishes. The viscous term $\frac{3\tilde{K}}{4Re}$ is approximated by:

$$\frac{3\tilde{K}}{4Re} \approx -1.48(Re)^{-\frac{2}{3}} \qquad [3] \tag{4.19}$$

After the necessary substitutions into Equation 4.13, the equation for the jet contraction ratio then becomes:

$$\chi = \frac{\frac{1}{2}\sqrt{3}}{\sqrt{1 + \frac{3}{4}\beta_{outlet} - 1.48(Re)^{-\frac{2}{3}}}} \tag{4.20}$$

Here, β_{outlet} represents the outlet development parameter. Evaluating this term using the velocity profile from Equation 4.17 at the nozzle exit, leads to the following approximation:

$$\beta_{outlet} \approx -\sum_{n=1}^{\infty} \frac{4}{k_n^2} e^{\left(-\lambda_n \frac{L}{R}\right)} \left(2 - e^{\left(-\lambda_n \frac{L}{R}\right)}\right) \tag{4.21}$$

, where λ_n are the function's eigenvalues, as defined in Equation 4.18. Substituting Eq. 4.21 in Eq. 4.13, the approximated equation for the jet ratio χ as a function of L/R and Re becomes:

$$\chi \approx \frac{\frac{1}{2}\sqrt{3}}{\sqrt{1 - \sum_{n=1}^{\infty} \frac{3}{k_n^2} e^{\left(-\lambda_n \frac{L}{R}\right)} \left(2 - e^{\left(-\lambda_n \frac{L}{R}\right)}\right) - 1.48(Re)^{-\frac{2}{3}}}} (Ca >> 1, Re \geq 10) \tag{4.22}$$

Figure 4.3 shows the calculated development of the final jet ratio χ by Equation 4.22. The dotted curves show the experimental results by Gavis and Modan [8]. The calculated final jet ratio shows similar behaviour to the experimental data in the intermediate Reynolds number range, but for $Re < 10$, the curve starts to differ from the experimental data. This is due to the approximation for the viscous forces in Eq. 4.22. Moreover, the entry flow approximation used in deriving the series expansion (Eq. 4.21) is only valid for $20 < Re < 400$.

The critical Reynolds number is defined as the Reynolds number, where χ switches from > 1 to < 1. Both the experimental and analytical curves collapse on a single curve in the intermediate Re-regime, suggesting that the critical Reynolds number is independent of the nozzle length-radius ratio L/R.

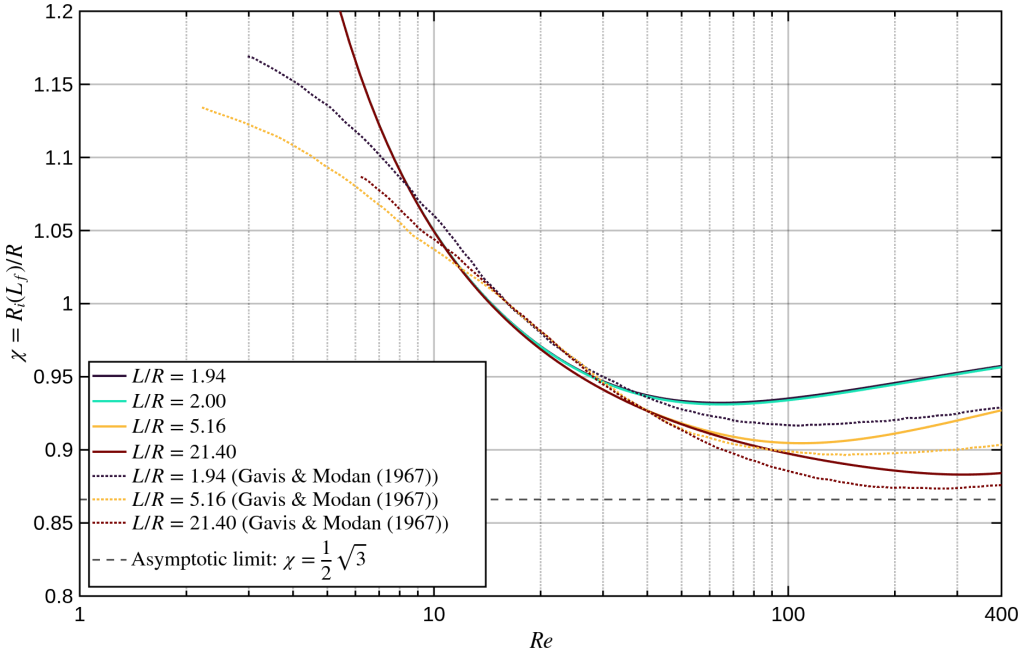


Figure 4.3: Theoretical final jet ratio (solid lines) calculated from Eq. 4.22 compared to the experimental results by Gavis and Modan [8] (dashed lines).

4.3. Flow regimes

4.3.1. Degree of development

β_{outlet} in Eq. 4.11 represents the degree of development or outlet development parameter with respect to a fully developed, homogeneous Poiseuille pipe flow, calculated at the nozzle outlet position:

$$\beta_{outlet} = \frac{\dot{M}^{EN}_{outlet}}{\rho\pi R^2 U_b^2} - \frac{4}{3} \tag{4.23}$$

and is bounded between 0 and $-\frac{1}{3}$.

For a homogeneous, fully developed Poiseuille velocity profile at the nozzle exit, for $L \gg L_{dev}$, or equivalently $L \to \infty$, $\dot{M}^{EN}_{outlet} = \frac{4}{3}\rho\pi R^2 U_b^2$ and $\beta_{outlet} = 0$.

On the other side of the spectrum, as $L \to 0$, the profile upon exiting the nozzle will approach a plug flow: $\dot{M}^{EN}_{outlet} = \rho\pi R^2 U_b^2$ and $\beta_{outlet} = -\frac{1}{3}$. Therefore, the relation for β_{outlet} suggests that an under-developed velocity profile reduces the contraction associated with a fully developed velocity profile. In the experimental results by Gavis and Modan [8]; their Fig. 1 shows a lower contraction ratio χ when ejected from a short nozzle at finite Re, corresponding to an undeveloped flow.

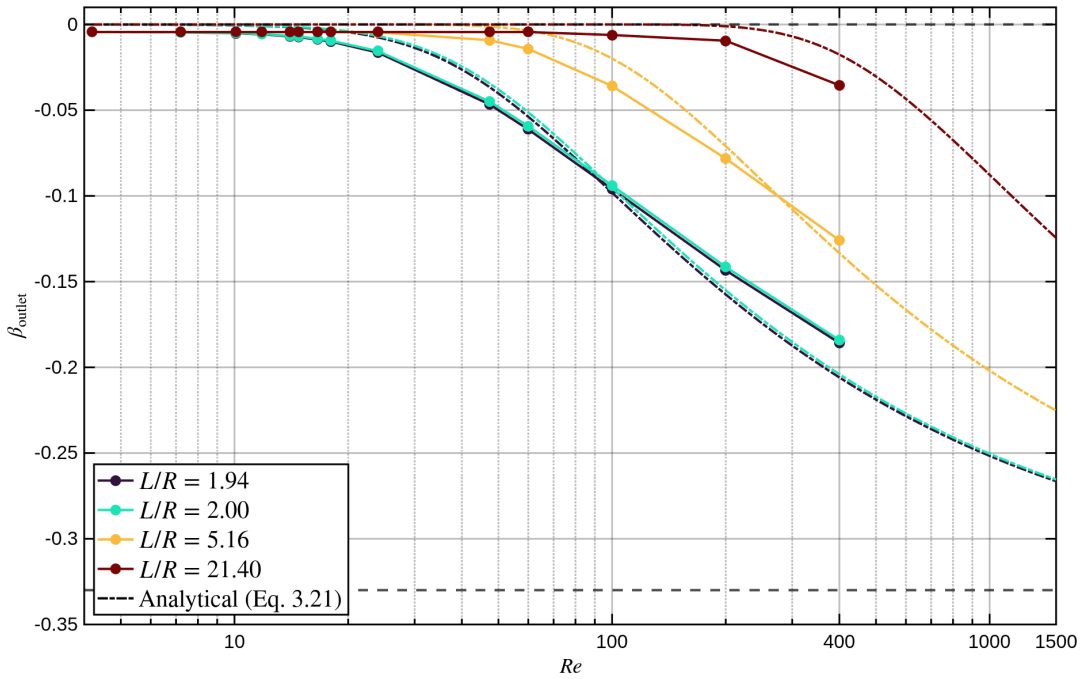


Figure 4.4: Outlet development parameter β_{outlet} as a function of Reynolds number for four different geometries. In the viscous regime, the numerical calculation of β_{outlet} is not exactly 0, but approaches it as close as $\mathcal{O}(0.001)$, most likely due to the numerical resolution used. The dashed lines represent the analytical approximation for β_{outlet}, Eq. 4.21, demonstrating that $\lim_{Re\to 0} \beta_{outlet} = 0$ and $\lim_{Re\to\infty} \beta_{outlet} = -\frac{1}{3}$.

Figure 4.4 shows the outlet development parameter as a function of Reynolds number and nozzle length. For the hydrodynamically developed flows, β_{outlet} is close to zero. As the flow becomes more undeveloped, the curves for β_{outlet} start to decrease within the investigated Reynolds number range and tend to go to $-\frac{1}{3}$ as Re is increased sufficiently.

The Reynolds number at which β_{outlet} starts to decrease is dependent on the nozzle length and corresponds to the critical Reynolds number where the flow within this nozzle length becomes undeveloped. For $L/R = 1.94$ and 2.00, this is approximately between $Re \approx 10 - 12$, for $L/R = 5.16$ it appears to be $Re \approx 47$ and for $L/R = 21.4$ it appears to be $Re \approx 100$.

In general, the shorter the nozzle, the lower β_{outlet} and thus the lowest degree of development at the nozzle outlet position.

4.3.2. Viscous effects

The viscous term $\tilde{K}$ is defined according to:

$$\begin{aligned} \tilde{K} &= \tilde{P}_{exc} + \tilde{T}_{exc} \\ \tilde{P}_{exc} &= 2\left[\tilde{p}_{inlet} - \left(\tilde{p}_{atm} + \frac{\tilde{\kappa}_0}{Ca}\right) - \Delta\tilde{p}^{EN}\right] \\ \tilde{T}_{exc} &= 4\int_{-\tilde{L}}^{0}\left(\tilde{\tau}_{xr|\tilde{r}=1} - \tilde{\tau}^{EN}_{xr|\tilde{r}=1}\right)d\tilde{x} \end{aligned} \tag{4.24}$$

, where $\tilde{P}_{exc}$ is the dimensionless excess wall pressure drop and $\tilde{T}_{exc}$ the dimensionless excess integral wall shear stress, both with respect to a homogeneous Poiseuille flow. [3]

The viscous stresses are most dominant at low Re and will tend to expand the jet. This is observed numerically ([3], [13]) as well as experimentally [8]. In highly viscous regimes, $Re << 1$ and $Ca >> 1$, the integral momentum balance requires $\tilde{K} = 0$ for equilibrium. The pressure gradient will balance the wall shear stress. To satisfy the $\tilde{K} = 0$, a positive curvature is required, i.e. an expansion.

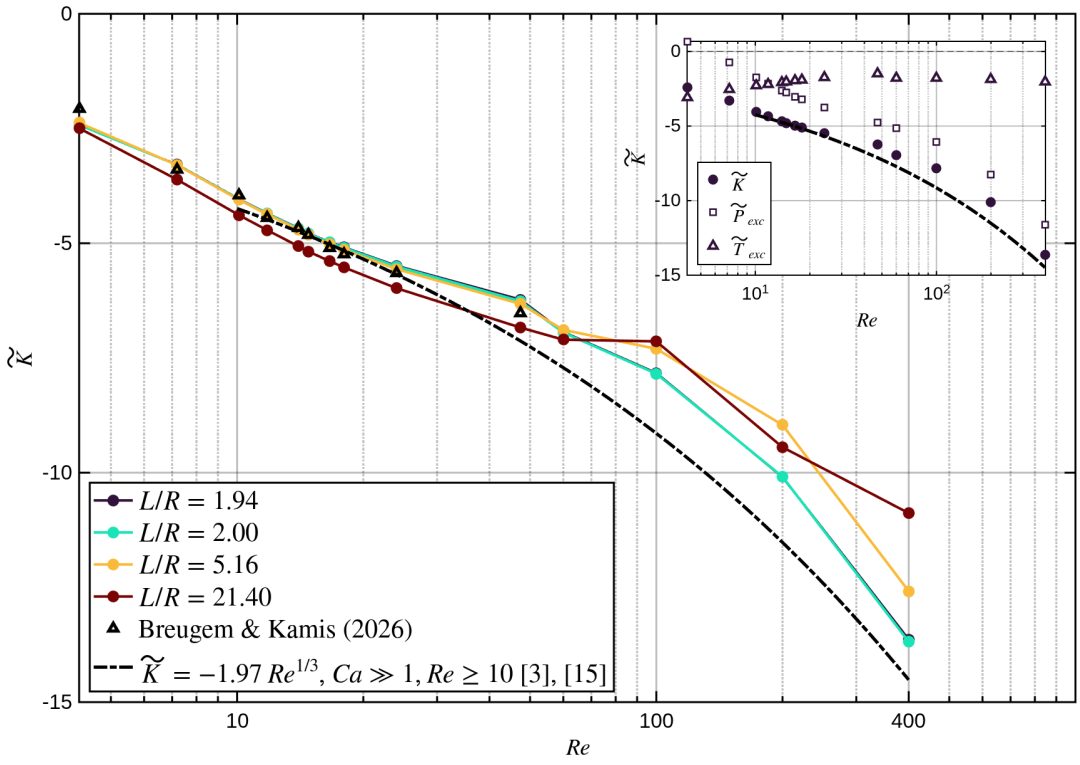


Figure 4.5: Dimensionless perturbed viscous stress term $\tilde{K}$. The dashed line shows an empirical correlation by Joseph [15], valid for $Ca >> 1$, $Re \geq 10$. The triangles represent the derivation by Breugem and Kamis [3] for a fully developed flow for $Re \leq 47.4$. The inset on the top right shows $\tilde{K}$ decomposed into the excess pressure drop $\tilde{P}_{exc}$ and the excess wall shear stress $\tilde{T}_{exc}$, for $L/R = 1.94$.

Figure 4.5 shows the dimensionless viscous force term $\tilde{K}$ for the four different nozzle lengths as a function of Re, constructed from Eq. 4.11 using numerical CFD data. In the intermediate Reynolds number regime, Joseph [15]'s correlation for $Ca \to \infty$ shows good agreement with the numerical data. The black triangles represent numerical results by Breugem and Kamis [3] for a fully developed flow for $Re \leq 47.4$.

As Re increases, $\tilde{K}$ becomes more negative. Moreover, $\tilde{K}$ seems to be relatively unaffected by the nozzle length in the viscous regime, where the curves for $\tilde{K}$ follow the trend of the results by Breugem and Kamis [3] for a fully developed flow. The opposite holds for the inertial regime, which is in line with the decreasing trend of β_{outlet} for the shortest nozzles in Fig. 4.4; as soon as the flow approaches the

critical Reynolds number, the numerical results for $\tilde{K}$ suggest that flow development starts to come into effect.

The change in gradient of $\tilde{K}$ between $Re = 60$ and $Re = 100$ for $L/R = 5.16$ and $L/R = 21.4$ suggests an interaction between viscous nozzle outflow effects and the hydrodynamic development of the upstream flow.

The inset on the top right shows the contribution from the excess pressure drop $\tilde{P}_{exc}$ and the excess wall shear stress $\tilde{T}_{exc}$ for $L/R = 1.94$. At $Re = 4.2$, the excess pressure drop is negative, whereas it is positive for all other Reynolds numbers. The results show that for $Re \leq 6$, axial viscous stresses cause an increased pressure drop within the nozzle, whereas the opposite holds for $Re \geq 6$, as previously reported by Breugem and Kamis [3]. This is the case for all nozzle lengths investigated; although the absolute values are slightly different, the monotonic decrease in excess pressure drop and increase in wall shear stress are visible.

4.3.3. Distinction between viscous outflow effects and flow development

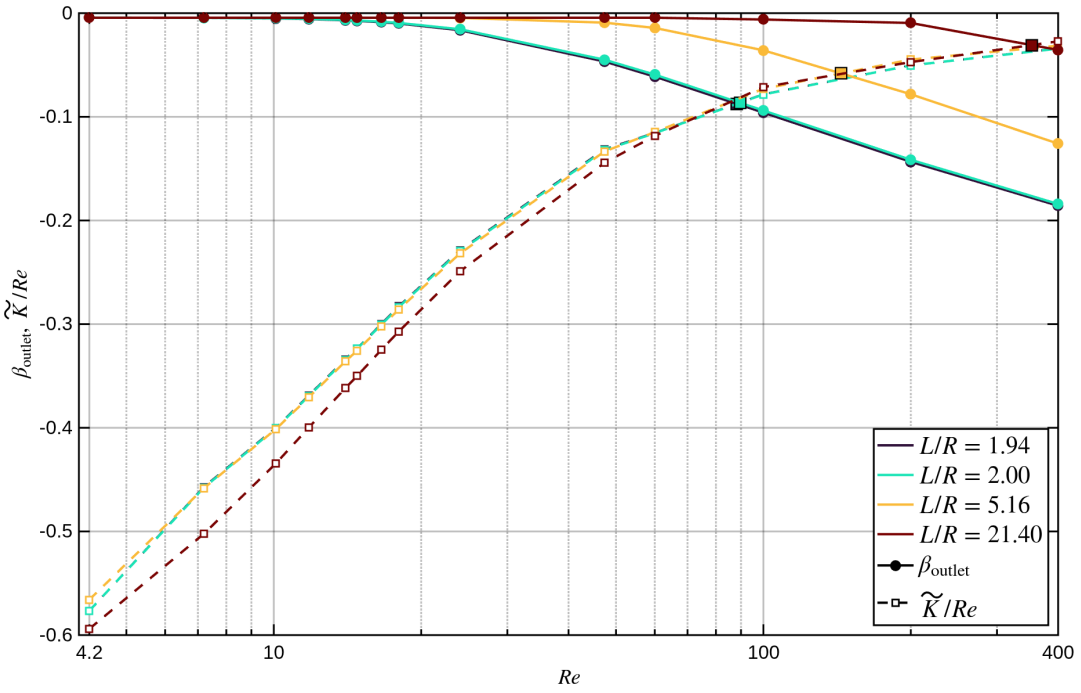


Figure 4.6: Contributions of β_{outlet} (closed dots - solid lines) and $\tilde{K}/Re$ (open squares - dashed lines) to the integral momentum balance, showing the crossover regions between flow development and viscous outflow effects. The crossover Reynolds numbers are shown as the closed squares.

Figure 4.6 compares the magnitudes of β_{outlet} and $\tilde{K}/Re$. At low Reynolds numbers, the contribution of the viscous outflow effects dominate over the flow development effects, whereas at high Reynolds numbers, the opposite holds. Here, the outlet velocity profile becomes increasingly underdeveloped.

The Reynolds number at which flow development becomes dominant is dependent on the nozzle length, in line with the relation between hydrodynamic development and Reynolds number. However, this point is not exactly equal to the Reynolds number at which the flow first becomes underdeveloped; rather, it is the point at which the contribution of flow development effects to the integral momentum balance becomes larger than the viscous contribution. For $L = 1.94R$ and $2.00R$ it is approximately $Re \approx 85$, for $L = 5.16R$ around $Re \approx 150$ and for the longest nozzle investigated, around $Re \approx 350$. The crossover Reynolds numbers are marked with closed squares in Figure 4.6.

4.3.4. Capillary effects

Surface tension dominates the integral momentum balance in Eq. 4.11 for $We << 1$ and $Ca << 1$. In the derivation of the integral momentum balance for a fully developed flow by Breugem and Kamis [3] it was found that the inertial and viscous terms drop out and the equation for χ is only a function of the surface curvature and jet angle at the nozzle outlet:

$$\chi = \cos\varphi + \tilde{R_i}"(0)\cos^3\varphi \tag{4.25}$$

In the limiting case of infinitely high surface tension, since $cos(\varphi) = 1$ and $\tilde{R_i}"(0) = 0$ must hold at the nozzle exit, Equation 4.25 will reduce to $\chi = 1$. In other words, the jet will become a constant radius cylinder at very high surface tension. In general, surface tension acts counteractive to any changes in the jet radius [3]. In their derivation of the integral momentum balance for a fully developed flow, it was found that surface tension has a stiffening effect at $Re = 4.2$, reducing the expansion of the jet, but becomes negligible as the Reynolds number is increased beyond this value under the conditions investigated.

However, the influence of surface tension does not only depend on the Reynolds number, but also on the Weber number. Consequently, capillary effects may remain relevant at higher Reynolds numbers when the Weber number is sufficiently low. The influence of the Weber number on the reconstructed and numerically obtained jet ratios is therefore investigated in more detail in 7.2.3, particularly in relation to the differences between numerical and experimental results.

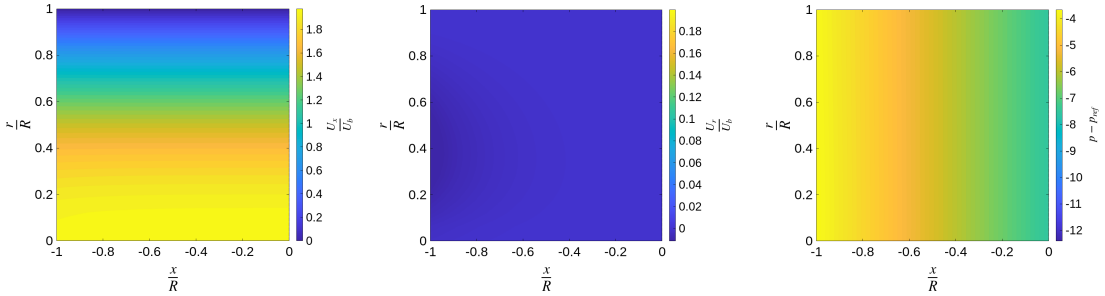
5. Two-dimensional flow fields

In the following chapter, the numerical two-dimensional flow fields (velocity, pressure and velocity magnitude) are presented, with the aim to quantify the outflow effects in the nozzle exit region. Similar to the decomposition of the integral momentum balance in Chapter 4, the two-dimensional flow fields are also decomposed: subtracting the undisturbed pipe flow from the perturbed jet flow results in the perturbation flow fields.

5.1. Flow field decompositions

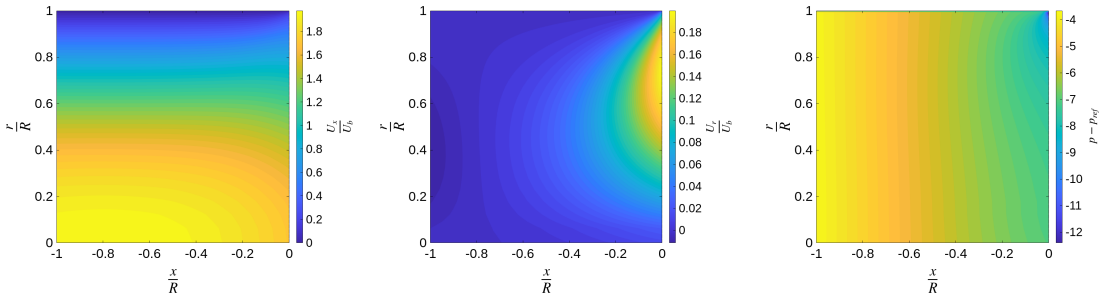
For a viscous-dominated regime, $Re = 4.2$, and for the inertia-dominated regime, $Re = 400$, the two-dimensional flow fields are shown for the undisturbed long pipe flow and jet flow, inside the exit region ($-1 < x < 0$) of the shortest nozzle investigated of length $L = 1.94R$, in Figures 5.1 to 5.6. The pressure fields are presented relative to the pressure in the free-slip inlet zone (p_{ref}).

5.1.1. Viscous regime: $Re = 4.2$



(a) Axial velocity field. **(b)** Radial velocity field. **(c)** Pressure field.

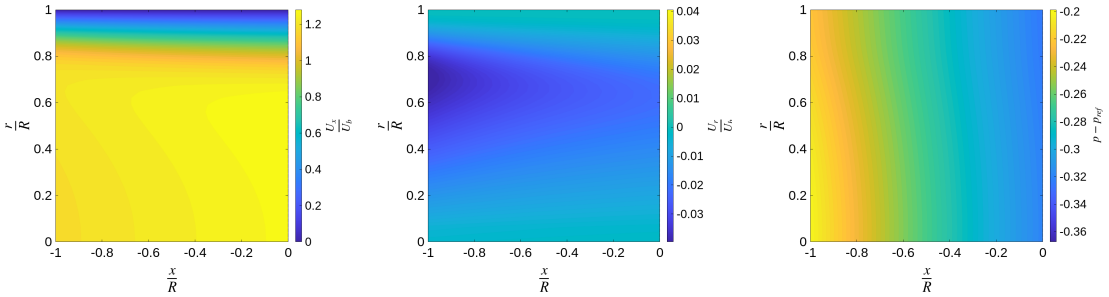
Figure 5.1: Two-dimensional flow fields: undisturbed pipe flow for $L/R = 1.94$, $Re = 4.2$.



(a) Axial velocity field. **(b)** Radial velocity field. **(c)** Pressure field.

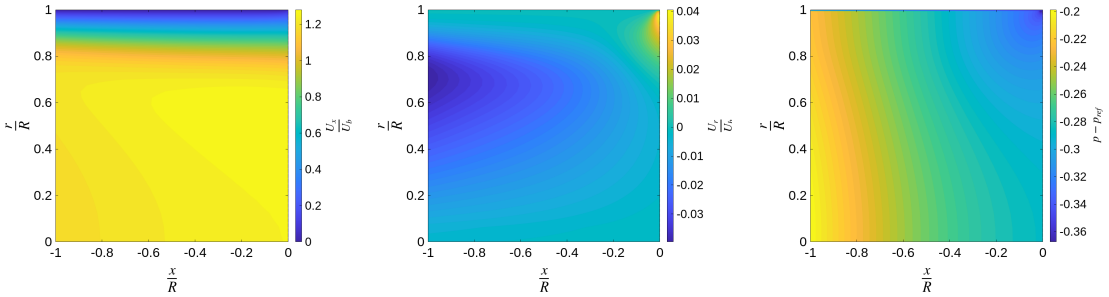
Figure 5.2: Two-dimensional flow fields: jet flow for $L/R = 1.94$, $Re = 4.2$.

5.1.2. Inertial regime: $Re = 400$



(a) Axial velocity field. **(b)** Radial velocity field. **(c)** Pressure field.

Figure 5.3: Two-dimensional flow fields: undisturbed pipe flow for $L/R = 1.94$, $Re = 400$.

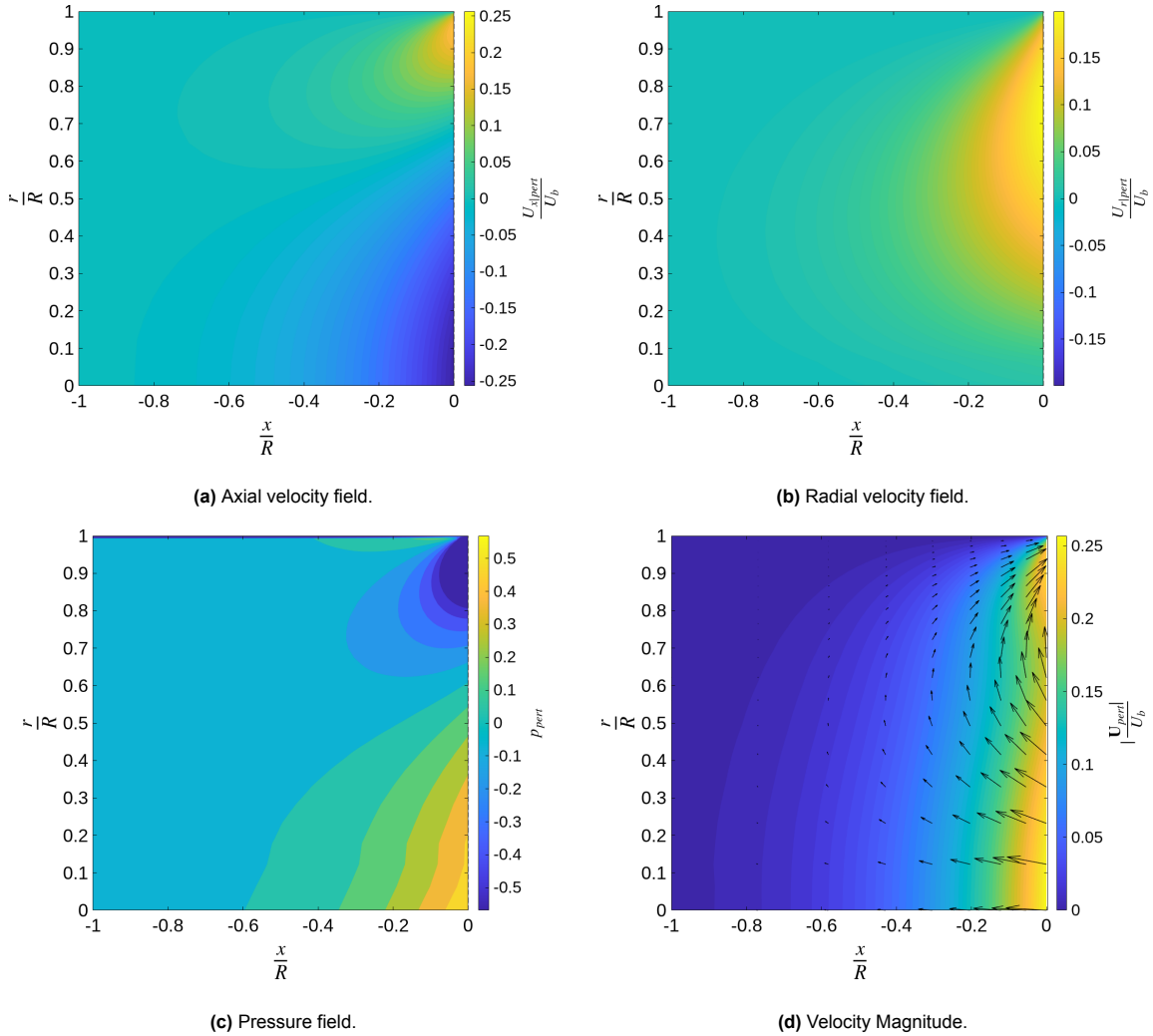


(a) Axial velocity field. **(b)** Radial velocity field. **(c)** Pressure field.

Figure 5.4: Two-dimensional flow fields: jet flow for $L/R = 1.94$, $Re = 400$.

5.1.3. Perturbation fields

Subtracting the undisturbed long pipe flow fields from the jet flow fields results in the perturbation fields for axial and radial velocity, pressure and velocity magnitude.



(a) Axial velocity field.

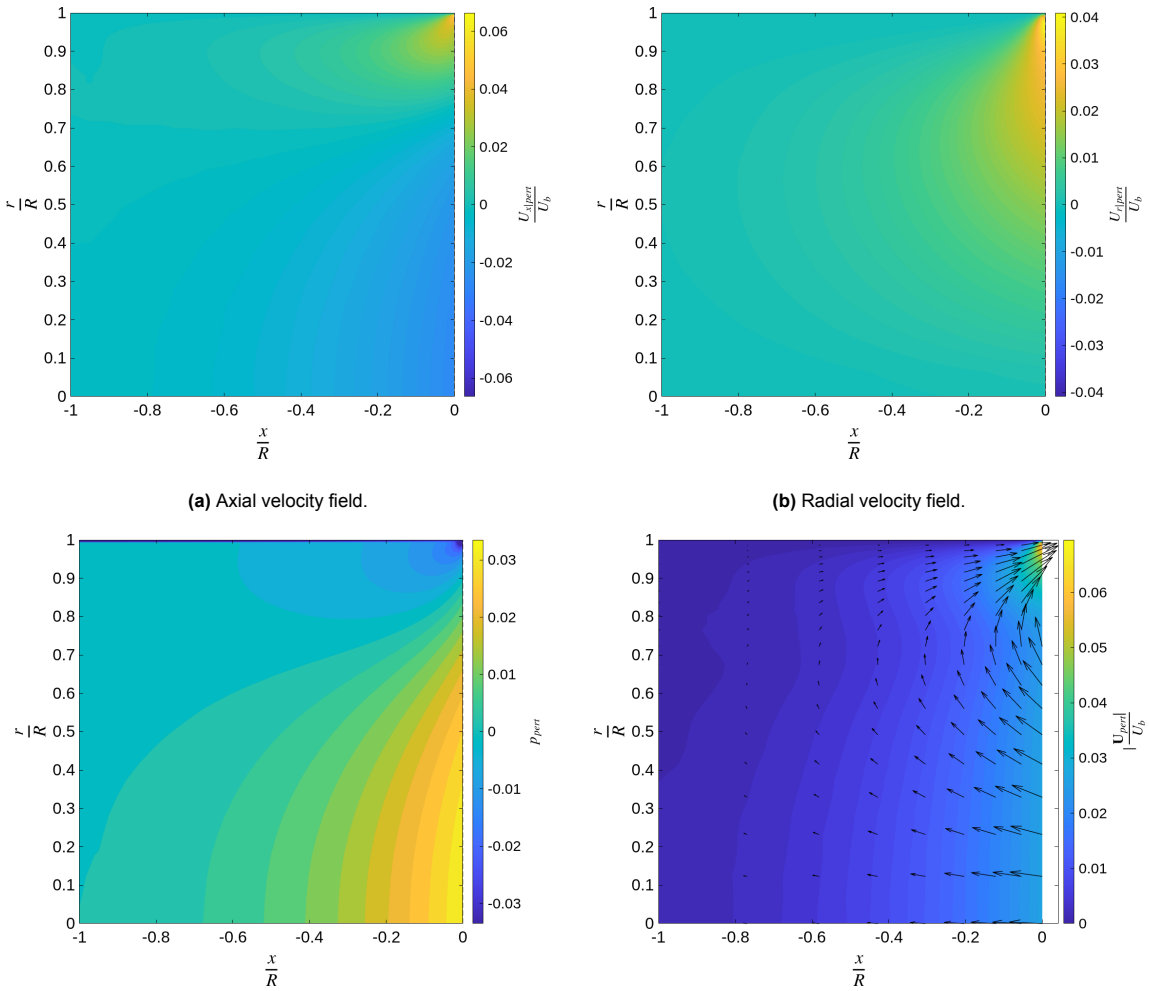
(b) Radial velocity field.

(c) Pressure field.

(d) Velocity Magnitude.

Figure 5.5: Two-dimensional flow fields: perturbation field for $L/R = 1.94$, $Re = 4.2$.

The perturbation field for $Re = 4.2$ (Fig. 5.5) shows a radial velocity gradient developing near the nozzle outlet wall lip. Also, there exists a gradient in the axial direction towards the core of the jet. As the axial velocity near the nozzle lip increases due to the transition from no-slip at the nozzle wall to free-slip at the jet surface, the radial velocity increases at the nozzle exit plane. Mass conservation across the nozzle exit plane dictates this. [3] As a consequence, the jet expands downstream of the nozzle exit.



(a) Axial velocity field.

(b) Radial velocity field.

(c) Pressure field.

(d) Velocity magnitude of the perturbation velocity field.

Figure 5.6: Two-dimensional flow fields: perturbation field for $L/R = 1.94$, $Re = 400$.

In the inertia-dominated regime, $Re = 400$, similar behaviour is visible as in the viscous-driven flows at low Reynolds numbers (Fig. 5.6), where a radial velocity is increased near the nozzle exit plane. However, the perturbations are decreased in magnitude and are less concentrated across the nozzle exit lip; as a consequence of the more advection-driven flow, they are more downstream spread out, corresponding to a contracting jet. [3]

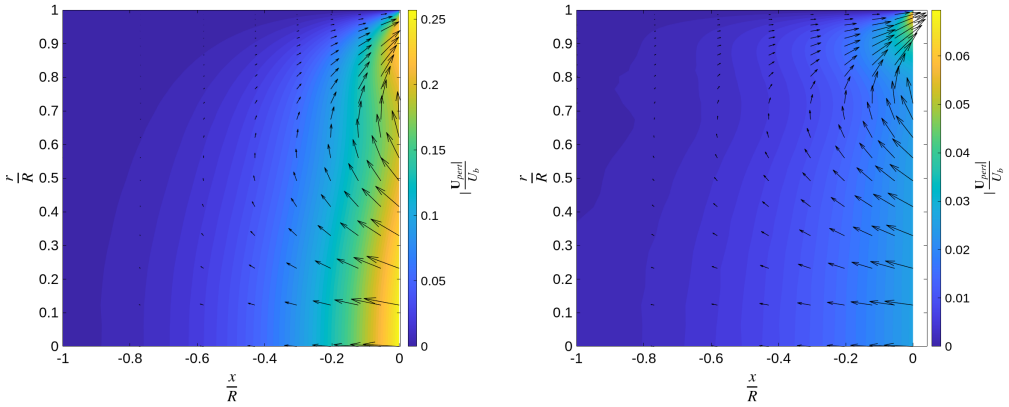
5.2. Effect of the nozzle length on the perturbation flow fields

Figures 5.7 and 5.8 again show the perturbation fields, but this time for all four nozzle lengths investigated.

Figure 5.7 shows the perturbation velocity magnitudes for $Re = 4.2$ (left) and $Re = 400$ (right) for four different nozzles in increasing length (top to bottom); Figure 5.8 shows the radial velocity fields for the same cases.

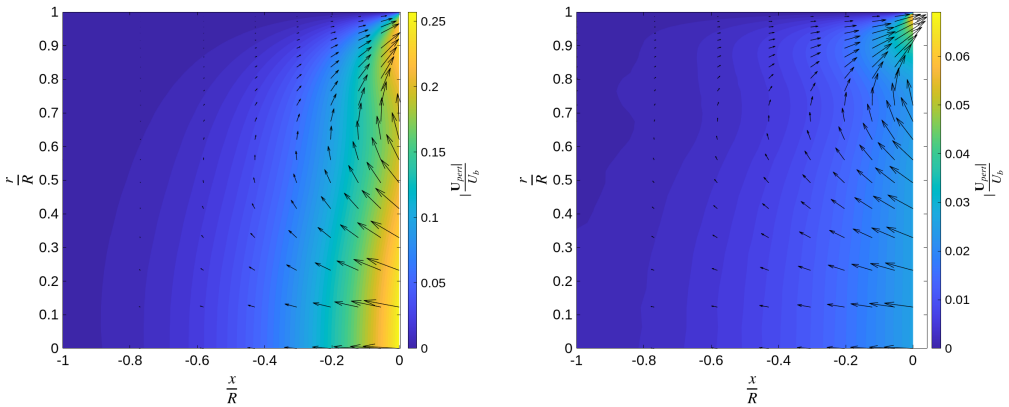
For $Re = 4.2$, the viscous-dominated regime (Figs. 5.7a, 5.7c, 5.7e, 5.7g), the perturbation fields are almost identical: the maximum perturbation magnitude is approximately constant and the spatial distribution changes very little. Similar behaviour can be seen in the radial velocity profiles in Figure 5.8, which is equal for all nozzle lengths. This suggests that, for a sufficiently long nozzle at low Reynolds numbers, the perturbations around the nozzle exit are independent of the degree of flow development, and thus of nozzle length, and only a viscous outflow effect. This can be explained by the relation for the hydrodynamic development length (Eq. 2.3); all nozzles are longer than the required hydrodynamic development length at $Re = 4.2$.

For $Re = 400$, the inertia-dominated regime Figs. (5.7b, 5.7d, 5.7f, 5.7h), the effect of increasing the nozzle length becomes much more noticeable. All but the largest nozzle show very similar, almost negligible, perturbation magnitudes, but the arrows indicating the direction of the flow show otherwise. This is closely related to the higher degree of development in longer nozzle. The flow in the largest nozzle, $L/R = 21.4$, displays a more advection-driven flow due to higher inertia and shows a lower radial velocity gradient in Figure 5.8, as this flow is at a higher development stage compared to the flow in the other three shorter nozzles.



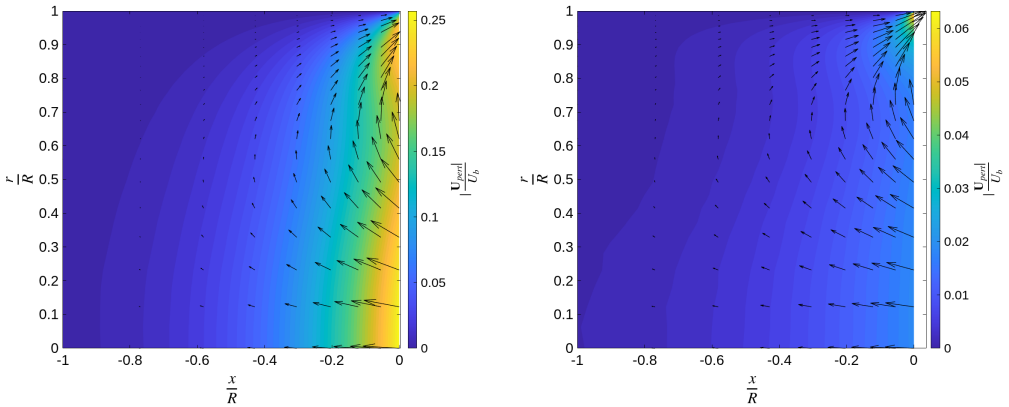
(a) $Re = 4.2$, $L/R = 1.94$.

(b) $Re = 400$, $L/R = 1.94$.



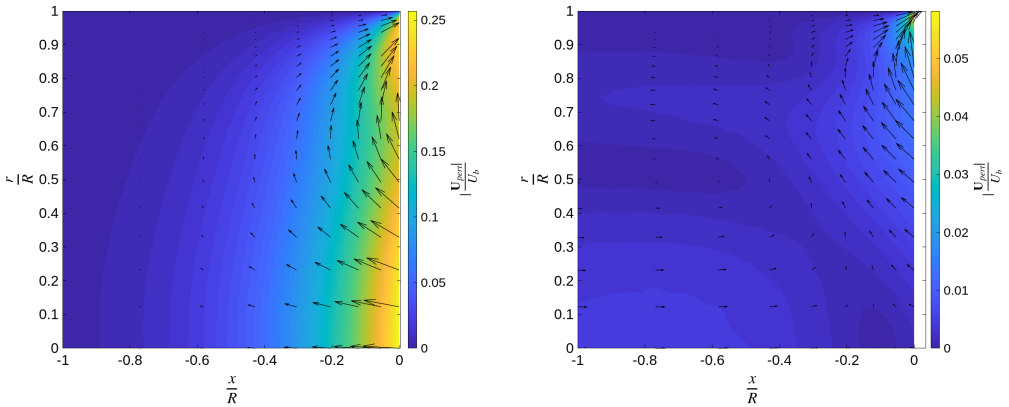
(c) $Re = 4.2$, $L/R = 2.00$.

(d) $Re = 400$, $L/R = 2.00$.



(e) $Re = 4.2$, $L/R = 5.16$.

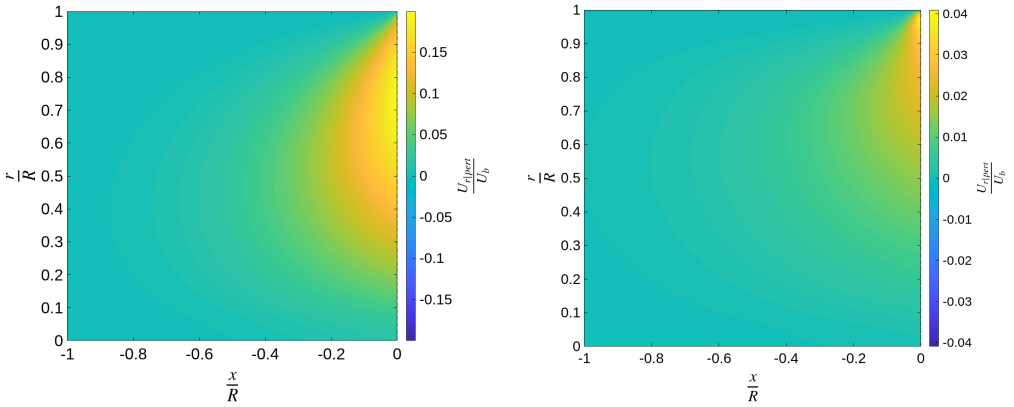
(f) $Re = 400$, $L/R = 5.16$.



(g) $Re = 4.2$, $L/R = 21.4$.

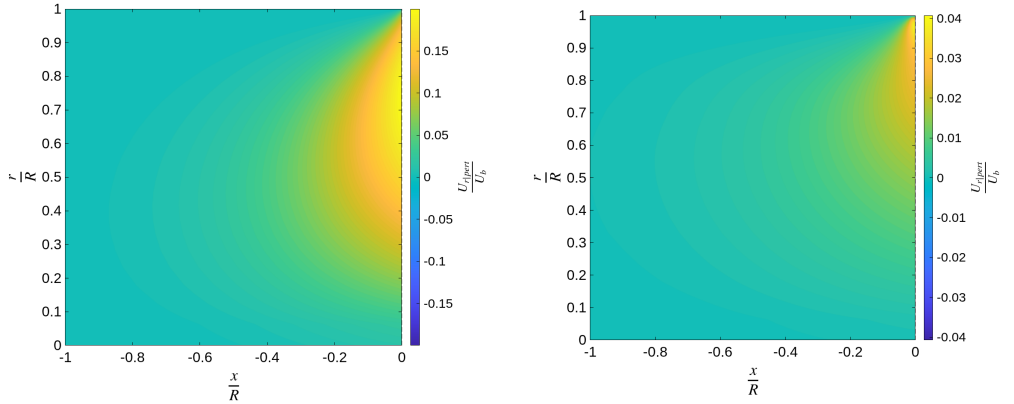
(h) $Re = 400$, $L/R = 21.4$.

Figure 5.7: Velocity magnitude perturbation fields for $Re = 4.2$ (left) and $Re = 400$ (right), illustrating the influence of nozzle length on the exit region perturbations. From top to bottom, $L/R = 1.94$, 2.00, 5.16, and 21.4.



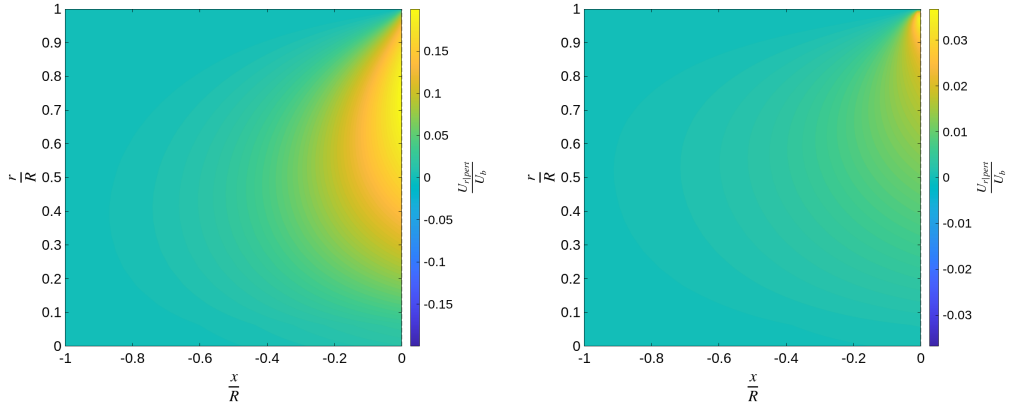
(a) $Re = 4.2$, $L/R = 1.94$.

(b) $Re = 400$, $L/R = 1.94$.



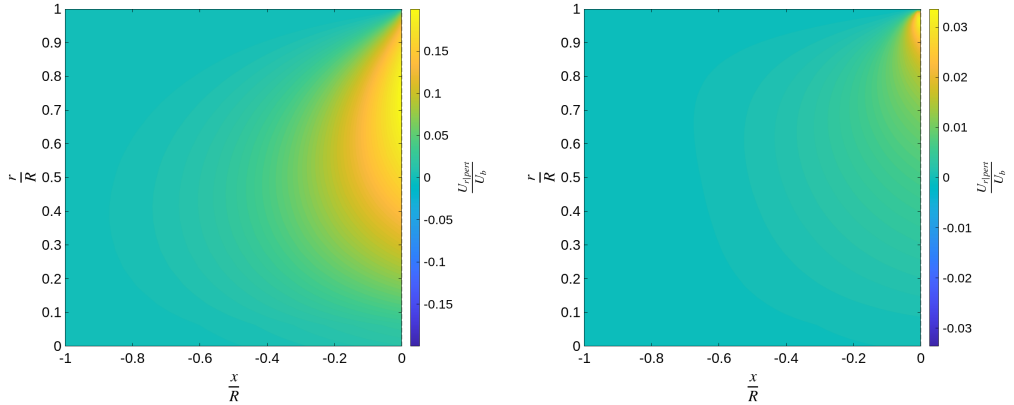
(c) $Re = 4.2$, $L/R = 2.00$.

(d) $Re = 400$, $L/R = 2.00$.



(e) $Re = 4.2$, $L/R = 5.16$.

(f) $Re = 400$, $L/R = 5.16$.



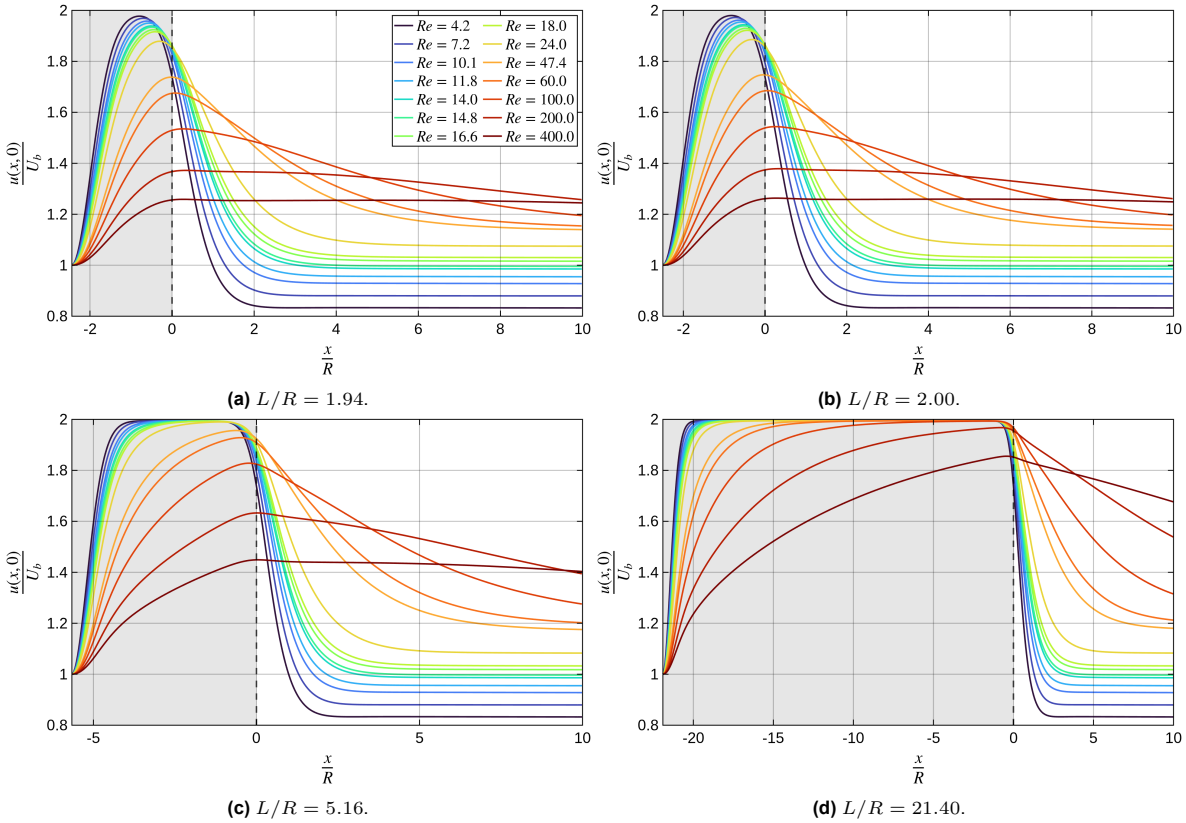
(g) $Re = 4.2$, $L/R = 21.4$.

(h) $Re = 400$, $L/R = 21.4$.

Figure 5.8: Radial velocity perturbation fields for $Re = 4.2$ (left) and $Re = 400$ (right), illustrating the influence of nozzle length on the exit region perturbations. From top to bottom, $L/R = 1.94$, 2.00, 5.16, and 21.4.

6. Centerline velocity

The chapter presents numerical results for the centerline velocity.



(a) $L/R = 1.94$. **(b)** $L/R = 2.00$.

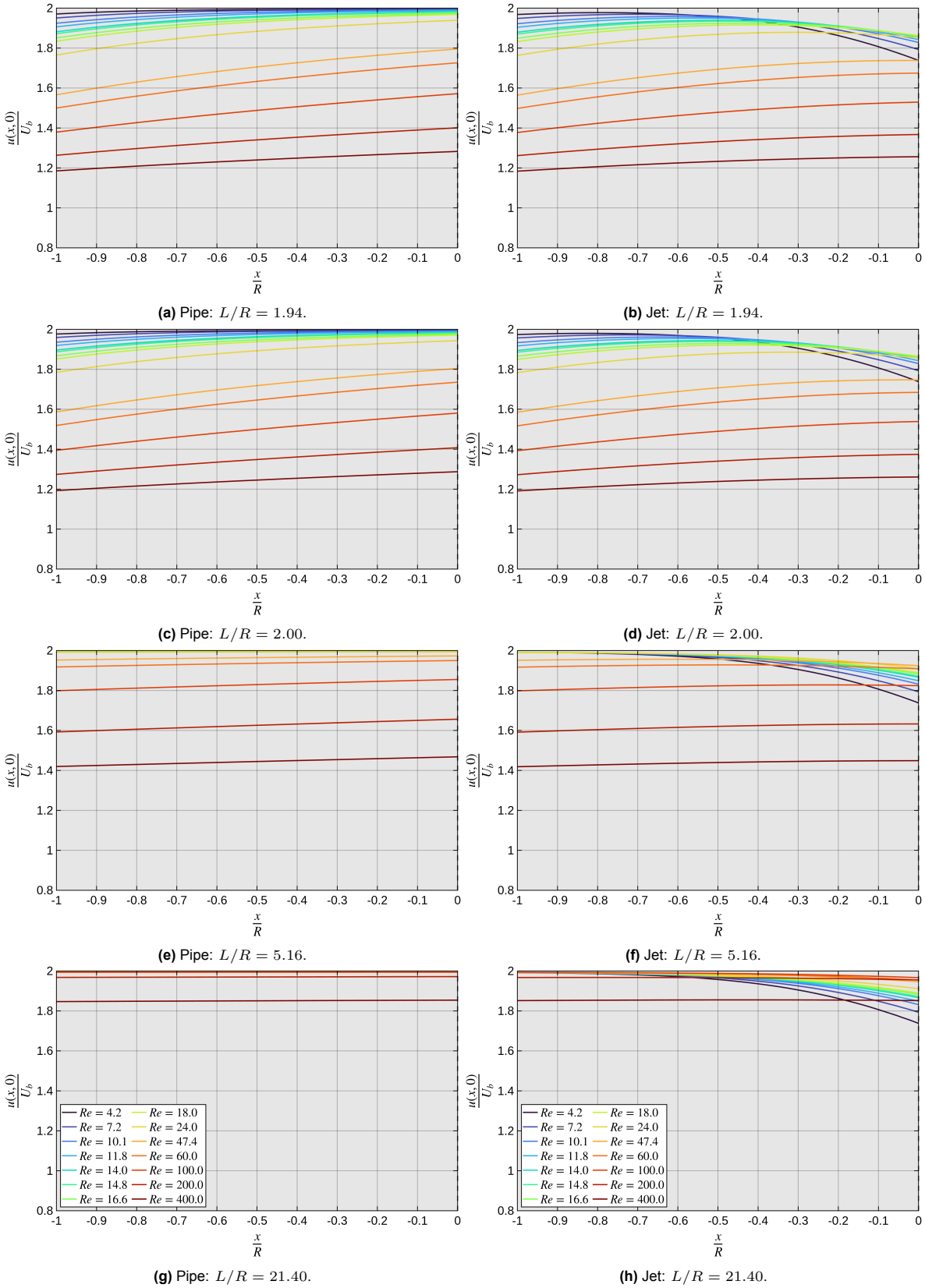
(c) $L/R = 5.16$. **(d)** $L/R = 21.40$.

Figure 6.1: Numerical results for the centerline velocity as a function of Reynolds number and axial coordinate, for four different nozzle lengths. The shaded area represents the nozzle.

In Figs. 6.1a to 6.1d, the centerline velocities for four nozzle lengths are given. The magnitude starts at $1U_b$, which is the prescribed uniform inflow condition at the start of the nozzle. The flow then develops along the nozzle length and should reach $2U_b$ when the flow is fully developed.

At low Reynolds numbers, the flow should be sufficiently developed for most geometries. However, the maximum is reached slightly upstream of the nozzle exit, followed by a decline in magnitude, due to the effect of the stick-slip transition on the upstream flow. This transition generates axial viscous stresses, responsible for a compressive normal viscous stress at the jet interface, causing the surface to be pushed outwards and causing an expanding jet. [3]

For high Reynolds numbers and short nozzles, the upstream nozzle flow might be undeveloped and the magnitude of the centerline velocity is far below the fully developed value of $2U_b$. Moreover, the decline in centerline velocity as the fluid leaves the nozzle is much lower. This suggests inertia is dominating over viscous effects, which are responsible for the fast decline at lower Reynolds numbers and causing a contracting jet downstream of the nozzle outlet.



(a) Pipe: $L/R = 1.94$.

(b) Jet: $L/R = 1.94$.

(c) Pipe: $L/R = 2.00$.

(d) Jet: $L/R = 2.00$.

(e) Pipe: $L/R = 5.16$.

(f) Jet: $L/R = 5.16$.

(g) Pipe: $L/R = 21.40$.

(h) Jet: $L/R = 21.40$.

Figure 6.2: Numerical results for the centerline velocity inside the exit region for four different geometries. The left figures show the undisturbed long pipe flow, the right figures show the jet flow, demonstrating the difference in centerline velocity as a consequence of flow undevelopment and exit perturbations. The shaded area represents the nozzle region.

Figure 6.2 shows the numerical results for the centerline velocity inside the exit region. The left plots show the centerline velocity developing in the undisturbed long pipe flow and the right plots demonstrate the effects of developing flow and viscous exit perturbations in the jet simulations. The results for the pipe flow demonstrates the process of a developing velocity profile, since there are no exit-induced perturbations here. The shorter the nozzle, generally the more undeveloped the flow is. See also Figure 4.4 in Section 4.3.1. The highest Reynolds numbers in particular are far from the fully developed magnitude of $2U_b$ and show an equally undeveloped profile in both the jet and pipe plots.

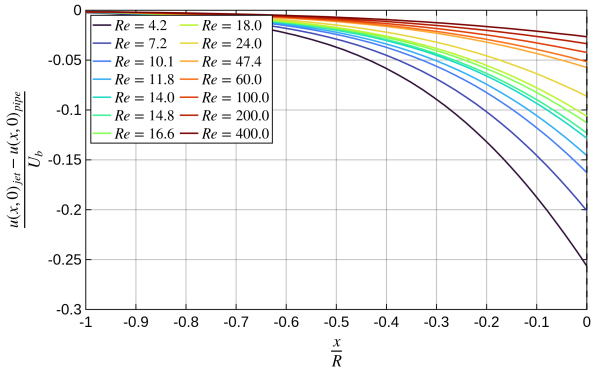
In the jet, the flow is affected by a combination of development effects and viscous exit perturbations. The low Reynolds numbers, some of which should be developed, particularly for the largest nozzle of $L/R = 21.4$, reach their peak magnitude some distance upstream of the exit, after which they start to decline. The fact that the profiles look equal for all four nozzle lengths and that only the low Reynolds numbers show this fast decline, suggests this is a consequence of viscous exit perturbations, dominant at low Reynolds numbers and independent on the nozzle length in this regime, as previously reported in Section 4.3.2. The higher Reynolds numbers, corresponding to an undeveloped flow within the nozzles investigated, do not show this decline and appear unaffected by the outflow perturbations. This behaviour is confirmed by the two-dimensional radial velocity perturbation plots in Figure 5.8; the radial velocity gradient at $Re = 400$ is more concentrated close to the nozzle outlet lip and jet surface and is zero close to the core of the flow. This reduces the fast decline in centerline velocity.

Figure 6.3a presents the perturbation centerline velocity relative to the uniform inflow velocity U_b for the shortest nozzle of length $L = 1.94R$, where development effects should generally be the most dominant. Noticeable are the largest perturbations for the lowest Reynolds numbers. The five highest Reynolds numbers, $Re \geq 47.4$, show considerably lower perturbations within this geometry, again suggesting the decline of viscous exit perturbations and inertial flow development effects taking over.

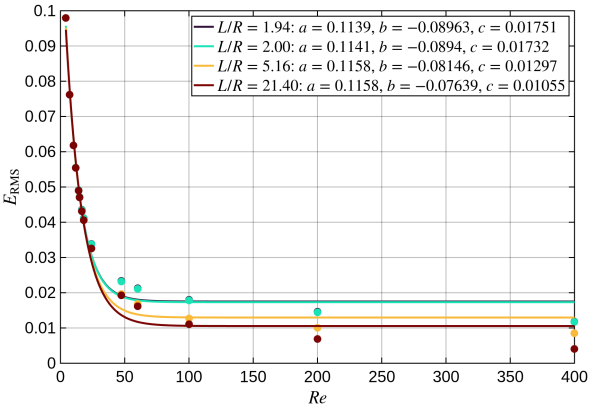
As the flow gets nearer to the nozzle exit plane, the perturbation velocity becomes more negative nonlinearly, indicating more perturbation as a consequence of the nozzle outflow. To quantify these perturbations in the exit region on both the Reynolds number and the nozzle length, the RMS-magnitude of the perturbation centerline velocity in the exit region, calculated by:

$$E_{RMS} = \sqrt{\int_{-1}^{0} \left[\Delta\tilde{u}(\tilde{x}, 0)\right]^2 d\tilde{x}} \approx ae^{bRe} + c \tag{6.1}$$

, is shown in Figure 6.3b. a represents the exponential amplitude, b the decay coefficient and c the asymptotic offset. At low Re, viscous-driven flows, the RMS-magnitudes are strongest. The curves collapse as $Re \to 0$, again suggesting independence of the nozzle length here and suggesting the viscous exit perturbations are dominant in this regime. As the Reynolds number increases, the RMS-value curves start to deviate around $Re \approx 50$ and the effect of the flow development starts to show. The shortest nozzle, corresponding to the most undeveloped flow, shows the largest RMS-values.



(a) Numerical perturbation centerline velocity for $L/R = 1.94$, relative to the uniform inflow velocity U_b, showing the nonlinear increase of centerline perturbations near the nozzle exit plane.



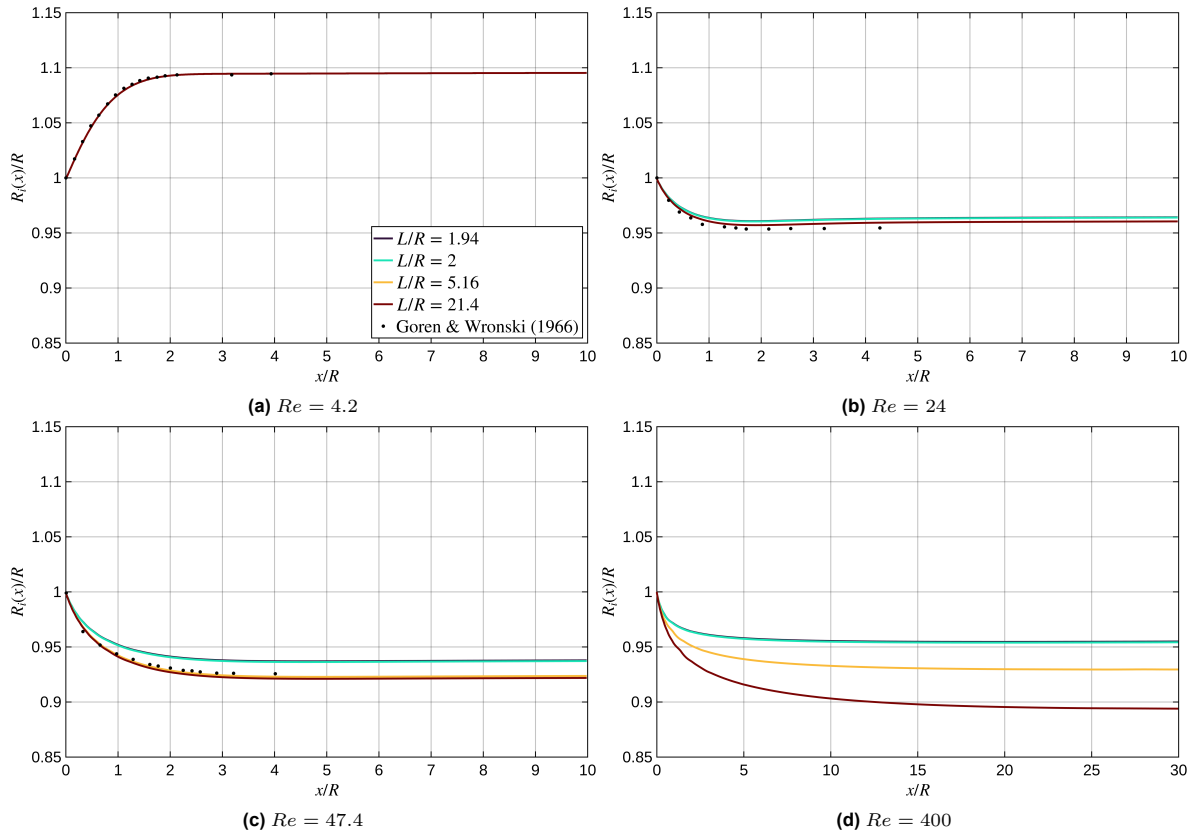
(b) Exponential fit to the perturbed centerline magnitude RMS.

Figure 6.3: Numerical results for the perturbation centerline velocity and the exponential decay of centerline perturbations.

7. Jet profile

The following chapter discusses the numerical results for the jet surface, downstream of the nozzle exit. This includes the downstream surface profiles, final jet expansion or contraction ratio as a function of Reynolds number and the surface curvature and interface angle at the nozzle outlet.

7.1. Numerical surface results



(a) $Re = 4.2$ **(b)** $Re = 24$

(c) $Re = 47.4$ **(d)** $Re = 400$

Figure 7.1: Jet surface profiles as a function of x/R downstream of the nozzle outlet and of nozzle length L/R. The dots represent experimental data by Goren and Wronski [10] for a fully developed flow at $Re = 4.2$, 24 and 47.4.

Figure 7.1 shows a selection of numerical jet surface profiles as a function of downstream distance from the nozzle outlet, for four different Reynolds numbers. Expansion occurs for the viscous-dominated low Reynolds number jets, contraction occurs for the inertia-driven high Reynolds number jets and as the Reynolds number is increased further, the influence of undeveloped nozzle flow becomes increasingly more important.

For $Re = 4.2$ up to $Re = 18$, the jet radius appears largely independent of nozzle length. The downstream jet formation is predominantly governed by the upstream exit perturbations of the flow.

$Re = 24$ is the first Reynolds number where different surface profiles are observed for an increasing nozzle length. The nozzles of length $5.16R$ and $21.4R$ show an equal result for the surface profile, since their outlet velocity profiles are approximately fully developed. However, the two shortest nozzles of length $1.94R$ and $2.00R$ show less contraction than their longer counterparts. Following the relationship for the hydrodynamic development length Eq. 2.3, both of these nozzles have an undeveloped velocity profile at the nozzle outlet.

Interestingly, $Re = 24$ is not the first Reynolds number at which the flow becomes undeveloped within this geometry ($1.94R$), which is $Re = 11.8$. For $Re \leq 24$, the difference in surface profiles between different nozzle lengths is negligible, see Appendix B. This is supported by the absolute magnitudes of the degree of development term β_{outlet} and $\tilde{K}/Re$ from the integral momentum balance, Equation 4.11 and Figure 4.6. Here, β_{outlet} is closer to zero than $\tilde{K}/Re$, indeed suggesting negligible effects of undeveloped flow at this Reynolds number.

At $Re = 47.4$, the results for $L/R = 5.16$ and $L/R = 21.4$ show practically equal values. They also show good agreement with the experimental data by Goren and Wronski [10]. However, the two shorter nozzles show less contraction for this Reynolds number, which is consistent with the undeveloped upstream velocity profiles within these nozzles. At this Reynolds number, β_{outlet} in Figure 4.6 shows almost equal values for $L = 5.16R$ and $21.4R$, but for $L = 1.94R$ and $L = 2.00R$ β_{outlet} is much more negative.

At $Re = 400$, the effect of undeveloped nozzle flow appears the most pronounced; the difference between the largest and the shortest nozzle is $\approx 6\%$. Within the nozzle lengths investigated, the jet (contraction) ratio shows a large dependency on nozzle length, because the upstream velocity profile has not reached the fully developed state at the nozzle exit. The nozzle with length $21.4R$ has the most developed flow, however, resulting in the most contraction. Also note the downstream distance required for the jet to attain a constant radius is much larger as the Reynolds number increases.

The higher contraction ratios for shorter nozzles in Figure 7.1 validates the relation between upstream flow development and the downstream formation of a jet. The integral momentum balance decomposition, derived in Chapter 4, predicts a value of $-\frac{1}{3} \leq \beta_{outlet} \leq 0$, implying reduced jet contraction as a consequence of undeveloped flow. The numerical jet interface profiles confirm this.

7.2. Final jet ratio

7.2.1. Direct numerical results

Figure 7.2 shows the numerical results for the final jet ratio as a function of Reynolds number for four different nozzle lengths, together with the experimental data by Gavis and Modan [8]. Final jet ratio here, is defined as the value of χ at a position x/R, downstream of the nozzle exit, where the surface gradient dR_i/dx approaches zero over an interval $1R$ up- and downstream of this position.

Overall, the numerical results show similar trends to the experimental data, apart from deviating absolute magnitudes in the viscous-dominated as well as the inertia-dominated regimes.

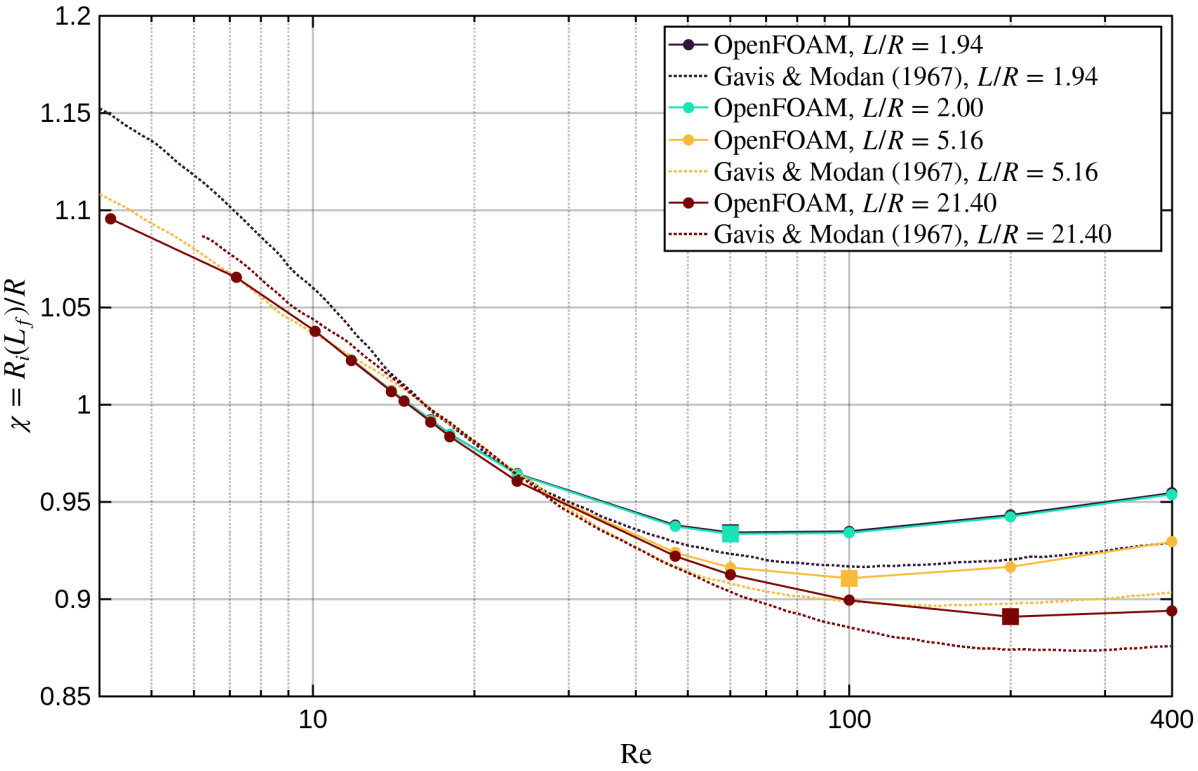


Figure 7.2: Numerical final jet ratio as a function of Reynolds number Re, compared to the experimental results by Gavis and Modan [8] (dashed lines). The squares mark the minimum final jet ratio measured for the different geometries with respect to Reynolds number.

In the numerical results, all four curves collapse on a single curve for $Re \leq 24$, which is consistent with the decomposition of the integral momentum balance, showing negligible influence of undeveloped flow at low Reynolds numbers. However, the experimental data shows different expansion ratios in this regime. In the original data, Figure 1 in ref. [8], the curves in the viscous regime show a lot of scatter and different fluid viscosities. The authors Gavis and Modan mention in their article the possibility the temperature at which the experiments were run had an influence on the results. Since both the numerical results for the jet ratio as well as the integral momentum balance decomposition show, that, for the investigated nozzle lengths, L/R has little to no effect in this low-Re regime, this could possibly be the best explanation for the deviation from the experimental results at low Reynolds numbers.

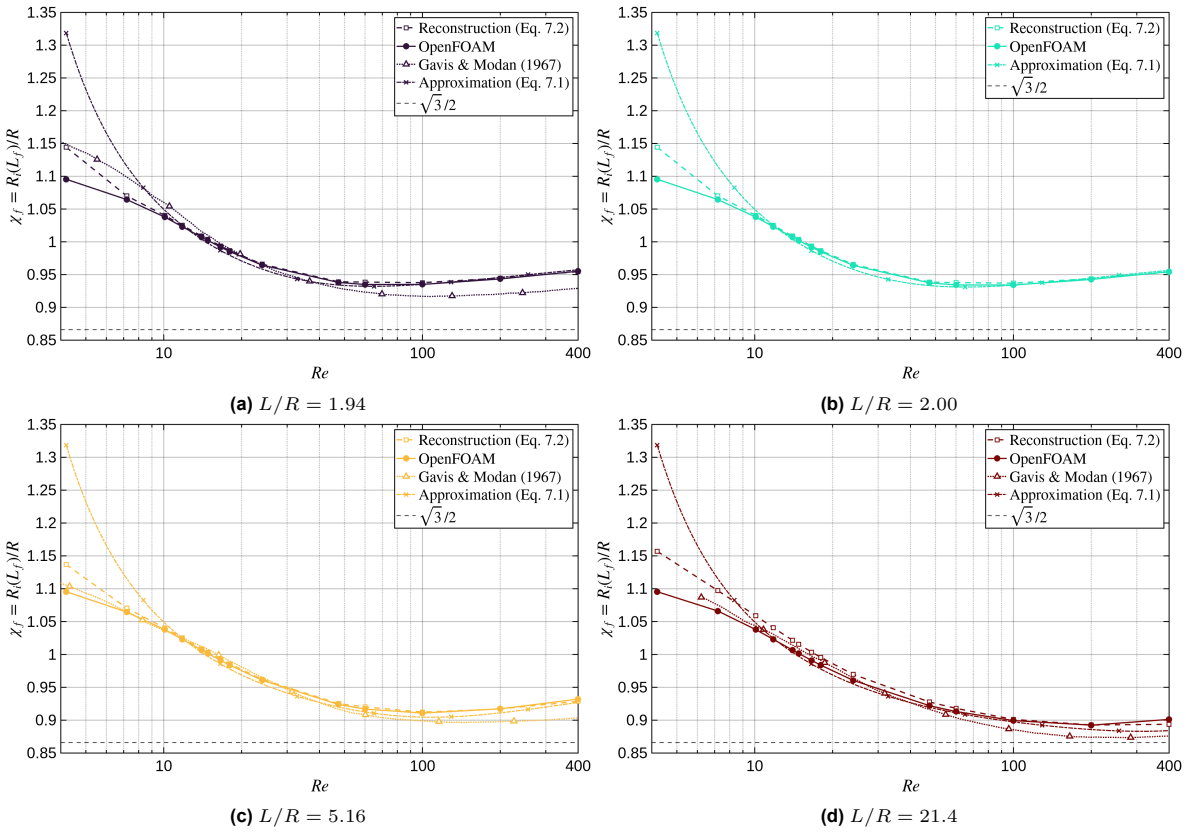
At high Reynolds numbers, the contracting-jet regime, the numerical results for all four nozzle lengths show higher contraction ratios compared to the experimental results. A possible explanation for this, is the finite, constant Weber number used throughout the simulations. As a result, the effect of surface tension might be overpronounced, since the derivation of the integral momentum balance has shown that capillary effects stiffen the jet interface, resulting in, in this case, less contraction.

7.2.2. Reconstruction

The jet ratio χ is reconstructed directly from the two-dimensional flow fields using the integral momentum balance and compared to the direct CFD data, as well as the experimental data by Gavis and Modan. Moreover, the approximation for χ, valid for negligible surface tension using the correlation derived by Joseph [15] and the series expansion for the radial velocity profile by Lew [19] is given. The results are shown in Figure 7.3 for the four investigated nozzle lengths. The two derived equations for the jet ratio χ are given once more below.

$$\chi\left(Re, \frac{L}{R}\right) \approx \frac{\frac{1}{2}\sqrt{3}}{\sqrt{1 - \sum_{n=1}^{\infty} \frac{3}{k_n^2} e^{\left(-\lambda_n \frac{L}{R}\right)} \left(2 - e^{\left(-\lambda_n \frac{L}{R}\right)}\right) - 1.48(Re)^{-\frac{2}{3}}}}, (Ca >> 1, Re \geq 10) \tag{7.1}$$

$$\chi\left(Re, \frac{L}{R}\right) = \frac{\frac{1}{2}\sqrt{3}}{\sqrt{1 + \frac{3}{4}\beta_{outlet} + \frac{3}{4}\frac{\tilde{K}}{Re} + \frac{3}{4We}\left[\chi - cos(\varphi) - \tilde{R_i}"(0)cos^3(\varphi)\right]}} \tag{7.2}$$



(a) $L/R = 1.94$ **(b)** $L/R = 2.00$

(c) $L/R = 5.16$ **(d)** $L/R = 21.4$

Figure 7.3: Jet ratios: reconstructed (open squares), direct CFD Data (closed circles) and experiments by Gavis and Modan [8] (dashed lines).

Figure 7.3 shows the results for the final jet ratio, obtained from: (1) a reconstruction using Eq. 7.2, (2) direct measurements of the numerical CFD data and (3) the approximation for $Ca \to \infty$, $Re \geq 10$, Eq. 7.1.

At lower Reynolds numbers, the approximation based on Joseph [15]'s correlation predicts much stronger expansion ratios in the far viscous regime. This is to be expected, regarding the validity of the correlation. The reconstruction shows the diverging geometries at the larger Reynolds numbers and overlaps with the direct CFD measurements almost perfectly for the two shortest nozzles, which indicates that the integral momentum balance captures the effect of a longer nozzle correctly. However, as the nozzle length increases, the contraction ratios at the largest Reynolds numbers start to deviate.

7.2.3. Sensitivity to the Weber number

At higher Reynolds numbers, corresponding to a contracting jet, the numerical simulations generally predict larger final contraction ratios than the experimentally measured values by Gavis and Modan [8]. A possible explanation for this is the constant Weber number of $We = 14.29$ employed throughout the original simulations. Since the Weber number characterizes the relative importance of inertial and surface-tension forces, the chosen value may have resulted in stronger capillary effects than those in the experimental conditions.

The decomposition of the integral momentum balance provides a way to investigate this hypothesis. The relative magnitudes of the outlet development parameter β_{outlet} and the dimensionless viscous forces $\tilde{K}/Re$ in Section 4.3.3 reveal that the viscous contribution dominates at low Reynolds numbers, whereas the contribution due to flow development becomes more important as the Reynolds number increases. Nevertheless, the capillary contribution remains noticeable, particularly at intermediate and high Reynolds numbers, as presented in Figure 7.4. For simplicity's sake, the capillary term, 3rd term on the right-hand side of the implicit equation for the jet ratio χ, Eq. 4.11, is written as C_σ.

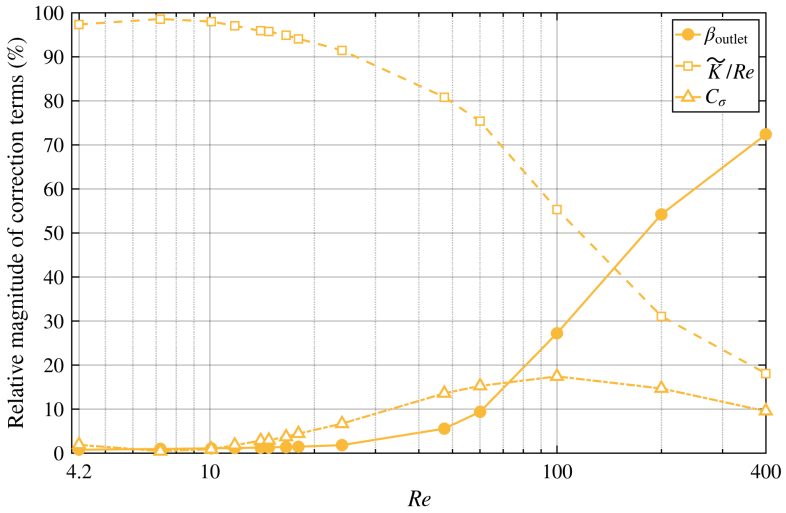


Figure 7.4: Relative magnitudes of the three correction terms in the integral momentum balance for $L/R = 5.16$: the outlet flow development contribution β_{outlet}, the viscous correction $\tilde{K}/Re$, and the capillary contribution C_σ. Each contribution is normalized by the sum of the absolute magnitudes of all three terms. The percentages therefore indicate their relative importance without accounting for cancellation between terms of opposite sign.

For $L/R = 5.16$, the capillary contribution accounts for approximately 10-20% of the combined absolute magnitudes over the contracting-jet regime. Although the percentage does not directly represent the influence of surface tension on the contraction ratio, it gives an indication that the explicit capillary term cannot necessarily be neglected. Furthermore, the surface tension also appears in the pressure contribution to $\tilde{K}/Re$. As a consequence, the total explicit dependence of the integral momentum balance on the Weber number is not represented by the separate capillary term on its own.

To investigate the deviations from the experimental results, the Weber numbers corresponding to the selected experimental conditions were estimated using the surface-tension parameter $S = \frac{\rho\sigma R\chi}{\mu^2}$ [10]. Combining this equation with the Reynolds and Weber number definitions gives:

$$We = \frac{\frac{1}{4}Re^2}{S/\chi} \tag{7.3}$$

A value of the surface tension parameter $S = 0.3$ was chosen as a reference from the experiments by Goren and Wronski [10]. Since Gavis and Modan [8] did not report the Weber numbers corresponding to their individual experiments, their experimental contraction ratios were used to estimate the Weber numbers by using Eq. 7.3. The resulting estimates for $L/R = 5.16$ are presented in Table 7.1.

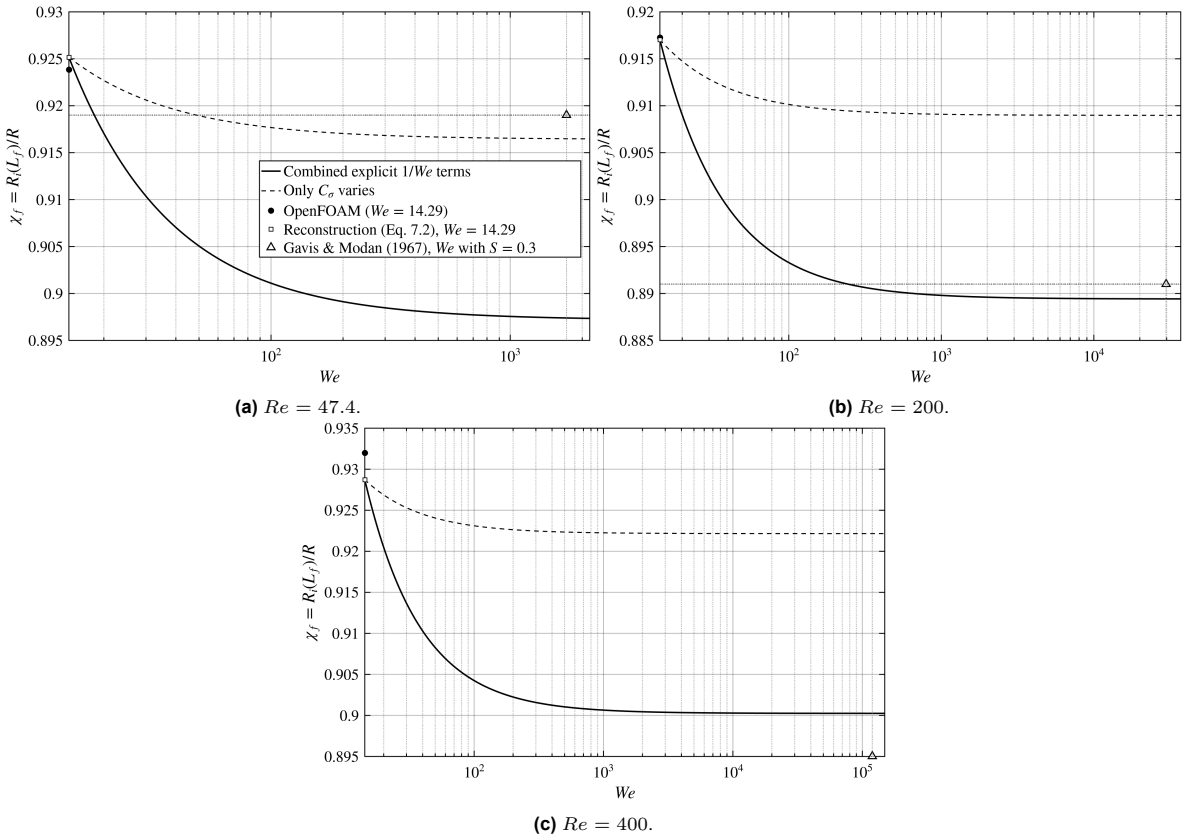
Re	Estimated We	Experimental χ
47.4	10^3	0.919
200	$10^4 - 10^5$	0.891
400	10^5	0.895

Table 7.1: Estimated Weber numbers based on the contraction ratios measured by Gavis and Modan [8] for $L/R \approx 5.16$, assuming the surface-tension parameter $S = 0.3$ from Goren and Wronski [10].

The estimated Weber numbers are substantially larger than the constant value used in the original simulations. This difference becomes particularly noticeable at higher Reynolds numbers, where the estimated Weber numbers exceed the numerical value by a great amount. It should be clarified that these are estimated Weber numbers; the assumption of a constant $S = 0.3$ is based on the experiments by Goren and Wronski [10] and cannot necessarily be applied to all viscosities investigated by Gavis and Modan [8].

To quantify the possible influence of the prescribed surface tension, a parametric sensitivity analysis was performed using the integral momentum balance reconstruction for $Re = 47.4$, $Re = 200$ and $Re = 400$, with $L/R = 5.16$. In this analysis, the explicit Weber number dependence of the reconstruction equation was varied while retaining the same velocity field, pressure distribution, viscous contributions and interface geometry, as obtained from the original numerical simulations at $We = 14.29$. Two approaches were considered. In the first, only the separate capillary contribution was varied with the Weber number. In the second, both the separate capillary contribution and the capillary pressure contribution to $\tilde{K}/Re$ were included.

Figure 7.5 presents the resulting contraction ratios as a function of Weber number, compared with the original numerical contraction ratios as well as the experimental values of Gavis and Modan [8].



(a) $Re = 47.4$.

(b) $Re = 200$.

(c) $Re = 400$.

Figure 7.5: Final contraction ratio as a function of increasing the Weber number in the integral momentum balance reconstruction, for $Re = 47.4$, $Re = 200$ and $Re = 400$, compared to the experimental final contraction ratio by Gavis and Modan [8] at an estimated Weber number.

For all three Reynolds numbers, increasing the Weber number results in a smaller reconstructed contraction ratio. The predicted contraction ratios decrease rapidly at relatively low Weber numbers, before reaching an approximately constant value as the Weber number increases further. This behaviour demonstrates that the explicit capillary contribution to the integral momentum balance reconstruction can have a large influence on the predicted contraction ratio, even though the capillary term does not dominate the combined absolute magnitudes.

At $Re = 47.4$, the original numerical contraction ratio is relatively close to the experimental value of 0.91. Increasing the Weber number causes the predicted contraction ratio to decrease. However, when both explicit capillary contributions are included, the reconstructed contraction ratio approaches 0.89, smaller than the experimental value. Therefore, the combined correction overestimates the required increase in contraction under the assumptions of an equal velocity and pressure field and interface geometry. At $Re = 200$, the original numerical value is approximately 0.91, compared with the experimental value of approximately 0.89. Increasing the Weber number to the estimated value decreases the predicted ratio to approximately 0.88, closer to the experimental measurement. At $Re = 400$, a similar trend is visible. The reconstructed value decreases from approximately 0.92 at the original Weber number to approximately 0.900 at the estimated experimental Weber number, approaching the experimental value of 0.89 closely.

To investigate whether the sensitivity predicted by the integral momentum balance is also observable in the numerical simulations, additional OpenFOAM simulations were performed at increased Weber numbers, estimated from the previously assumed value $S = 0.3$. The resulting contraction ratios are compared with those obtained numerically using the original Weber number of $We = 14.29$, as shown in Figure 7.6.

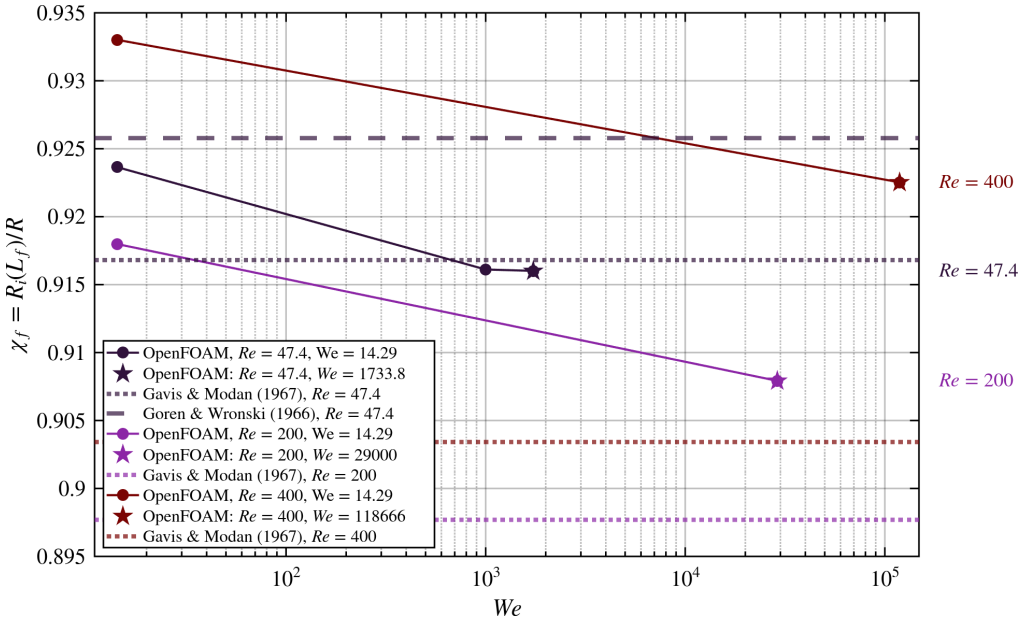


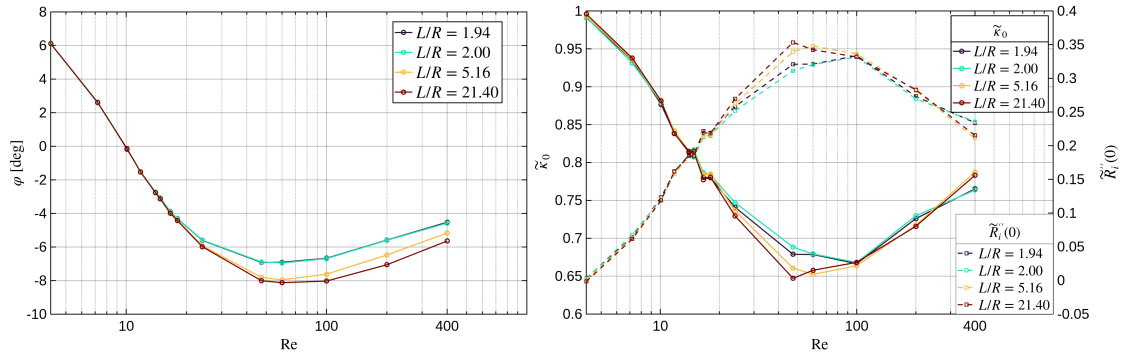
Figure 7.6: Final numerical contraction ratio at increased Weber numbers for $Re = 47.4$, $Re = 200$ and $Re = 400$. The experimental results by Gavis and Modan [8] are given for all three Reynolds numbers, results by Goren and Wronski [10] is only available for $Re = 47.4$. The results demonstrate the effect of increasing the Weber number at the given Reynolds numbers. The line drawn between the points is a visual guideline, it does not represent a linear relationship between χ_f and We. The numerical contraction ratios are evaluated at a fixed downstream position; At $Re = 200$ and $Re = 400$, the jet might not yet have reached its final constant value.

The additional OpenFOAM simulations confirm that increasing the Weber number results in a more contracting jet. At $Re = 47.4$, increasing the Weber number brings the numerical result close to the experimental measurement. Note the difference to the experimental result by Goren and Wronski [10], this is because they assumed a fully developed flow. At $Re = 200$ and $Re = 400$, the increased Weber number leads to similar behaviour. However, an important limitation of this comparison is that the contraction ratios are measured at a fixed downstream position of $10R$. Previous numerical simulations

have shown that the jet requires a greater downstream distance to develop into a constant radius as the Reynolds number increases.

Nevertheless, the additional simulations support the hypothesis that the relatively strong capillary effects at $We = 14.29$ contribute to the difference in jet contraction ratios. The more contracting jets at higher Weber number, observed in Figure 7.6, are consistent with the trend predicted by the integral momentum balance, Figure 7.5. However, the reduction obtained from the additional OpenFOAM simulations is smaller than that predicted by the integral momentum balance sensitivity analysis. It confirms the indirect effect of surface tension on the capillary pressure term within $\tilde{K}$, not just the direct contribution via C_σ. The additional OpenFOAM simulations therefore conclude that the difference between the original numerical and experimental results are influenced by the capillary contribution, although the complete influence on the contraction ratio remains to be investigated, particularly at the other Reynolds numbers originally investigated.

7.3. Jet angle and curvature at the nozzle outlet



(a) Jet angle φ with respect to the nozzle wall plane as a function of Re.

(b) Dimensionless jet curvature $\tilde{\kappa}_0$ and dimensionless 2nd derivative of the radius $\tilde{R}_i"(0)$.

Figure 7.7: Nozzle exit interface geometry as a function of Reynolds number for four nozzle lengths.

By fitting a polynomial to the surface data, the jet angle φ with respect to the nozzle wall plane was determined and is shown in Figure 7.7a. The positive angle for $Re = 4.2$ and $Re = 7.2$ indicates a radially outward flow and thus an expanding jet. For $Re \geq 10$, the angle becomes negative, indicating an initial contraction as the fluid leaves the nozzle, which is visible in the numerical surface profiles for these cases. Interestingly, the graph for the jet angle φ reaches a minimum value at $Re = 47.4$ and then starts to increase with Re as we near the inertia-dominated regime. Longer nozzles exhibit a more negative angle compared to shorter nozzles, which is consistent with their more developed exit velocity profiles and a stronger jet contraction, as seen in Figure 7.2.

The dimensionless interface curvature $\tilde{\kappa}_0$ is shown in Figure 7.7b. Similar to the jet angle φ, it first decreases with increasing Reynolds number, reaches a minimum between 47.4 and 60 and then starts to increase again. As pointed out by Breugem and Kamis [3], the nondimensional curvature $\tilde{\kappa}_0$ is approximately equal to $1 - \tilde{R}_i"(0)$.

8. Conclusion

The influence of the nozzle length on the expansion or contraction behaviour of laminar liquid jets was investigated. The integral momentum balance, derived by Breugem and Kamis [3] for a fully developed nozzle flow, was extended to incorporate the effects of hydrodynamic flow development inside the nozzle. Furthermore, numerical results for laminar liquid jets using the finite-volume CFD solver OpenFOAM version 13 were presented. The Reynolds number range investigated in the experiments by Goren and Wronski [10] for a fully developed flow, $4.2 \leq Re \leq 47.4$ was extended up to $Re = 400$. The influence of a hydrodynamically underdeveloped flow on the downstream jet formation, investigated experimentally by Gavis and Modan [8], was examined numerically for three of their nozzle length-radius ratios: $L/R = 1.94$, $L/R = 5.16$ and $L/R = 21.4$. Next to these, a ratio of $L/R = 2.00$ was investigated, corresponding to a length-diameter ratio of exactly one.

In the derivation of the jet expansion or contraction ratio χ from the integral momentum balance decomposition, the distinction was made between exit perturbations on the velocity profile, represented by the outlet development parameter β_{outlet} and the viscous pressure and shear components, $\tilde{K}$. It was found that β_{outlet} is largely unaffected by the nozzle length at low Reynolds numbers, where the flow inside the nozzle is largely fully developed. As the Reynolds number increases, however, the required hydrodynamic development length increases and the critical Reynolds number where the flow becomes underdeveloped in a finite nozzle length, is reached. As a consequence, β_{outlet} starts to be affected by the degree of development, in other words by the nozzle length.

The dependence for the pressure and shear contributions was observed in a similar manner, where the dimensionless shear stress contribution to the integral momentum balance, $\tilde{K} = \tilde{P}_{exc} + \tilde{T}_{exc}$, seems to be unaffected by the nozzle length at low Reynolds numbers. This relates to the fact that the flow at low Reynolds numbers was developed within the nozzle lengths investigated. The opposite holds for high Reynolds numbers, where $\tilde{K}$ becomes more dependent on the length of the nozzle; it was observed to be more negative for a shorter nozzle, as the flow from a short nozzle and high Reynolds number is undeveloped. This suggests the increased hydrodynamic development length at higher Reynolds numbers also influences the viscous stresses around the nozzle exit, when the Reynolds number is increased sufficiently and the nozzle remains short, relative to the required development length.

The investigation of the perturbations upstream of the nozzle exit was further extended by analyzing the two-dimensional perturbation flow fields inside the exit region, defined as $1R$ upstream of the nozzle outlet plane. The perturbation fields investigated include axial and radial velocity contours, pressure contours and the velocity perturbation magnitude contours. At low Reynolds numbers and for all nozzle lengths investigated, the axial and radial velocity fields show a negligible effect of the nozzle length, indicating upstream exit perturbations are only function of viscous outflow effects, where the flow is approximately developed. At higher Reynolds numbers, upstream exit perturbations are not only a function of viscous outflow effects, but also of the hydrodynamic flow development and with this the nozzle length. Magnitudes of the flow parameters are largely identical here, but as the Reynolds number increases, the increased inertia-driven flow advects the perturbations more downstream. Furthermore, the transition between dominant viscous outflow effects and flow development effects starts between $Re = 60 - 200$, depending on the length of the nozzle.

Besides the upstream flow, the numerical results also show that hydrodynamic development affects the downstream formation of a jet. At $Re \geq 24$ investigated, shorter nozzles generally show weaker contraction, in line with the underdeveloped upstream velocity profile within the nozzle. Increasing the nozzle length allows the flow to develop closer to a Poiseuille flow, thereby increasing the axial nozzle exit momentum flux and resulting in a jet experiencing more contraction. At $Re = 400$, the largest Reynolds number investigated, the difference in final contraction ratio between the shortest and largest nozzle, far downstream of the nozzle outlet, reaches approximately 6%.

Finally, the jet expansion or contraction ratio χ was reconstructed via the integral momentum balance decomposition using numerical CFD data for the degree of flow development with respect to a fully developed flow, viscous stresses and pressure effects and capillary terms. The reconstruction shows good agreement with the jet ratios obtained directly from the numerical data. Furthermore, the numerical results show trends similar to those reported in the experimental work by Gavis and Modan [8], although quantitative differences remain, due to the overestimated effect of surface tension, resulting in less contraction in the high Reynolds number regime. Nevertheless, the qualitative agreement supports their hypothesis that an underdeveloped flow reduces the contraction of a laminar liquid jet.

Furthermore, the differences between numerical and experimental contraction ratios at higher Reynolds numbers were investigated by considering the influence of surface tension. A sensitivity analysis of the integral momentum balance reconstruction, assuming unchanged flow fields and interface geometry, demonstrated that the capillary contributions can have a larger influence on the predicted contraction than initially thought, both directly through the capillary term C_σ and indirectly through the capillary pressure inside $\bar{K}/Re$. Additional OpenFOAM simulations at increased Weber numbers have confirmed that decreasing the relative importance of surface tension results in a stronger contracting jet. It should be noted that the reduction observed in these additional simulations was smaller than predicted by the integral momentum balance reconstruction, since the downstream distance at which the final jet contraction ratio was measured was fixed, where the jets might not have reached their constant radius yet. Still, these results support the hypothesis that the relatively strong capillary effects in the original simulations contribute significantly to an overestimated jet contraction ratio at higher Reynolds numbers.

Overall, the results indicate that the effect of the nozzle length on the expansion and contraction behaviour is closely related to the hydrodynamic development length required for the flow to reach the fully developed Poiseuille state. An approximately fully developed profile at the nozzle exit shows that the jet behaviour is largely independent of the nozzle length. An underdeveloped flow results in weaker contraction when ejected from a short nozzle at a high Reynolds number; at low Reynolds numbers, within the range of nozzle lengths investigated, the expansion and contraction behaviour is mainly a consequence of the exit-induced viscous perturbations.

9. Recommendations for future work

For future research, it is recommended to extend the Reynolds number range even further, to beyond $Re = 400$ and into the limits of laminar pipe flow, up to $Re \approx 2000$. The reconstructions, experimental results and numerical results show that the final contraction ratio χ increases for undeveloped flow, as the Reynolds number is increased. Therefore, additional simulations at higher Reynolds numbers should include sufficiently long nozzles to obtain a fully developed velocity profile at the nozzle exit. This would allow for clearer distinction between the influence of hydrodynamic flow development and viscous outflow effects on the dimensionless viscous term in the integral momentum balance, $\tilde{K}/Re$. Furthermore, investigating fully developed jets at higher Reynolds numbers would allow for a more detailed investigation of the approach towards the theoretical contraction limit of $\frac{1}{2}\sqrt{3}$, derived by Harmon [12]. The numerical results for $L/R = 21.4$ show that the contraction ratio approached this limit, before increasing again as the nozzle flow becomes undeveloped at higher Reynolds numbers. Consequently, investigation of this limit requires sufficiently long nozzles and a sufficiently long computational domain, as the jet requires a greater distance to reach its final constant radius.

Moreover, for the lowest Reynolds numbers investigated in this work, the required hydrodynamic development length is very low, less than the shortest nozzle investigated ($L = 1.94R$). Consequently, the flow reaches its fully developed velocity profile before exiting the nozzle. However, for even shorter nozzles, outlet effects might have an effect on the inlet conditions, such as when $L = 0.5D$, or equivalently, $L = 1R$. The numerical results have shown that exit perturbations occur approximately $1R$ upstream of the nozzle exit. For nozzles with a length less than this, these exit perturbations might have an effect throughout the entire length of the nozzle and the inlet velocity might not be determined only by the hydrodynamic flow development, but also by the viscous perturbations as a consequence of the outflow conditions. As a result, the assumption of a uniform inflow velocity might become invalid. Further numerical research should therefore consider shorter nozzles, while extending the numerical domain far enough upstream for the interaction between inlet and outlet regions to be resolved. This would allow a quantification of the influence of upstream boundary conditions on the nozzle exit velocity profile to be investigated. Furthermore, it would provide more insight into validity of the decomposition of hydrodynamic flow development and exit-induced perturbations, as considered in the integral momentum balance decomposition, when inlet and outlet flows interact.

References

[1] C. Barus. “Isothermals, isopiestics and isometrics relative to viscosity”. In: *American Journal of Science* s3-45.266 (Feb. 1893), pp. 87–96. ISSN: 0002-9599. DOI: 10.2475/ajs.s3-45.266.87.

[2] J. U. Brackbill, D. B. Kothe, and C. Zemach. “A continuum method for modeling surface tension”. In: *Journal of Computational Physics* 100.2 (1992), pp. 335–354.

[3] W.-P. Breugem and Y. E. Kamis. “Newtonian die-swell phenomenon revisited: Theory and simulations”. In: *Physical Review Fluids* 11.5 (May 2026). ISSN: 2469-990X. DOI: 10.1103/l1b2-blw2.

[4] E. R. A. Coyajee. “A front-Capturing method for the numerical simulation of dispersed two-phase flow”. Dissertation (TU Delft). Delft University of Technology, 2007. ISBN: 978-90-9022160-1.

[5] S. S. Deshpande, L. Anumolu, and M. F. Trujillo. “Evaluating the performance of the two-phase flow solver interFoam”. In: *Computational Science Discovery* 5.1 (Nov. 2012), p. 014016. ISSN: 1749-4699. DOI: 10.1088/1749-4699/5/1/014016.

[6] F. Durst, S. Ray, B. Ünsal, and O. A. Bayoumi. “The development lengths of laminar pipe and channel flows”. In: *Journal of Fluids Engineering* 127.6 (June 2005), pp. 1154–1160. ISSN: 1528-901X. DOI: 10.1115/1.2063088.

[7] S. H. Garrioch and B. R. Baliga. “A PLIC volume tracking method for the simulation of two-fluid flows”. In: *International Journal for Numerical Methods in Fluids* 52.10 (2006), pp. 1093–1134. ISSN: 1097-0363. DOI: 10.1002/fld.1217.

[8] J. Gavis and M. Modan. “Expansion and contraction of jets of Newtonian liquids in air: Effect of tube length”. In: *The Physics of Fluids* 10.3 (Mar. 1967), pp. 487–497. ISSN: 0031-9171. DOI: 10.1063/1.1762142.

[9] S. L. Goren. “Development of the boundary layer at a free surface from a uniform shear flow”. In: *Journal of Fluid Mechanics* 25.1 (May 1966), pp. 87–95. ISSN: 1469-7645. DOI: 10.1017/s0022112066000065.

[10] S. L. Goren and S. Wronski. “The shape of low-speed capillary jets of Newtonian liquids”. In: *Journal of Fluid Mechanics* 25.1 (May 1966), pp. 185–198. ISSN: 1469-7645. DOI: 10.1017/s0022112066000120.

[11] C. Greenshields. *OpenFOAM 8 released: OpenFOAM Foundation*. July 2020. URL: https://openfoam.org/release/8/.

[12] D. B. Harmon. “Drop sizes from low speed jets”. In: *Journal of the Franklin Institute* 259.6 (June 1955), pp. 519–522. ISSN: 0016-0032. DOI: 10.1016/0016-0032(55)90098-3.

[13] H. D. Haustein, R.S. Harnik, and W. Rohlfs. “A simple hydrodynamic model of a laminar free-surface jet in horizontal or vertical flight”. In: *Physics of Fluids* 29.8 (Aug. 2017). ISSN: 1089-7666. DOI: 10.1063/1.4996771.

[14] C. W. Hirt and B. D. Nichols. “Volume of fluid (VOF) method for the dynamics of free boundaries”. In: *Journal of Computational Physics* 39.1 (Jan. 1981), pp. 201–225. ISSN: 0021-9991. DOI: 10.1016/0021-9991(81)90145-5.

[15] D. D. Joseph. “Slow motion and viscometric motion; stability and bifurcation of the rest state of a simple fluid”. In: *Archive for Rational Mechanics and Analysis* 56.2 (1974), pp. 99–157. ISSN: 1432-0673. DOI: 10.1007/bf00248137.

[16] Y. E. Kamis, S. Prakash, W. -P. Breugem, and H. B. Eral. “Controlling the breakup of spiralling jets: results from experiments, nonlinear simulations and linear stability analysis”. In: *Journal of Fluid Mechanics* 956 (Feb. 2023). ISSN: 1469-7645. DOI: 10.1017/jfm.2023.31.

[17] J. Knir. *PLIC,MPLIC: New piecewise-linear interface compression schemes*. July 2020. URL: https://github.com/OpenFOAM/OpenFOAM-dev/commit/1611e0dbfbf9a9d5ee65fde97ec38e93a781d4d6.

[18] P. K. Kundu, I. M. Cohen, and D. R. Dowling. “Chapter 9: Laminar Flow”. In: *Fluid Mechanics*. Elsevier, 2016, pp. 1–48.

[19] H. S. Lew. “The use of entry flow equations in studying the uniform entry flow”. In: *Journal of Biomechanics* 6.2 (Mar. 1973), pp. 205–214. ISSN: 0021-9290. DOI: 10.1016/0021-9290(73)90089-4.

[20] S. Middleman and J. Gavis. “Expansion and contraction of capillary jets of Newtonian liquids”. In: *The Physics of Fluids* 4.3 (Mar. 1961), pp. 355–359. ISSN: 0031-9171. DOI: 10.1063/1.1706332.

[21] S. Middleman and J. Gavis. “Expansion and contraction of capillary jets of viscoelastic liquids”. In: *The Physics of Fluids* 4.8 (Aug. 1961), pp. 963–969. ISSN: 0031-9171. DOI: 10.1063/1.1706446.

[22] B. D. Nichols and C. W. Hirt. “Methods for calculating multi-dimensional, transient free surface flows past bodies”. In: Los Alamos Scientific Lab., N.Mex. (USA). Jan. 1975. URL: https://www.osti.gov/biblio/5044626.

[23] R. E. Nickell, R. I. Tanner, and B. Caswell. “The solution of viscous incompressible jet and free-surface flows using finite-element methods”. In: *Journal of Fluid Mechanics* 65.1 (Aug. 1974), pp. 189–206. ISSN: 1469-7645. DOI: 10.1017/s0022112074001339.

[24] B.J. Omodei. “On the die-swell of an axisymmetric Newtonian jet”. In: *Computers & Fluids* 8.3 (Sept. 1980), pp. 275–289. ISSN: 0045-7930. DOI: 10.1016/0045-7930(80)90018-3.

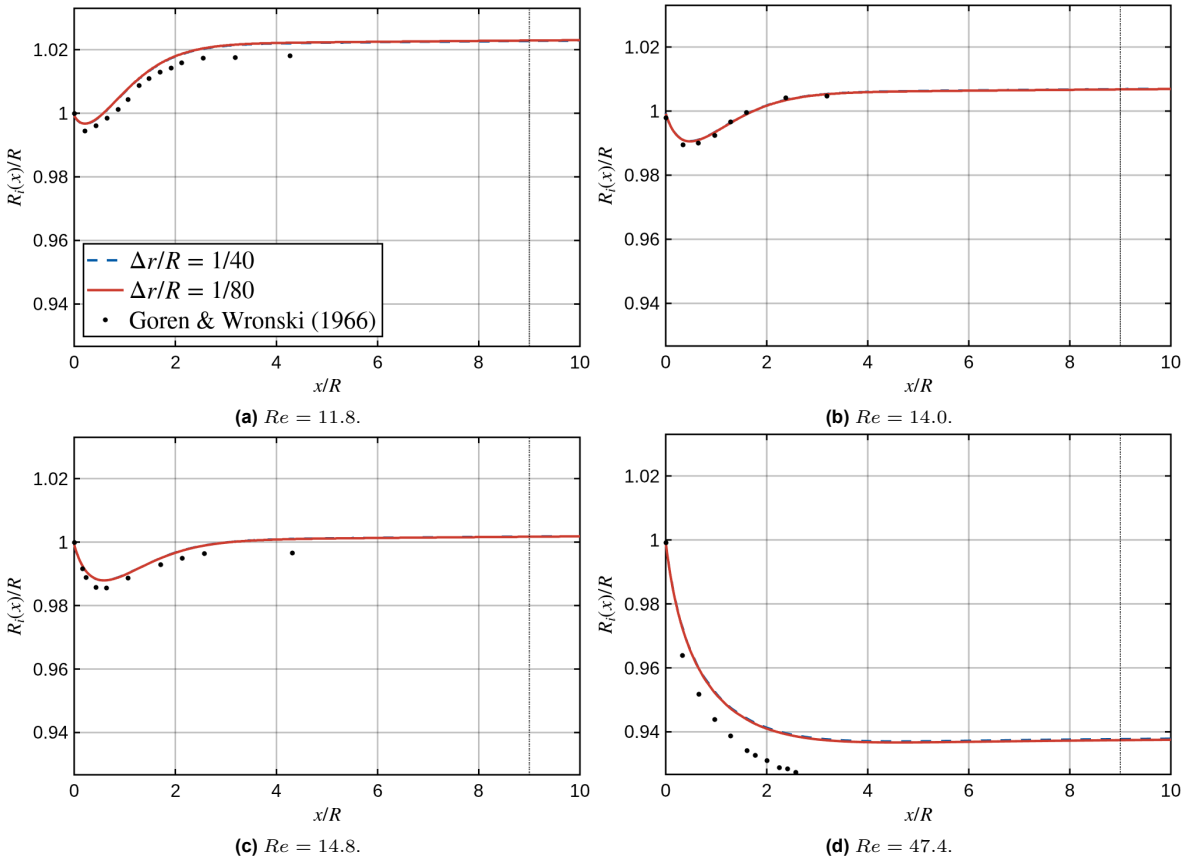
[25] G. Ooms, M. Pourquie, and W.-P. Breugem. “On the hydrodynamic stability of a viscous liquid jet enclosed in a narrow tube”. In: *International Journal of Multiphase Flow* 200 (2026), p. 105712. ISSN: 0301-9322. DOI: 10.1016/j.ijmultiphaseflow.2026.105712.

[26] K. R. Reddy and R. I. Tanner. “Finite element solution of viscous jet flows with surface tension”. In: *Computers & Fluids* 6.2 (June 1978), pp. 83–91. ISSN: 0045-7930. DOI: 10.1016/0045-7930(78)90009-9.

[27] S. Richardson. “A ‘stick-slip’ problem related to the motion of a free jet at low Reynolds numbers”. In: *Mathematical Proceedings of the Cambridge Philosophical Society* 67.2 (Mar. 1970), pp. 477–489. ISSN: 1469-8064. DOI: 10.1017/s0305004100045758.

[28] F. M. White. *Fluid mechanics*. 8th edition in SI Units. McGraw-Hill Ed. New York, NY: McGraw-Hill Education, 2016. ISBN: 978-9-814-72017-5.

A. Mesh sensitivity study



(a) $Re = 11.8$.

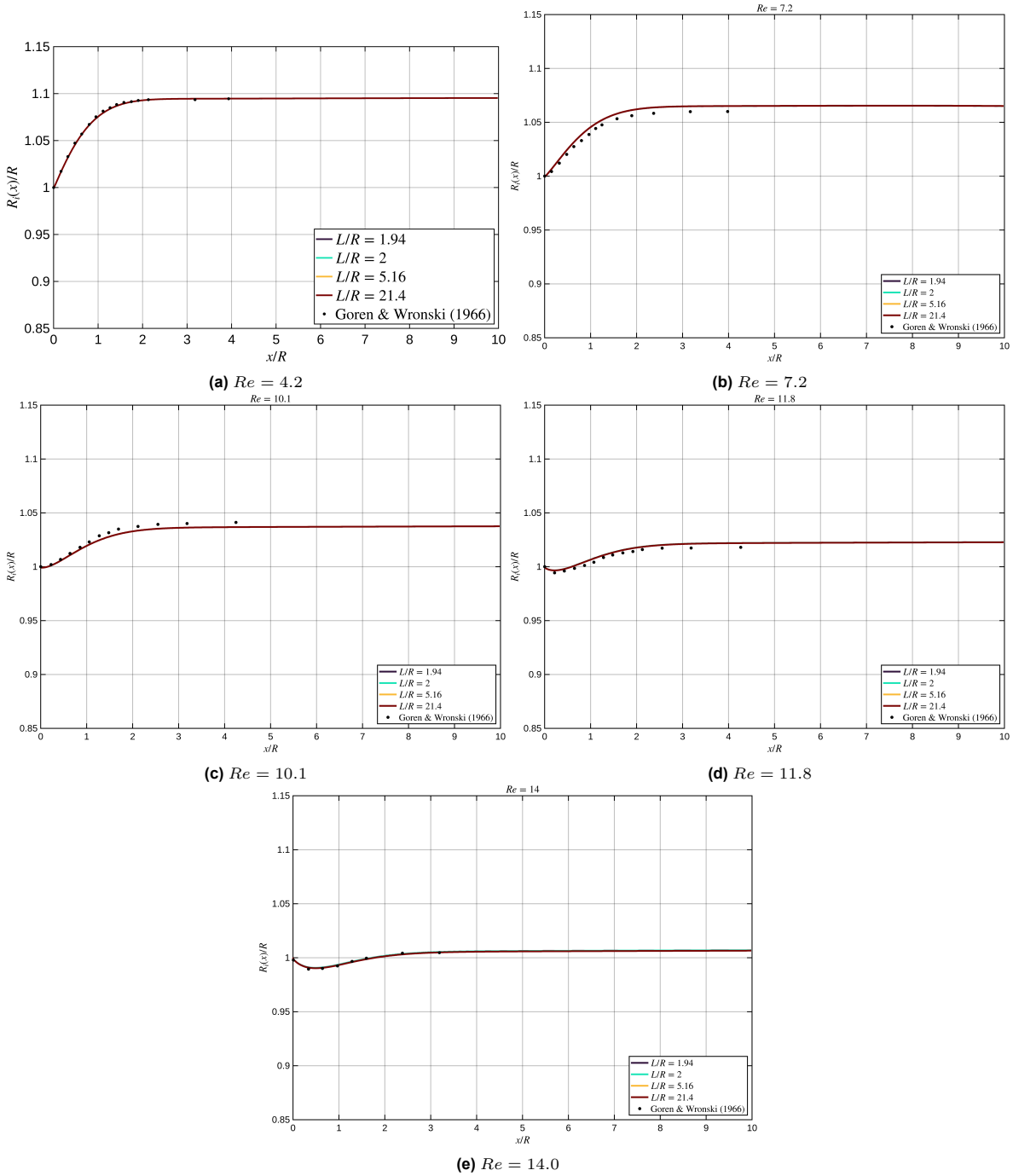
(b) $Re = 14.0$.

(c) $Re = 14.8$.

(d) $Re = 47.4$.

Figure A.1: Comparison between two grid resolutions $\Delta r/R = 1/40$ and $\Delta r/R = 1/80$ for three expanding-contracting jets and one contracting jet, ejected from the shortest nozzle of $L = 1.94R$. The results for $\Delta r/R = 1/40$ and $\Delta r/R = 1/80$ show identical interface profiles and similar deviation from the results for a fully developed flow by Goren and Wronski [10], verifying $\Delta r/R = 1/40$ was fine enough. The flow for $Re = 47.4$ is undeveloped within this nozzle, hence the noticeable deviation from the experimental results.

B. Additional numerical surface results



(a) $Re = 4.2$

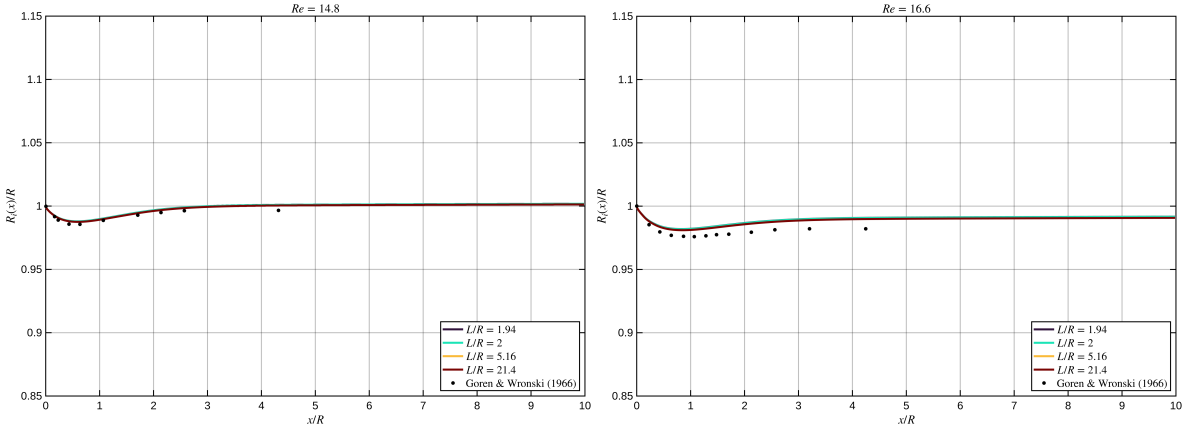
(b) $Re = 7.2$

(c) $Re = 10.1$

(d) $Re = 11.8$

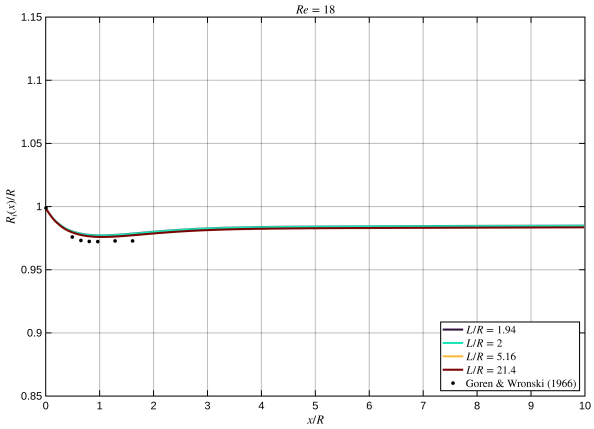
(e) $Re = 14.0$

Figure B.1: Jet surface profiles as a function of x/R downstream of the nozzle outlet and nozzle length L/R, for Reynolds numbers $4.2 \leq Re \leq 400$. The black dots represent experimental data by Goren and Wronski [10], where available.

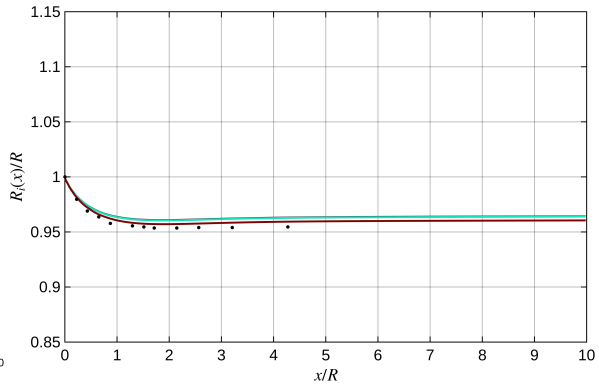


(f) $Re = 14.8$

(g) $Re = 16.6$

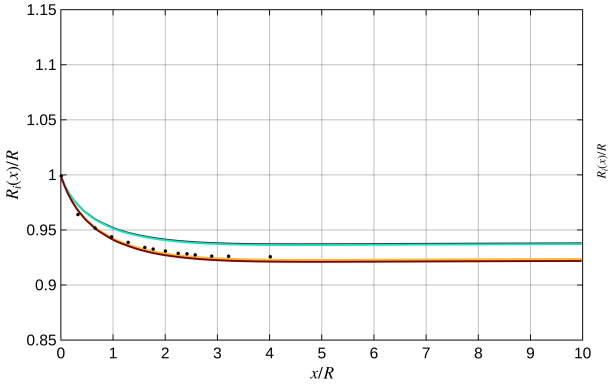


(h) $Re = 18.0$

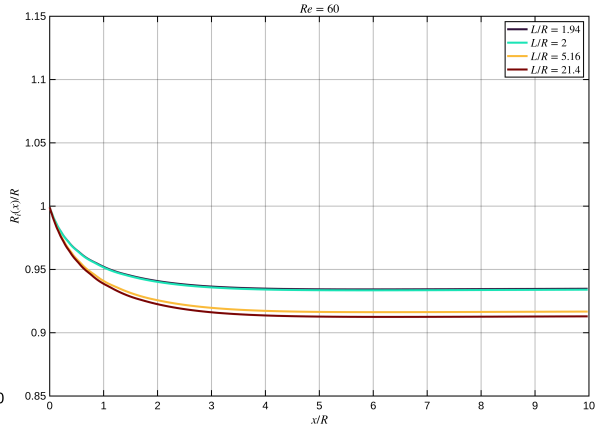


(i) $Re = 24.0$

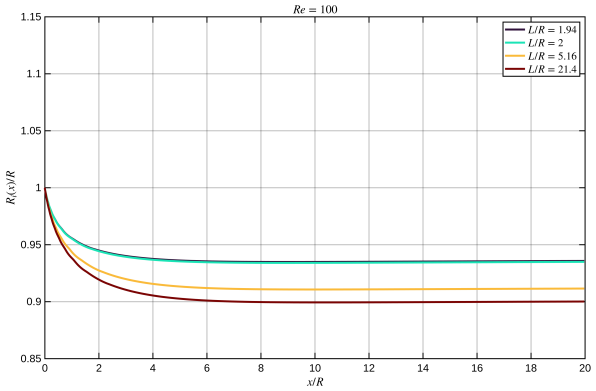
Figure B.1: Jet surface profiles as a function of x/R downstream of the nozzle outlet and nozzle length L/R (continued).



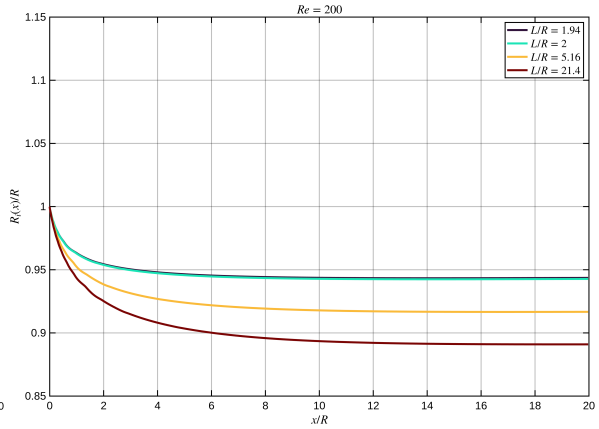
(j) $Re = 47.4$



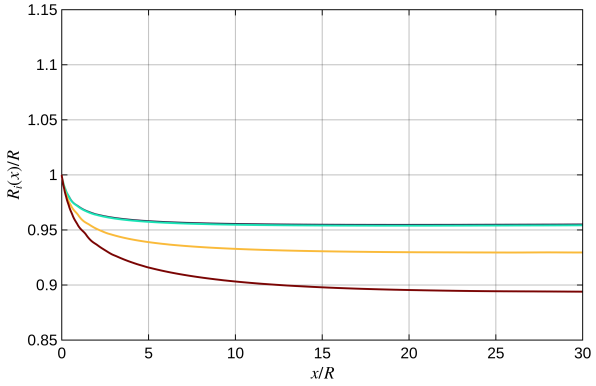
(k) $Re = 60.0$



(l) $Re = 100.0$



(m) $Re = 200.0$



(n) $Re = 400.0$

Figure B.1: Jet surface profiles as a function of x/R downstream of the nozzle outlet and nozzle length L/R (continued).

C. Numerical solver settings

All jet cases were run with a maximum permitted Courant number of $Co = 0.02$ and an interface Courant number of $\alpha Co = 0.1$, whereas the pipe cases were run with $Co = 0.2$.

The OpenFOAM solver controls, discretisation schemes, and run-time settings are given in the following configuration files. Apart from the use of *div(phi,alpha) Gauss PLIC interfaceCompression vanLeer 1* as the divergence discretisation scheme, the settings are identical to the *damBreakLaminar* VOF tutorial shipped with the software package.

C.1. `controlDict`

```
/*--------------------------------*- C++ -*----------------------------------*\
  =========                 |
  \\      /  F ield         | OpenFOAM: The Open Source CFD Toolbox
   \\    /   O peration     | Website:  https://openfoam.org
    \\  /    A nd           | Version:  13
     \\/     M anipulation  |
\*---------------------------------------------------------------------------*/
FoamFile
{
    format      ascii;
    class       dictionary;
    location    "system";
    object      controlDict;
}
// * * * * * * * * * * * * * * * * * * * * * * * * * * * * * * * * * * * * //

#include "$FOAM_CASE/parameters"

solver          incompressibleVoF;

startFrom       startTime;

startTime       0;

stopAt          $endTime;

endTime         25;

deltaT          1e-5;

writeControl    adjustableRunTime;

writeInterval   0.5;

purgeWrite      0;

writeFormat     binary;

writePrecision  6;

writeCompression off;

timeFormat      general;

timePrecision   6;

runTimeModifiable true;

adjustTimeStep  true;

maxCo           $maxCo;
maxAlphaCo      $maxAlphaCo;
```

```
53
54  maxDeltaT       $maxDeltaT;
55
56  DebugSwitches
57  {
58      MULES           1;
59  }
60
61
62  // ************************************************************************* //
```

Listing C.1: OpenFOAM `controlDict` configuration

C.2. fvSolution

```
1   /*--------------------------------*- C++ -*----------------------------------*\
2     =========                 |
3     \\      /  F ield         | OpenFOAM: The Open Source CFD Toolbox
4      \\    /   O peration     | Website:  https://openfoam.org
5       \\  /    A nd           | Version:  13
6        \\/     M anipulation  |
7   \*---------------------------------------------------------------------------*/
8   FoamFile
9   {
10      format      ascii;
11      class       dictionary;
12      location    "system";
13      object      fvSolution;
14  }
15  // * * * * * * * * * * * * * * * * * * * * * * * * * * * * * * * * * * * * * //
16  solvers
17  {
18      "alpha.water.*"
19      {
20          nCorrectors     2;
21          nSubCycles      2;
22
23          MULESCorr       no;
24
25          MULES
26          {
27              nIter           10;
28              tolerance       1e-2;
29          }
30
31          solver          smoothSolver;
32          smoother        symGaussSeidel;
33          tolerance       1e-8;
34          relTol          0;
35      }
36
37      "pcorr.*"
38      {
39          solver          PCG;
40          preconditioner  DIC;
41          tolerance       1e-5;
42          relTol          0;
43      }
44
45      p_rgh
46      {
47          solver          PCG;
48          preconditioner  DIC;
49          tolerance       1e-7;
50          relTol          0.05;
51      }
52
53      p_rghFinal
54      {
55          $p_rgh          ;
```

```
        relTol          0;
    }

    "(U|k|epsilon|omega).*"
    {
        solver          smoothSolver;
        smoother        symGaussSeidel;
        tolerance       1e-10;
        relTol          0;
        minIter         1;
    }
}

PIMPLE
{
    momentumPredictor no;
    nOuterCorrectors 1;
    nCorrectors     3;
    nNonOrthogonalCorrectors 0;
}

relaxationFactors
{
    equations
    {
        ".*"            1;
    }
}


// ************************************************************************* //
```

Listing C.2: OpenFOAM `fvSolution` configuration

C.3. fvSchemes

```
/*--------------------------------*- C++ -*----------------------------------*\
  =========                 |
  \\      /  F ield         | OpenFOAM: The Open Source CFD Toolbox
   \\    /   O peration     | Website:  https://openfoam.org
    \\  /    A nd           | Version:  13
     \\/     M anipulation  |
\*---------------------------------------------------------------------------*/
FoamFile
{
    format      ascii;
    class       dictionary;
    location    "system";
    object      fvSchemes;
}
// * * * * * * * * * * * * * * * * * * * * * * * * * * * * * * * * * * * * * //

ddtSchemes
{
    default         Euler;
}

gradSchemes
{
    default         Gauss linear;
}

divSchemes
{
    div(phi,alpha)  Gauss PLIC interfaceCompression vanLeer 1;

    div(rhoPhi,U)   Gauss linearUpwind grad(U);

    div(((rho*nuEff)*dev2(T(grad(U))))) Gauss linear;
}
```

```
35
36  laplacianSchemes
37  {
38      default         Gauss linear uncorrected;
39  }
40
41  interpolationSchemes
42  {
43      default         linear;
44  }
45
46  snGradSchemes
47  {
48      default         uncorrected;
49  }
50
51
52  // ************************************************************************* //
```

Listing C.3: OpenFOAM `fvSchemes` configuration

C.4. blockMeshDict

```
1  /*--------------------------------*- C++ -*----------------------------------*
2  | =========                 |
3  | \      /  F ield         | OpenFOAM: The Open Source CFD Toolbox
4  |  \    /   O peration     |
5  |   \  /    A nd           |
6  |    \/     M anipulation  |
7  *---------------------------------------------------------------------------*/
8
9  FoamFile
10 {
11 format      ascii;
12 class       dictionary;
13 object      blockMeshDict;
14 }
15
16 #include "$FOAM_CASE/parameters"
17
18 convertToMeters 1;
19
20 // VERTICES
21
22 vertices
23 (
24 // x = 0 / INLET PLANE
25 (0      0   0)              // 0
26 (0      $yR  $minusZR)      // 1
27 (0      $yR  $zR)           // 2
28
29 // xptR = Lactual/R - R/R = LR - 1
30 ($XptR  0    0)             // 3
31 ($XptR  $yR  $minusZR)      // 4
32 ($XptR  $yR  $zR)           // 5
33
34 // x = Lactual/R = LR
35 ($LR   0     0)             // 6
36 ($LR   $yR   $minusZR)      // 7
37 ($LR   $yR   $zR)           // 8
38
39 // x = Ldomain/R = Lactual + 15R
40 ($XdomainR     0     0)     // 9
41 ($XdomainR     $yR   $minusZR) // 10
42 ($XdomainR     $yR   $zR)      // 11
43
44 // Domain 'above' nozzle exit
45 ($XptR      $yRT   $zRT)        // 12
46 ($XptR      $yRT   $minusZRT)   // 13
47
48 ($LR        $yRT   $zRT)        // 14
49 ($LR        $yRT   $minusZRT)   // 15
50
51 ($XdomainR  $yRT   $zRT)        // 16
52 ($XdomainR  $yRT   $minusZRT)   // 17
53
54 ($XptR  $yR  $minusZR)          // 18
55 ($XptR  $yR  $zR)              // 19
56
```

```
// Fake 'hump' region
($hump      0     0)            // 20
($hump      $yR   $minusZR)     // 21
($hump      $yR   $zR)          // 22

);

// BLOCKS

blocks
(
    // NOZZLE

    // Block 0: Hump zone

    hex (20 21 22 20 0 1 2 0)
    ($nCellRadial $nCellAz $nCellAxialZero)

    simpleGrading ($zeroRadial 1 $zeroAxial)

    // Block 1: Inlet/bulk Zone
    hex (0 1 2 0 3 4 5 3)
    ($nCellRadial $nCellAz $nCellAxialOne)

    simpleGrading ($oneRadial 1 $oneAxial)

    // Block 2: Exit Zone
    hex (3 4 5 3 6 7 8 6)
    ($nCellRadial $nCellAz $nCellAxialTwo)

    simpleGrading ($twoRadial 1 $twoAxial)

    // Block 3: Jet Zone
    hex (6 7 8 6 9 10 11 9)
    ($nCellRadial $nCellAz $nCellAxialThree)

    simpleGrading ($threeRadial 1 $threeAxial)

    // OUTER DOMAIN (atmosphere - environment)

    // Block 4: Environment above Exit Zone
    hex (18 13 12 19 7 15 14 8)
    ($nCellRadialEnv $nCellAz $nCellAxialFour)

    simpleGrading ($fourRadial 1 $fourAxial)

    // Block 5: Environment above J Zone
    hex (7 15 14 8 10 17 16 11)
    ($nCellRadialEnv $nCellAz $nCellAxialFive)

    simpleGrading ($fiveRadial 1 $fiveAxial)
);

// BOUNDARIES

boundary
(
humpWall
{
    type wall;

    faces
    (
        (21 22 1 2)
    );
}
inlet
{
    type patch;

    faces
    (
        (20 21 22 20) // NB numerical inlet is before the hump region, first 0.xx m is slip BC for U
    );
}

outlet
{
    type patch;

    faces
    (
        (9 10 11 9)
        (10 17 16 11)
```

```
    );
}

pipeWall
{
    type wall;

    faces
    (
        (1 2 5 4)
    );
}

exitRegionWall
{
    type wall;

    faces
    (
        (4 5 8 7)
    );
}

virtualExitRegionWall
{
    type wall;

    faces
    (
        (18 19 8 7)
    );
}

sideBoundary
{
    type patch;

    faces
    (
        (18 19 13 12)
    );
}

topBoundary
{
    type patch;

    faces
    (
        (13 12 14 15)
        (15 14 16 17)
    );
}

axis
{
    type empty;

    faces
    (
        (0 3 3 0)
        (3 6 6 3)
        (6 9 9 6)
    );
}

frontWedge
{
    type wedge;

    faces
    (
        (20 0 2 22)
        (0 3 5 2)
        (3 6 8 5)
        (6 9 11 8)

        (19 12 14 8)
        (8 14 16 11)
    );
}

backWedge
{
```

```
225     type wedge;
226
227     faces
228     (
229         (20 21 1 0)
230         (0 1 4 3)
231         (3 4 7 6)
232         (6 7 10 9)
233
234         (18 7 15 13)
235         (7 15 17 10)
236     );
237 }
238
239 );
```

Listing C.4: OpenFOAM `blockMeshDict` configuration

D. Numerical mesh settings

L/R	$N_{x,\mathrm{pipe}}$	$N_{x,\mathrm{jet}}$ $(Re < 400)$	$N_{x,\mathrm{jet}}$ $(Re = 400)$
1.94	198	678	1078
2.00	200	680	1080
5.16	328	808	1208
21.40	976	1456	1856

Table D.1: Mesh dimensions for the four nozzle geometries. The number of radial cells $N_r = 40$ is identical for all cases. The jet simulations at $Re = 400$ use an extended downstream domain, resulting in a larger number of axial cells N_x. The nominal cell size is $\Delta x_i/R = 1/40$.

Re	T_{final} $(L/R = 1.94,\ 2.00,\ 5.16)$	T_{final} $(L/R = 21.4)$
4.2	50	50
7.2–60	25	50
100–200	60	60
400	75	75

Table D.2: Final simulation times T_{final} for the different Reynolds numbers and nozzle geometries. All undisturbed pipe-flow simulations were run until $T_{\mathrm{final}} = 25$.

E. AI Statements

Prompts used for the cover image:

'Generate a visualization for a cover page of my Master thesis, visualizing the concept of the laminar liquid jet. Emphasize on different nozzle lengths and how they influence the jet expansion or contraction. The jet radius at the nozzle exit should be the same as the nozzle radius. Generate three jets from top to bottom: an expanding jet, expansion should start right at the nozzle exit, an contracting then expanding jet, the contraction should start right at the nozzle exit, and a purely contracting jet, the contraction should start right at the nozzle exit. The background must be white.'

Prompts used for the VOF / PLIC visualisations (Figs. 3.2 and 3.1), after sketching the VOF methodology myself:

'Visualize VOF, use the following caption as a start: 'Sketch of the average analytical volume fractions for a curved interface on a fixed grid.' Make the interface more curved.'

Other AI usage include the generation of MATLAB, Python, C scripts during the pre- and post-processing stage and troubleshooting while running OpenFOAM.